Summer 8-16-2019

Design, Construction and Application of a Home-Built, Two-Photon Microscope

William P. Breeding
University of Maine, william.breeding@maine.edu

DESIGN, CONSTRUCTION AND APPLICATION OF A HOME-BUILT, TWO-PHOTON MICROSCOPE

By

William Patrick Breeding

B.S. Biomedical Engineering, 2017

A THESIS

Submitted in Partial Fulfillment of the

Requirements for the Degree of

Master of Science

(in Biomedical Engineering)

The Graduate School

The University of Maine

August 2019

Advisory Committee:

Karissa Tilbury, Assistant Professor of Biomedical Engineering, Advisor

Michael Mason, Professor of Biomedical Engineering

Paul Millard, Associate Professor of Biomedical Engineering

Robert Bayer, Professor Emeritus of Animal and Veterinary Science

DESIGN, CONSTRUCTION AND APPLICATION OF A HOME-BUILT, TWO-PHOTON MICROSCOPE

By William Patrick Breeding

Thesis Advisor: Dr. Karissa Tilbury

An Abstract of the Thesis Presented
in Partial Fulfillment of the Requirements for the
Master of Science
(in Biomedical Engineering)
August 2019

Two-photon microscopy (TPM) is a powerful, versatile imaging modality for the study of biological systems. This thesis overviews the relevant physics involved in TPM, design considerations and process of constructing a home-built, two-photon microscope, and provides a set of procedures to operate the system. Furthermore, this work explores several applications of TPM through the study of single-cell metabolism and imaging the cellular-material interface. Explored in particular depth was the imaging of cellulose nanofiber (CNF) materials, with the goal of understanding the three-dimensional nature of fibroblast cell growth when embedded within the materials. This work uncovered several optical properties of CNF, and resulted in the creation of a novel method for imaging three-dimensional cellular growth into CNF materials; resolving fine material and biological structures without perturbing the native environment.

DEDICATION

To my Dad. Thank you for giving me every opportunity to explore curiosity, adventure, mess up, learn and grow. This is but a small step in becoming the man you would be proud of.

ACKNOWLEDGEMENTS

Thank you to my family for all your grace and support. To my loving partner Amber for giving me strength, being my best friend and rock. To my incredible friends for supporting me and keeping me grounded. To my lab mates, especially Mitchell Harling, Aimee and Aileen Co, and Jeremy Grant, for your patience and friendship. Thank you to David Holomakoff for your strength, energy and being my perpetual partner-in-crime. Thank you to Bob Bayer, Renee Kelly, Richard 'Rich' Corey, Caitlin Howell, and members of my tribe that have offered me mentorship, support, or just took the time to listen. Most of all, thank you to my advisor, Karissa Tilbury, for exposing and subjecting me to so many interesting, unique experiences and situations, which evoked incredible personal and professional growth.

TABLE OF CONTENTS

LIST OF TABLES

LIST OF FIGURES

LIST OF EQUATIONS

INTRODUCTION

Optics are the truly the predominant means by which we observe, interpret and understand the way the world works from a macro to microscopic level. The field of optics has progressed significantly and iteratively, in one perspective, through phases of addressing increasingly more complex challenges, overcoming these challenges and opening doors to new frontiers. For example, downfalls of human's innate optical system, the unaided physical eye, were addressed with the invention of the eyeglass. Once the door was opened, a new set of optical tools were invented and a frontier in our ability to visualize the world was explored. This platform of tools could only take us so far, so more complex means to visualize visibly 'small structures', such as stars, were investigated; leading to the development of the microscope. Again, this opened a breadth of doors leading to and still resulting in centuries of invention and exploration, but following the cyclical trend, traditional light microscopes could only take us so far.

In the past century, the field of optics has become truly illuminated with inventors and innovators who more intimately understand physics and physical systems, comprehend the challenges of using current means to probe systems, and harness previously unexplored optics and optical processes to better visualize these such systems. The information about things, systems, and the world is already available; we simply need to wield the right tools to uncover the desired information. Doing so requires innovators to try new approaches to gain new insights, and a well-justified demonstration of the validity of the information collected using new tools. New information can create value, understanding and meaning in all aspects of our life; from the materials we use, the food we eat and the very function of living organisms.

This is why exploration in the field of optics is so important, where the needle is moved with a thorough understanding of optical processes, understanding the versatility of our current tools, and how to combine, improve or create entirely new ones. This thesis adds to the wealth of exciting work utilizing

one of these versatile tools, a two-photon microscope, employing several optical processes to uncover new information about complex biological and material systems. Ultimately, this work provides the outline of a process to build one of these tools, how to wield it, and use it to better visualize and understand aspects how the world around us works.

CHAPTER 1

BACKGROUND

1.1. Introduction to Fluorescence Microscopy

The development of fluorescence microscopy to observe, study and understand specimens revolutionized many fields of science; arguably one of the greatest booms to accelerate field of scientific research. Fluorescence microscopy employs fluorophores, whether endogenous or exogenous, to probe samples of interests under a microscope by illuminating with a particular wavelength of light, and collecting the subsequent fluorescent emission generated from an absorption event of the incident photons.

Initially, the general fluorescence microscope system employed a lamp or laser source, system of optics to direct the beam through an objective to illuminate a sample, fluorescence emission directed back through the objective, and reflected off a dichromatic mirror towards a camera. While applicable to many imaging situations, this setup, called widefield fluorescence microscopy, suffered greatly from poor imaging depth and unwanted out-of-focus signal [1].

To enhance the potential for imaging to greater depths and eliminate out of focal plane signal, Marvin Minsky invented the confocal microscope in 1955, which involved placing a pinhole just before emission detector to spatially filter out-of-focus light from outside the microscope's focal volume [2,3]. To construct a confocal image, it is necessary to scan across the sample, whether it be transforming the beam into a scanning state or translating the sample across an illumination area – slowly building a pixel by pixel, or line by line image by sweeping across the sample. As moving the sample, especially with sensitive biological specimens, could be destructive to the native conformation of the sample, scanning the beam was the pragmatic choice, thus leading to the Laser Scanning Confocal Microscope (LCSM), which has been one of, if not the most, widely utilized fluorescence microscope setup employed in scientific research to

date. Images acquired on a confocal microscope, when compared to the same sample area imaged on a widefield microscope, produced significantly higher-resolution images that lacked the blurry and de-focused appearance of a widefield image, as images were constructed based on photons emitted more tightly localized to the focal plane based on specific placement of the pinhole before the detector [4,5].

Figure 1.1. Physical demonstration of a single-photon and two-photon focal point. Visible beam focusing by a 20x water objective in a fluorescein filled vial (**A**), Two-photon laser excitation focused through a 10x air objective at the identical fluorescein vial and fluorescence emission from the focal point (**B**).

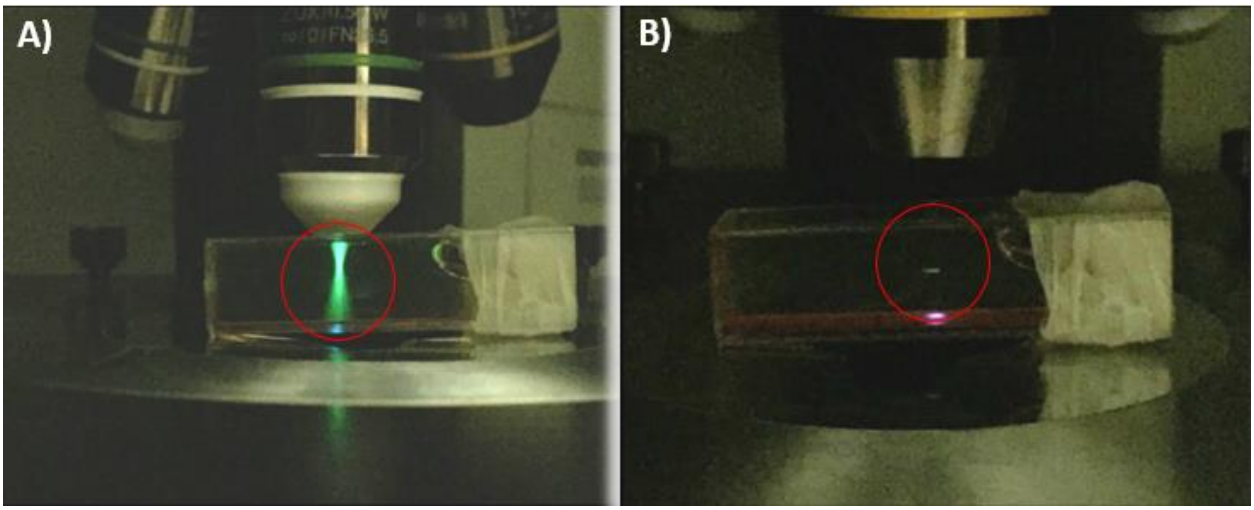

Although confocal is a highly utilized microscopy setup, far superior to the widefield fluorescence microscope, the setup still suffers from a range of problems. Some of these potential downfalls include: Sample photodamage due to continuous output laser, minimizing but not removing unwanted sample scattering, fixed excitation wavelength ranges (in many but not all cases), and sample imaging depth is still relatively superficial due to unwanted absorption or scattering events throughout the beam path. In many cases, these downfalls lead to an inadequate ability to extract the desired information about

complex systems, especially in biology, and it becomes necessary to deviate from traditional microscopy methods and employ more sophisticated physics and microscopy tools to ask 'deeper' questions.

1.2 History of Two-Photon Conceptualization

In 1931, Maria Göppert-Mayer published her doctoral thesis on the theoretical possibility of the simultaneous absorption of two photons by a single atom. In this work, she hypothesized the simultaneous absorption would amount to an energetic value comparable to that necessary to promote an electron to the excited state, which must lead to a subsequent emission event [6,7]. This was the basis for two-photon fluorescence [8].

The concept of two-photon fluorescence microscopy (TPM) presented itself to be a potentially viable alternative technique to account for the constraints experienced by confocal, as well as provide an array of additional benefits. However, it took 31 more years for this process to be experimentally demonstrated in the laboratory, first by Wolfgang Kaiser in 1961 when his group first observed two-photon events in a $CaF_2:Eu^{2+}$ crystal upon laser excitation [9]. Numerous studies followed these, leading to the development and patenting of the first two-photon microscope at Cornell in 1990 by James Strickler and Winfried Denk in Watt. W Webb's laboratory [10,11].

Following this groundbreaking work, studies involving two-photon microscopy (TPM) and adapting the technique to address a range of research questions increased in incidence following Moore's law. In this time period of rapid adoption of TPM, the breadth of applications were continuously realized and expanded upon, shown to pose as a viable technique to provide novel optical information, ultimately allowing researchers to ask and answer questions previously not thought to be possible [12]. In this thesis,

the applications of imaging single-cell metabolism and biological components within complex material scaffolds is of particular interest.

Figure 1.2. Trend of Publications Refencing Two-Photon Microscopy. Graph of studies using, referencing or reviewing two-photon microscopy and associated methods from 1965 - 2016, with a trend fitted to an exponential [13].

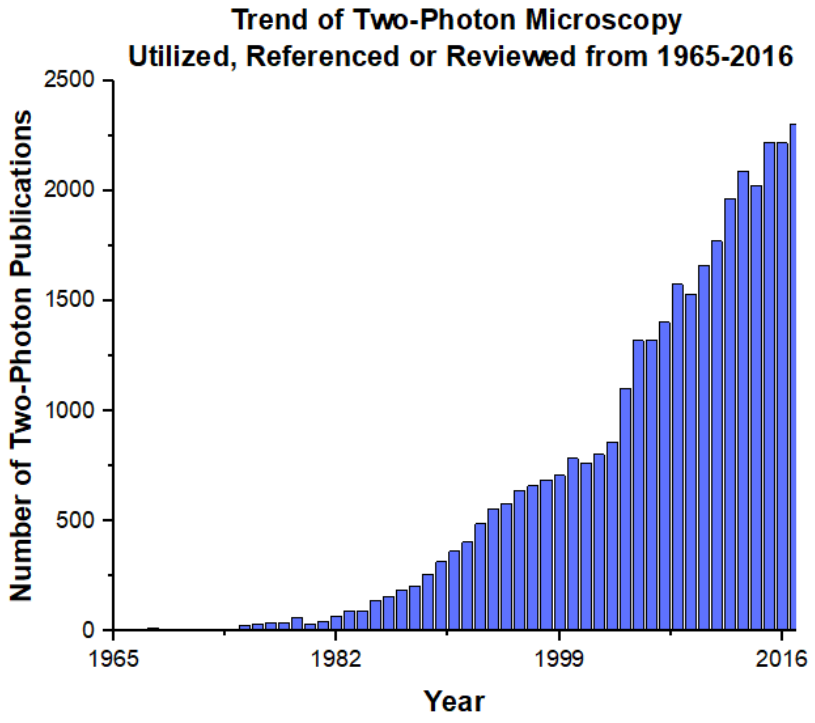

1.3 Two-Photon Physics

Two-photon absorption is an optical process in which a molecule near-simultaneously absorbs two incident photons, promoting a valence electron across the band gap to an excited state. This near-simultaneous absorption occurs where two photons, with wavelengths ranging from far red to near IR,

are absorbed by the same molecule within a femtosecond of each other. Electron promotion to the excited state occurs when the energetic combination of these two incident photons is at least slightly larger than the electron's band gap [14].

The excited state is an energetically volatile state, therefore non-favorable, and the electron is prone to releasing energy in any form possible to return to an available position in the ground state. To do so, in the excited state it possesses a high likeliness to move around vibrational/rotational states, losing small amounts of energy, until it reaches a point in which it must give off a significant amount of energy to jump back down across the band gap (Illustrated in **Figure 1.3A**). Just as energy was introduced into the system in the form of light (photons), the energy released is emitted in the form of an emitted photon. Due to energy loss within the excited state, the emission photon possesses slightly less energy than the energy required to promote it to the excited state, therefore, wavelength of the emission photon is slightly higher than the effective incident photon. When graphically representing the excitation and emission characteristics of a molecule, is it clear that the peak emission intensity is at a higher wavelength than the peak excitation wavelength. The distance between the excitation and emission peak is called the Stokes shift, displayed in **Figure 1.3B** [15], a concept first noted in the work of (and later named after) George G. Stokes in 1848 [16].

In the case of the near-simultaneous absorption of two photons, the emission photon is slightly higher than the value of half the wavelength of the incident photons – this overall process of near-simultaneous absorption and subsequent emission is two-photon fluorescence.

Figure 1.3. Jablonski diagram and graph depicting 1P/2P energy transfer and emission. **A**) Jablonski diagram depicting 1P and 2P energy transfer, **B**) Theoretical graph demonstrating a red-shifted stokes shift upon excitation (**B**).

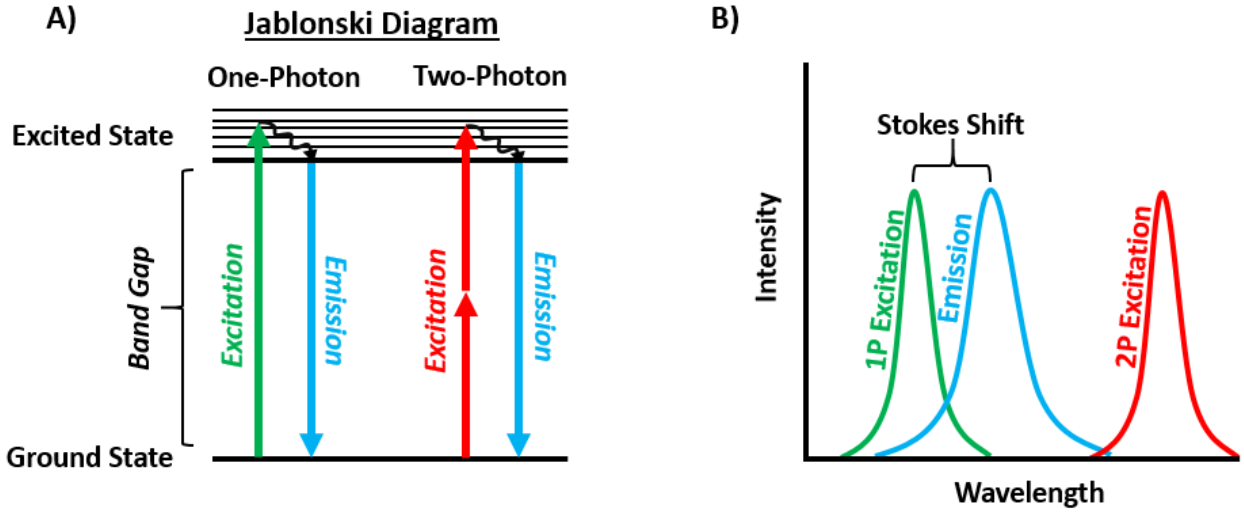

1.4 Advantages of Two-Photon Fluorescence Microscopy

The probability of a spontaneous two-photon absorption event in nature is extremely low, however, the combination of multiple system parameters, including laser wavelength, pulse repetition rate, power and the complimentary microscopy system, allow two-photon fluorescence to occur at a higher rate of incidence, in which it can be quantitatively predictable to happen in a controlled environment [17].

As the prerequisite for two-photon fluorescence is the near simultaneous absorption of two far red or infrared photons, the first requirement is a laser source capable of emitting such wavelengths. In two-photon systems, a laser emitting a beam consisting of photons between the wavelengths of 680- 1200nm is typically used. In addition, a microscopy setup utilizing an objective (without considering preceding elements) to focus the beam on the sample as a means to converge the previously collimated beam in a

region where the beam is at its smallest cross section, where it is neither converging or diverging (called the focal point) is used [11,18].

As a two-photon absorption event is dependent on two photons absorbing at the same location at nearly the same time (<1 fs arrival delay time), the probability of an excitation event is the multiple of the individual photons' probabilities of absorption, therefore excitation probability is dependent on the square of the excitation intensity profile, or I^2. This relationship below the objective is demonstrated in **Figure 1.4**, where the probability of two-photon excitation increases at an exponential rate as it reaches the focal point as a function of intensity squared, therefore, as intensity is doubled, the theoretical likeliness for excitation events or fluorescence produced is quadrupled. The point at which the probability for simultaneous absorption is represented by the peak, and thus decreases in the same form diverging from the focus, overall forming a sharp Gaussian curve.

Figure 1.4. Theoretical approximation for likeliness of a 2P excitation event. Diagram displays the focal point, forming a tight Gaussian-like distribution, where 'a' represents an arbitrary unit expressing the probability of 2P absorption.

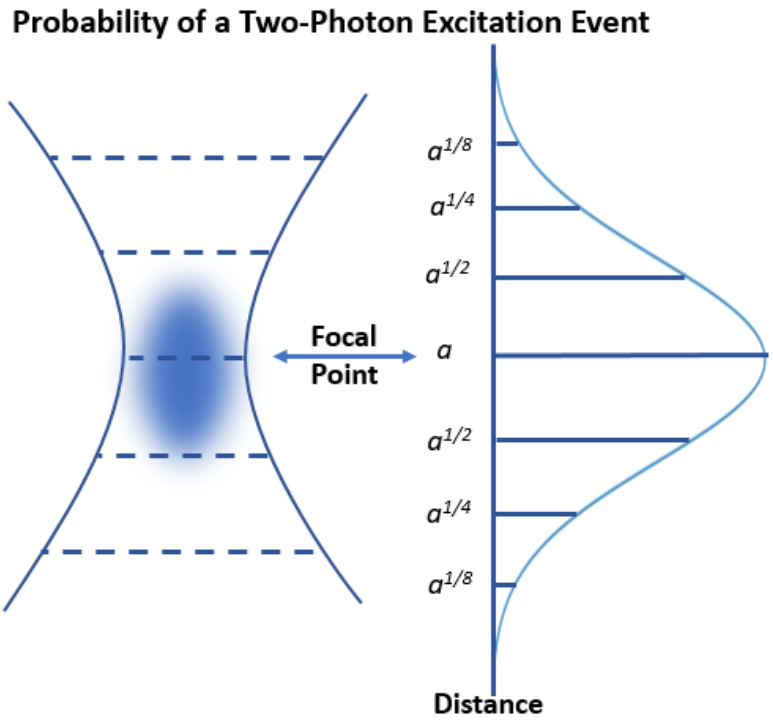

In addition to using cross sectional area the beam passes through to increasing the likeliness of an absorption event, the laser source is also femtosecond pulsed – emitting high energy bursts of photons rather than outputting a continuous beam. Doing so further increases the 'concentration' of photons delivered to the sample for only the duration of the pulse, thus creating a high (peak) power for the duration of a pulse. However, when averaged over a period of time accounting for effective power of 0 during the time between pulses, average power is not radically different than that of a continuous single-photon laser. Therefore with such a high frequency of pulses arriving per unit time, this pulsed nature of excitation does not deduct from the energy flux, rather, optimizes the delivery of a high concentration to increase the likeliness for an excitation event, while minimizing the potential for sample harm. In a typical

one-photon laser in continuous output mode, the sample experiences continuous irradiation, which in many cases can lead to sample saturation. Thus, the time between each pulse serves to mitigate the potential for sample damage as well as optimize likeliness for an absorption event during the arrival of the concentrated pulse of photons. The comparison between continuous and pulsed laser irradiation and a graphical representation of the two is presented below in **Figure 1.5**.

Figure 1.5. Theoretical representation of photon output vs time for 1P/2P lasers. Included in this representation is a visualization of continuous vs pulsed laser output.

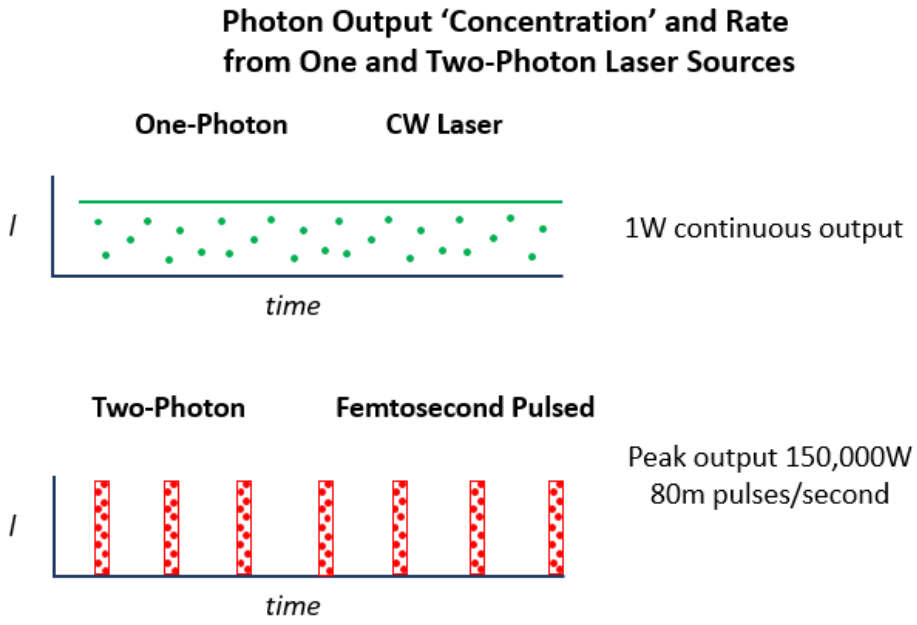

As the distance from the focal point increases, the likeliness of an excitation event exponentially decreases, therefore fluorescence emitted by the sample is localized to an area around the focal point in which photon concentration is the greatest, called the focal volume. The three-dimensional geometry of the focal volume is approximated by the point spread function (PSF). Calculation of the PSF, and

subsequently size of the focal volume, is simply achieved by following the calculation established by Richards and Wolff, in which they demonstrate that the PSF is a simple function of the lateral and axial-direction PSF radii [19,20]. The diffraction-limited lateral PSF radius with a NA higher than 0.7 and axial PSF radius are defined by **Equation 1.1** and **Equation 1.2** below [12,20]:

Equation 1.1. Lateral PSF radius ($\omega_{lateral}$), given Numerical Aperture (NA) is greater than 0.7.

$$\omega_{lateral} = \frac{0.325\lambda}{\sqrt{2}NA}$$

Equation 1.2. Axial PSF radius (ω_{axial}).

$$\omega_{axial} = \frac{0.532\lambda}{\sqrt{2}}\left[\frac{1}{\left(n - \sqrt{n^2 - NA^2}\right]}\right]$$

Where in a hypothetical instance, λ = 760 nanometers (nm), Numerical Aperture (NA) = 0.8, and n (refractive index) = 1.33 (where the medium is water). Solving the two functions above with the given variables, *ω (axial)* becomes roughly 1,069nm, and *ω (lateral)* becomes roughly 219nm.

With both axial and lateral resolution values, and the understanding that the multiphoton microscope focal volume encompasses points (x, y, z) in space about the focal volume that have an equal likeliness for an absorption event, the focal volume can be calculated as a function both directions of PSF radii, as shown in **Equation 1.3** below:

Equation 1.3. Two-photon focal volume (TPFV) of a two-photon microscope system.

$$TPFV = \pi^{\frac{3}{2}} (\omega_{lateral}^2)(\omega_{axial})$$

Following the calculation through with the previously obtained hypothetical lateral and axial radii values, the TPFV for the hypothetic multiphoton system with the given parameters would be roughly 2.9 x 10^8nm^3 [11,19,20].

The specific nature of the information derived from a system where excitation is highly limited to the focal area presents an addition benefit; the minimizing of unwanted signal from around the region of interest. Considering a range of biological components with optical absorption characteristics, such as protein, melanin and collagen in Figure 6 below, one can visualize an optical window between the ranges of 650-1200nm, in which the absorption of these components reaches a valley, or relative minimum [8,12]. In this region, termed the 'NIR biological window', the likeliness for an unwanted absorption event of just one of the incident photons is at a minimum [21]. This presents an ideal scenario for imaging deep into biologically complex samples where absorption only occurs at a significant order as two-photon absorption within the focal plane. Furthermore, it is well known that scattering is a function of $1/\lambda^4$, therefore, as wavelength increases, probability of scattering radically decreases [17,22,23].

Figure 1.6. Ranges of common biological absorbers and photon paths through tissue. (**A**), Theoretical illustration of 1P vs 2P absorption and scattering in a deep-tissue imaging situation (**B**). Tissue NIR absorbers graphic reproduced from the Beckman Laser Institute Diffuse Optical Spectroscopy & Imaging Lab at UCI. [24]

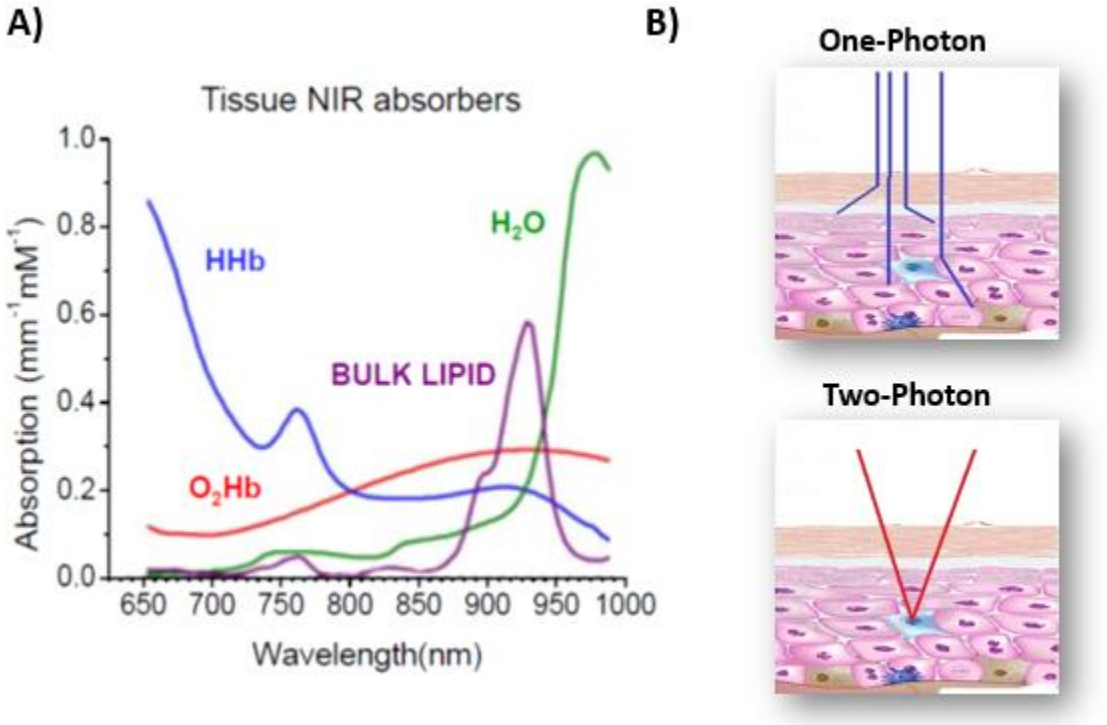

A theoretical illustration of these absorption and scattering properties are displayed in **Figure 1.6** above, comparing one to two-photon excitation for blatant demonstration of the strength of two-photo in specific imaging of deep samples. In one-photon excitation, the biologically complex sample presents a high likeliness to scatter and absorb at locations outside the focal plane, simply due to the nature of single higher energy photons directed at a sample buried underneath potential absorbers. In two-photon, the blue cell (sample of interest in the focal plane) is specifically excited due to the ease of the NIR photons traveling through the tissue, and only combining to create an absorption event at the focal plane. This ultimately positions two-photon as a highly advantageous tool for high resolution optical sectioning of tissue samples.

Overall, the optical parameters of two-photon fluorescence setups create an ideal system that minimizes unfavorable absorption and scattering, and optimizes the probability of only generating significant fluorescence from the sample of interest within the focal plane.

Chapter 2

DESIGN, CONSTRUCTION AND OPERATION

2.1. System Schematic

Figure 2.1. Tilbury Lab Two-Photon Microscope Schematic**.**

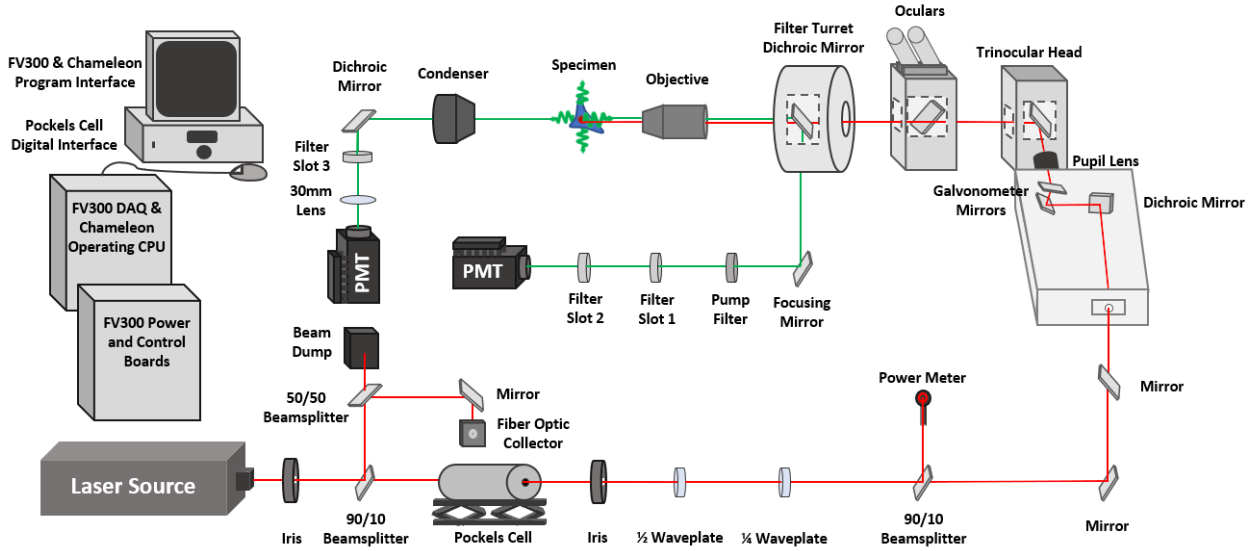

The Tilbury Lab Two-Photon system is a custom home-built system, converted utilizing microscopy components from an Olympus BX50WI confocal microscope stand and scanning unit. The system uses a mode-locked, Titanium Sapphire laser excitation source tunable from 680-1060, a Pockel's cell to modulate beam intensity, FluoVIEW FV300 scanning unit to focus the line scanned beam through the BX50WI stand. A custom mounted dichroic is employed to allow for two-photon excitation wavelengths to transmit through the filter turret, objective and illuminate the sample. Emission is directed by custom mounted optical components towards forward and backward directed photomultiplier tubes (PMTs). Images are collected with the FluoVIEW image acquisition software.

This chapter will review in detail the specific components of the microscope system, relevant physics, system design considerations and provide Standard Operating Procedures (SOP)s for the utilization and maintenance of the system.

2.2. Source, Power and Polarization

2.2.1. Source

As previously mentioned, to achieve sufficient two-photon excitation, a femtosecond-pulsed laser emitting between the wavelengths on the lower end around 680nm up to ranges between 1000-2000nm is necessary. In this system, we utilize a mode-locked Titanium Sapphire laser excitation source (Chameleon Ultra II; Coherent, Santa Clara, California). This powerful source is a femtosecond-pulsed, 80 MHz repetition rate tunable laser with a wavelength range from 680 to 1060nm. With an optimal power output (operating wavelength) at 800nm, the source has a maximum power output of roughly 3.4W. The overall laser system consists of a power supply, chiller, digital control interface as well as USB connection that communicates with the Chameleon computer program, allowing the system operator to control the various functionalities via computer program. Included in these functionalities is a shutter located just before the output bezel, allowing the laser to warm up and remain in a lasing state while turned on, without constantly emitting a beam [25].

With the shutter open, the horizontally polarized beam is first split with a 90/10 beamsplitter, allowing 90% of the beam to transmit and reflecting 10% toward a 90° flip mount mirror. When not in the path, the mirror simply allows the beam to strike a beam dump. When flipped upright, the beam is directed 45° toward an additional mirror, which is then again reflected 45° toward a fiber optic beam collector. With

this, the system retains the capability to send a portion of the beam through a fiber optic for use in an additional experiment setup.

2.2.2. Power

The portion of the beam transmitted through the 90/10 beamsplitter subsequently enters an electro-optic modulator Pockel's cell (ConOptics, Danbury, Connecticut). Depending on the use-case, a Pockel's cells can be used to alter beam intensity or polarization by introducing an electrical field longitudinal to the optical beam. In this system, the Pockel's cell works to modulate beam intensity through a process called 'Amplitude Modulation', where applying a voltage to the crystal will result in modulation of beam intensity exiting the Pockel's cell, controlling power as a sine-squared function of the applied voltage. Consequently, as the rotation of the Pockel's cell changes, the resulting applied sine function of voltage vs intensity changes. Ultimately, optimal alignment of the Pockel's cell depends on the application; in this system the purpose was to achieve the largest breadth of power modulation (e.g. largest range over which the user is capable of modulating the power by altering the applied voltage) - achieving this aligned state is discussed more in the respective 'Calibration and Alignment' section. The DC power supply controlling voltage applied to the crystal is equipped with a dial and digital voltage indicator, ultimately allowing the user to manually modulate beam intensity exiting the Pockel's cell, and as a result of passing through the crystal, this beam undergoes a halfwave shift (180°) in polarization [26–28].

Figure 2.2 Schematic of laser source, power modulation and polarization components. Physical (A) and cartoon schematic (B) illustration of laser source, power modulation and polarization controlling components, with beam path and respective beam intensity values overlaid.

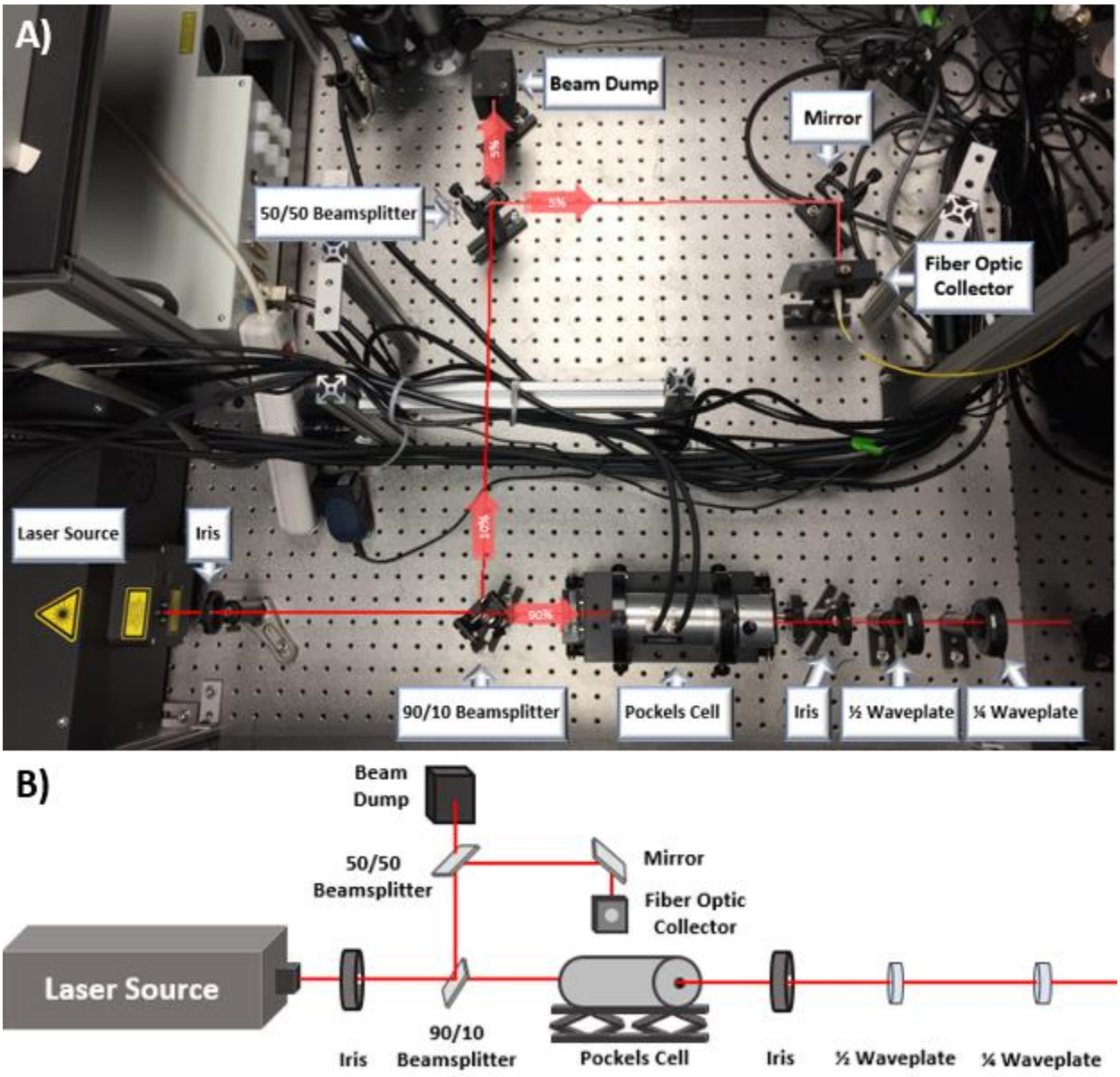

2.2.3. Polarization

As previously mentioned, many imaging techniques falling under the umbrella of multiphoton microscopy are polarization-sensitive, namely in this system, the use of SHG imaging. To account for this and allow for modulation of beam polarization, two waveplates are placed directly after the Pockel's cell. The first is a half waveplate, which alters the polarization angle of the beam by a function of 2θ, where θ represents polarization angle relative to the horizontal. As the waveplate rotates, it continues to modulate polarization following this function, allowing one to achieve a full 365° of polarization angle by rotating the waveplate 180°. In situations such as calibrating an SHG system to achieve the full range of polarization angles, or any other experimental setup where a specific angle is desired, a half waveplate in the path is an absolute necessity, as it converts circularly polarized light into linearly polarized light [29].

Followed by the half waveplate is a quarter waveplate, which simply converts the plane or linearly polarized beam into a circularly polarized beam. Circular polarization is the state in which electromagnetic field magnitude is constant at each degree of polarization angle, which was used in this system during imaging studies described in the following chapters.

Figure 2.3 Physical illustration of Pockel's cell and polarizers. Representation of beam polarization angle(s) is overlaid.

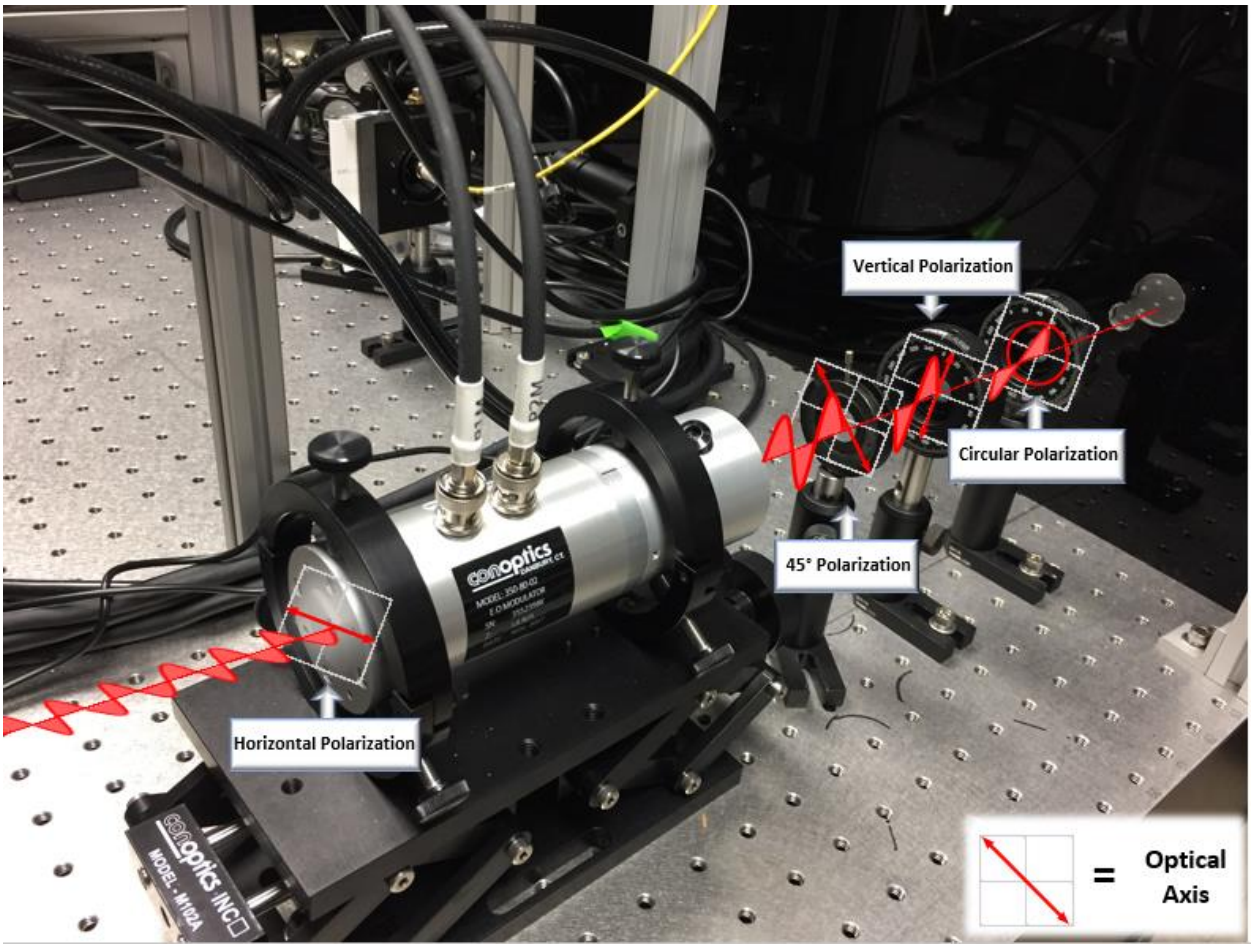

The transmitted light is reflected upwards at 45° towards a mirror, which reflects light towards the next portion of the optical setup, beginning with a FluoVIEW FV300 scanning unit (Displayed in **Figure 2.4** below).

Figure 2.4 Schematic of path through Pockel's cell, waveplates and FV300 unit. Cartoon schematic (A) and physical illustration (B).

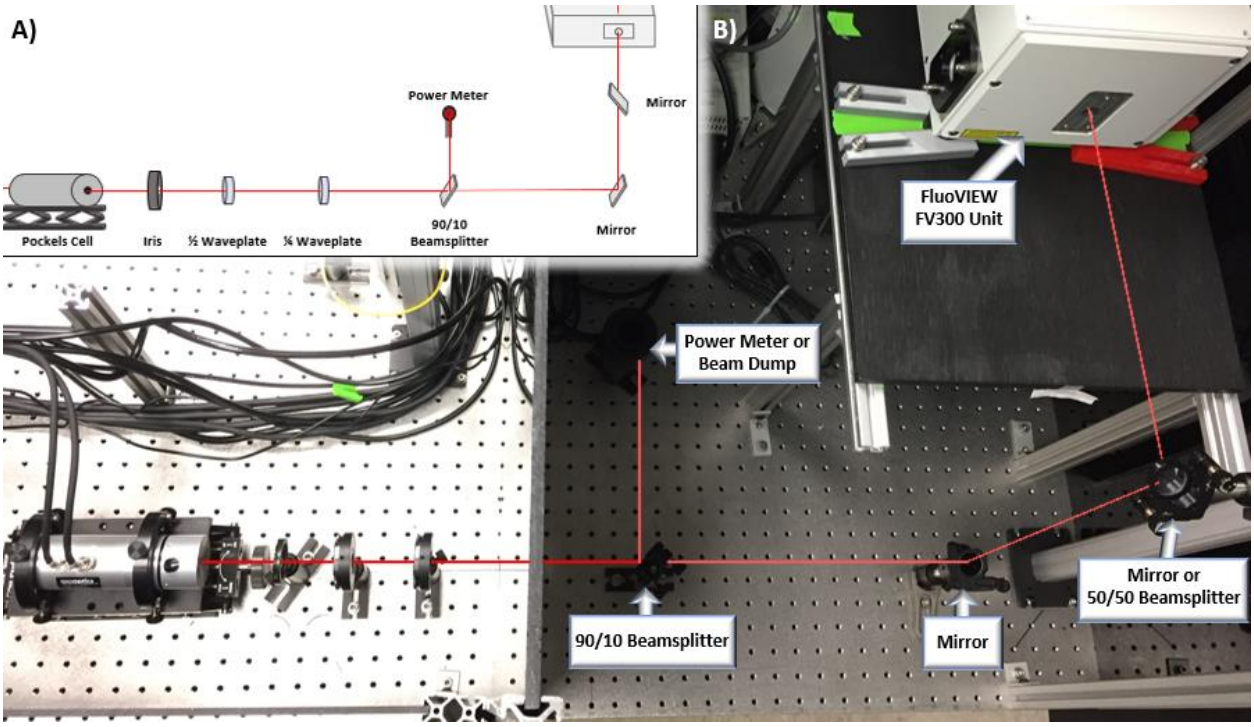

2.3. Scanning Unit, Microscope Stand and Sample Excitation

2.3.1. Scanning Unit

The FluoVIEW FV300 unit is a laser scanning unit typically utilized for confocal laser scanning units. For the multiphoton application, where line scanning is desirable, the FV300 is an ideal selection to do so while requiring only few changes to optics to achieve the desired two-photon laser scanning head.

The beam enters the FV300 through the longitudinal end (opposite the pupil lens) and passes through the system to strike a mount where a dichroic beam splitter can be mounted. These mirrors are mounted at 45° to divert the excitation beam towards a set of galvonometers, however, in the native FV300 setup are

tailored for one-photon fluorescence imaging, therefore, transmit >665nm light rather than reflect it towards the galvanometer mirrors. Therefore, it was necessary to remove the native filter and replace it with the custom mounted 665nm edge dichroic beamsplitter to allow for the two-photon excitation beam to be reflected (665nm edge BrightLine multiphoton single-edge dichroic beamsplitter, FF665-Di02-25x36, Semrock).

With this mounted, the excitation beam was directed 45° sideways towards a set of two galvanometer mirrors. Abbreviated 'galvos', these are perpendicular, rectangular mirrors that rotate in accordance to an applied voltage, which when rotating while reflecting a beam, have the ability to modulate the laser spot, and ultimately once rotating back/forth in unison, allow for line scanning across the eventual focal plane.

The first galvo is located at the bottom of the pair, with the face facing the dichroic mirror, which reflects the beam upwards towards the second galvo, which ultimately reflects the beam 45° towards the pupil lens. The pupil lens is the last optical component in the excitation path through the FV300, which aids in focusing to beam through the Olympus BX50WI stand, and to eventually slightly overfill the back aperture of the objective.

Figure 2.5 Schematic of beam path through FV300 unit towards trinocular head. FV300 galvanometer mirrors scanning the beam and pupil lens directing the beam into the trinocular head.

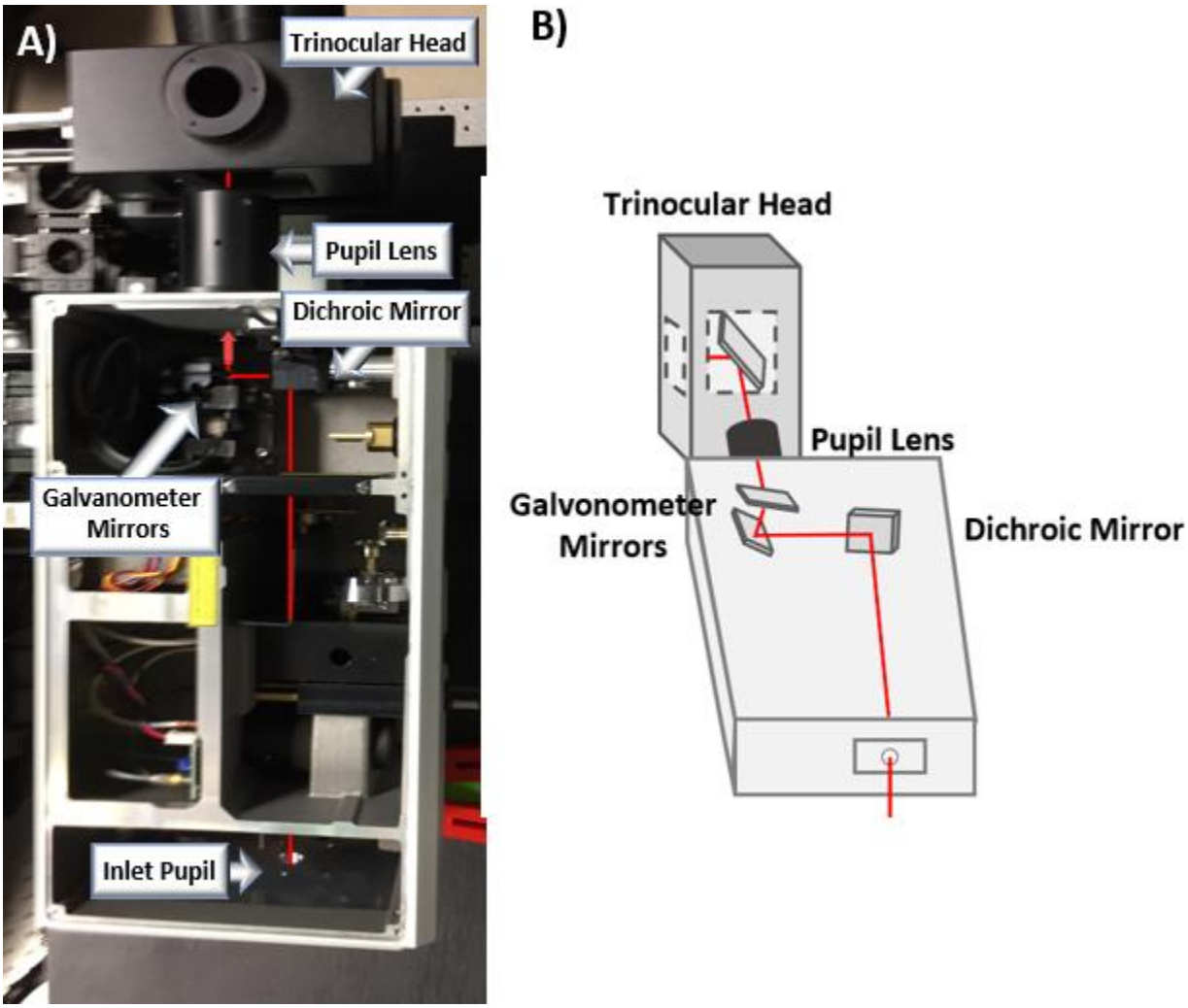

2.3.2. Microscope Stand

Following the FV300, the beam is directed into the trinocular head of the Olympus BX50WI microscope stand. Within the trinocular head, a set of prisms are housed which can rest in three positions; allowing for excitation beams to enter the system through multiple ports (side and top of the head). In this system, the FV300 is mounted horizontally adjacent to the side entrance to the head, therefore, the 45° angle

setting is positioned to divert the beam downwards toward the sample stage. In the initial overall multiphoton system design, only accounting for one and two-photon illumination through the same FV300 system, there is no source mounted to the vertical entrance of the trinocular head, and is therefore left empty – leaving the space available for an additional source which could potentially be coupled with the excess beam split by the second beamsplitter, for alternative experimentation purposes.

After being diverted downwards, the beam passes through another set of prisms, which rest in two locations and alternate to switch between allowing the excitation beam propagating downward to pass through towards the objective, or to allow an image generated through the brightfield channel to be viewed by the user through the set of oculars. Alternating between the two positions is discussed in more detail in the respective 'Operation and Maintenance' section.

Once the beam passes through the second set of prisms, it enters the filter cube turret, where the beam is met with a filter cube consisting of an excitation filter, dichroic mirror and emission filter. The excitation filter is a 532nm long pass, effectively eliminating any potential photons in the path from the laser pump, ultimately only allowing far red/near-IR excitation wavelength wavelengths suitable for two-photon excitation transmit. The next element is a 665nm edge dichroic beamsplitter which again allows wavelengths over 665nm to transmit for two-photon excitation, and reflects wavelengths below 665nm (665nm edge BrightLine multiphoton single-edge dichroic beamsplitter, FF665-Di02-25x36, Semrock).

Once passed through the dichroic filter, the beam exits the turret and enter the nose-piece rotating unit, to which objectives are mounted. The system includes a set of objectives; A 10x 0.3NA (air), 20x 0.45NA (air) 40x 0.8NA water immersion objective. For imaging purposes, the predominantly utilized objective was the 40x 0.8NA water immersion objective. When designing a microscopy system that passes a beam through an objective, it is necessary to consider the gaussian profile of the beam, where lateral beam intensity decreases moving away from the center. By underfilling, or passing a beam through an objective

back aperture with a diameter larger than the beam, will cause for a loss of resolution and decrease the effective numerical aperture. Therefore, the excitation beam should slightly overfill the back aperture, at the expense of a minimal loss of power.

Figure 2.6 Beam directed through microscope stand and objective focusing at sample. Cartoon schematic (A) and physical illustration (B).

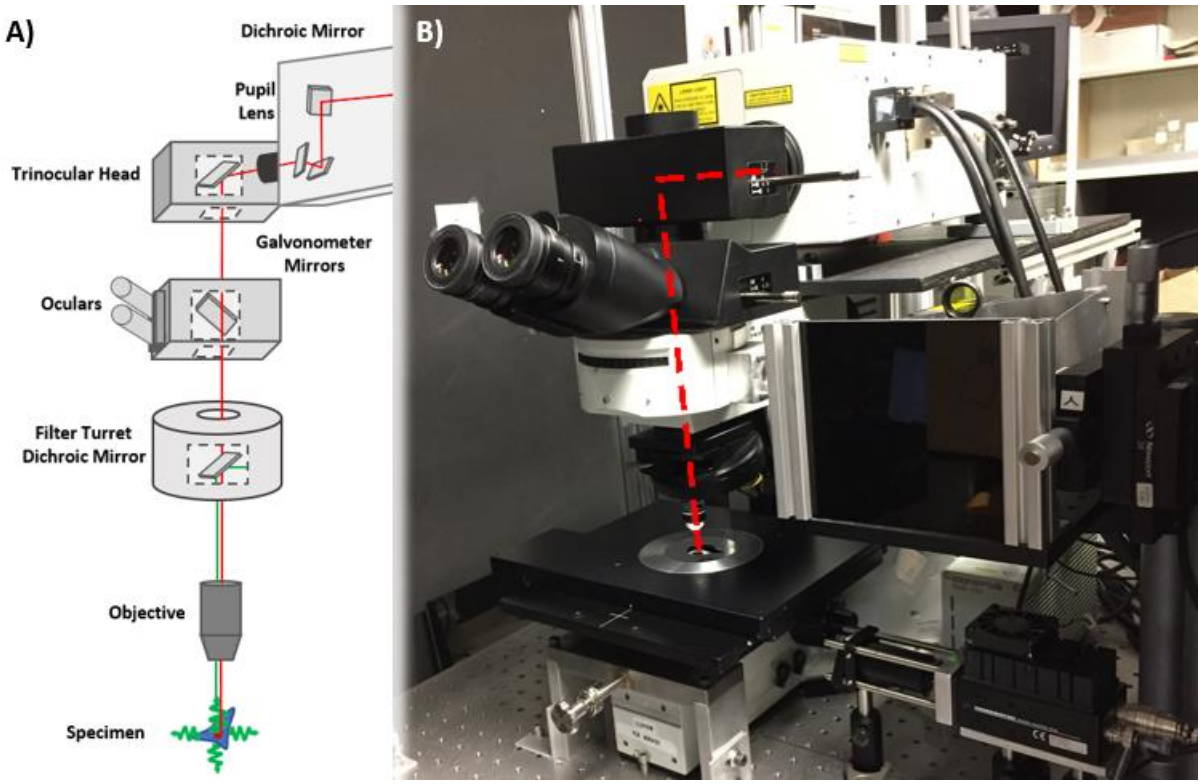

In this system the loss of power is not a significant concern, as the maximum capable system excitation power at the sample is much larger than necessary for imaging purposes, as shown **in Table 2.1** below, where a typical imaging power rarely exceeds 50mW. By placing a power meter in specific locations throughout the beam path, and calculating the ratio of values, transmission through the system is easily

quantified. To calculate transmission throughout this system, a power meter was placed following the waveplates and directly below the objective, and the ratio of the values obtained at 20 unique operating powers was calculated. The 40x, 0.8NA water immersion objective was utilized for this measurement, which possesses a back-aperture diameter of 0.35in and incoming scanned beam with diameter of roughly 0.3675in, representing approximately a 5% overfill ratio beam diameter to aperture diameter.

The average transmission through the system (FV300 through BX50WI stand) was calculated in this manner for typical imaging wavelengths; 760nm, 800nm and 890nm. It is notable that the maximum power of 890nm light at the sample (shown in **Table 2.1**) is significantly lower than the 760nm and 800nm excitation wavelengths, this can be attributed to the lower transmission through the system (shown in **Table 2.2**).

Table 2.1 Range of excitation powers for typical imaging wavelengths.

	At Sample	
Wavelength (nm)	**Minimum Power (mW)**	**Maximum Power (mW)**
760	0.2	163.5
800	0.3	191
890	0.4	49.5

Table 2.2 Average system transmission values for typical imaging wavelengths.

Wavelength (nm)	Transmission Through System (%)
760	87
800	90
890	27

Prior to sample imaging, it is necessary to roughly align the sample into focus and guide the objective to an imaging region of interest. After a sample has been prepared, it is placed under the microscope objective on a stage, which is manually translatable in the X, Y and Z axes. In the center of the stage is a stage opening, allowing for a path of light to exist below the sample. For viewing purposes through the oculars, a white light source was mounted at the rear of the microscope stand base, which transmits through a series of lenses at the bottom and is reflected 45° (upwards) by a mirror, up through a field iris diaphragm, and focused by a condenser located just below the sample stage. This illuminates the sample, achieving a brightfield image of the sample in the oculars, allowing the user to translate X, Y and Z coordinates of the stage and guide the sample into focus (the focusing process is described in more detail in the respective 'Operation and Maintenance' section). With the sample in focus, the appropriate prisms and filter cubes can be switched into the two-photon imaging positions, an image can be properly obtained.

2.3.3. Sample Excitation

Within the objective, the beam is focused through a series of lenses, and exits the objective with the beam continuing to focus towards a point in which the beam 'waist', or focal point where the beam is neither converging or diverging. At this point, photons are spatially concentrated to a focal volume in which the probability of a two-photon excitation events becomes of maximum likeliness to occur. The geometry of this three-dimensional volume is defined by the previously explained point-spread function (**Chapter 1 Section 1.4**). At the very center of the beam waist, the photon flux through the cross-sectional area is the greatest, representing the point in which the most two-photon absorption and subsequent emission events will occur – a specific distance away from the objective. The working distance of the microscope is defined as the distance between the final lens of the objective and the point at which the beam diameter

is at its smallest, or the focal point, as shown in the figure below. The working distance of the Olympus 40x 0.8NA water immersion objective commonly used in this system is 3.3mm [30].

With only the sample in the focal plane excited, fluorescence is emitted omnidirectionally, collected in forwards and backwards emissions pathways.

2.4. Emission and Detection

2.4.1. Backward Emission Path

Light emitted upwards from the sample is collected by objective and directed back toward the dichroic beamsplitter, which the excitation beam had transmitted through. As previously mentioned, the dichroic in place is mounted sideways at a 45° angle (relative to the front of the microscope base) in a fluorescence mirror unit slot, allowing light below 665nm to be reflected out of the turret towards a custom-built detector setup, retro-mounted to the side of the base (shown in **Figure 2.7B** below). Due to the height of the emission beam directed out of the turret at this location, the detector setup consists of a stage where optics were mounted, a network of optical rails to guide the setup into mounting position on base and mount the various optical components, X/Y translatable stages to adjust the alignment of the beam traveling through the optics, and a dense 1.5 in diameter non-magnetic cylindrical beam to stabilize the entire setup.

Within this setup (physical and schematic illustration shown in **Figure 2.7**), the beam is first met with a concave focusing mirror placed at a 45° angle that directs the beam backwards (relative to the front of the microscope base) towards a set of filters. Two filters are mounted in Thorlabs bimodal positioned motorized mirror flippers, allowing for the user to switch between filter sets by simply clicking the corresponding button to actuate the motor (MFF001, Thorlabs). Finally, once passed through a filter, the

beam reaches the backward-channel detector, a photosensor module, or photomultiplier tube (PMT) that is described in further detail in the following 'PMT' section (H7422 Series GaAsP Photosensor Module; Hamamatsu, Hamamatsu City, Japan). This PMT is mounted via circular RMS thread and oriented sideways to account for the tight spacing towards the rear of the microscope base.

Figure 2.7 Illustration of backward detection pathway of fluorescence emission. A) Emission traveling upwards toward the B) Dichroic mirror and directed horizontally toward the C) Custom mounted detector setup, which is reflected by a mirror through optical filters and strikes the PMT. D) Cartoon schematic of the entire fluorescence emission backward detection pathway.

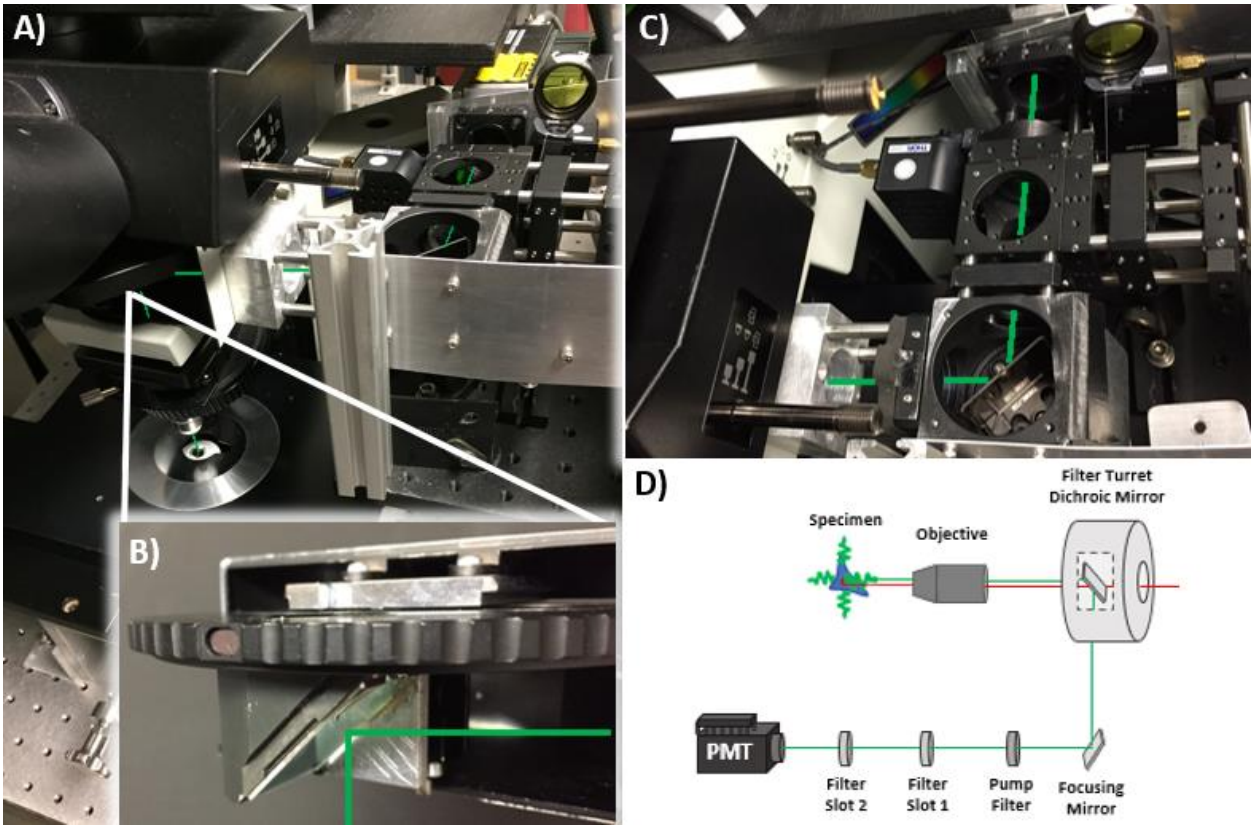

2.4.2. Forward Emission Path

The portion of the light emitted from the sample in the forward-direction is collected by an Olympus 'Long working distance' WI-UCD NA=0.8 condenser (air) and passed through an iris and directed toward the 665nm edge dichroic beamsplitter (transmits above 665, reflects below 665) mounted at 45° on a custom-built adjustable assembly. The assembly includes two base components that allow for the unit to be mounted via screws to the table, a 'bridge' component with a gap in the center of the rectangular cross section that allows a tightly-fitted rod to seamlessly slide forward and backwards, and the rod component to which the dichroic is mounted. Towards the front-facing side of the shaft is a clamp that serves to both stop the rod at the appropriate depth that allows the beam to strike the middle of the dichroic, as well as a pin that slides into a corresponding hole on the bridge component that locks to disable rod rotation (**Figure 2.8C**). The clamp can be loosened to adjust the angle of the dichroic mirror, thus adjusting the pitch of the beam reflecting away from the base. The reflected beam passes through an emission filter mounted on a set of optical rails, through a 30mm biconvex lens that focuses the beam onto the PMT detector, which has a circular detector face roughly 44mm in diameter (illustrated in **Figure 2.8E**). Numerous C-mount extension tubes are present, spanning the path between emission filter and detector, which prevent unwanted light to enter the system and obstruct image acquisition.

Figure 2.8 Forward direction emission pathway. A) Pathway view highlighting B) Custom mounted dichroic mirror and C) Dichroic mirror adjustment and fixation assembly. D) Physical illustration and E) Cartoon schematic illustration of forward direction emission beam path and optical components.

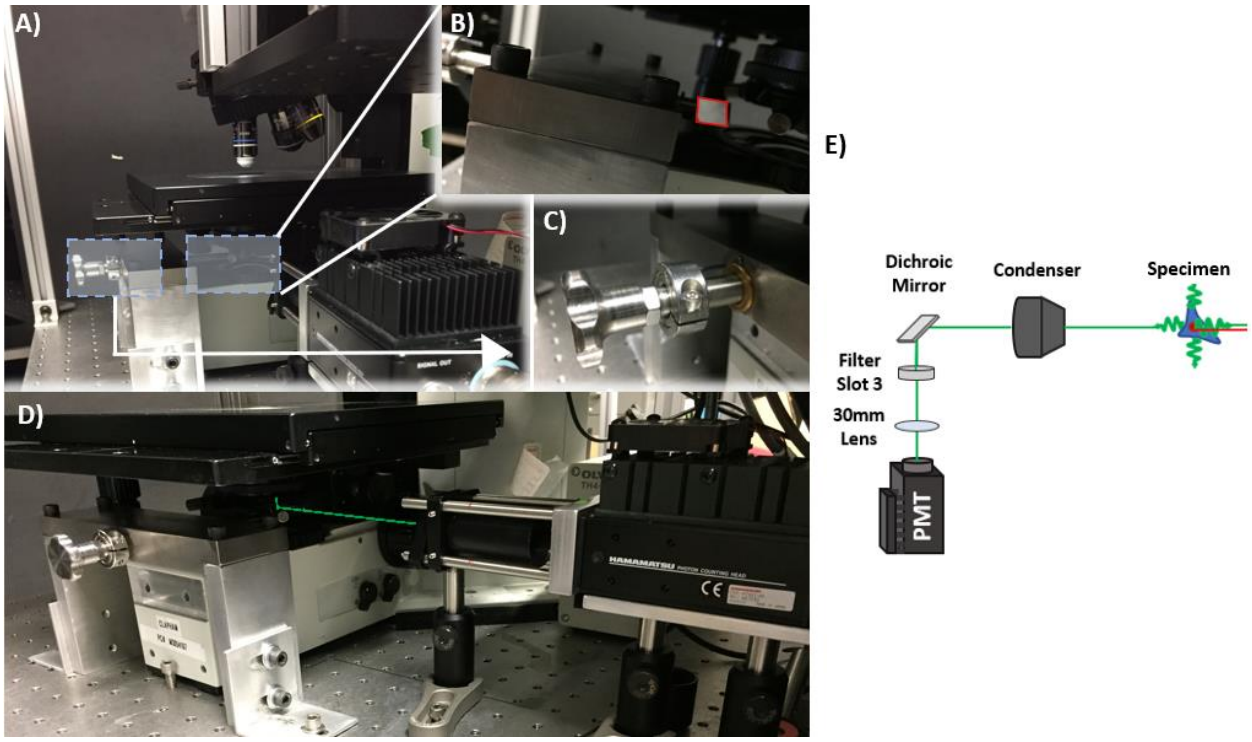

2.4.3. Photomultiplier Tubes (PMT)

A photomultiplier tube consists of a grid of detectors collecting photons emitted by a sample, digitized into an image with brightness of a particular pixel correlating to the PMT voltage (signal) generated by collected photons at that particular location on the detector. These collected photons are focused by an focusing electrode, and subsequently propagate down a cascade of dynodes and anodes. Upon striking the first dynode, the incident electron propagates a second photon, and together are accelerated toward the next dynode, where they both strike and in turn stimulate the acceleration of two more photons, and so on proceeding down the chain. The purpose of this electron multiplication is to amplify the incident

signal, significantly increasing the detector's sensitivity to incident photons. Upon traveling down the electron multiplying cascade, the current generated between the anode and ground is translated into photoelectron flux, and is read by an output meter and communicates relative amount of signal to the DAQ.

Signal intensity correlates directly to brightness displayed in an obtained image, where a pixel that has reached 100% brightness occurs when the rate of incident photons creating voltage exceeds the PMT working voltage generated in response to photons (PMT voltage no longer increases proportional to the amount of incident photons), therefore the detector dynamic range is completely filled -a point termed the saturation limit. No detected signal intensity is the simple case in which there is a lack of photons emitted by the sample sufficient to generate a voltage from the PMT any greater than voltage generated from read or dark noise.

2.5. Construction, Calibration and Alignment

2.5.1. Power Modulation by the Pockel's Cell

Proper alignment of the Pockel's cell is necessary to mitigate the potential to damage the device, and ensure an optimal breadth of power modulation is achieved. The Pockel's cell rests within an assembly of two rings with fine adjustment knobs located 120° apart from each other, with two positioned laterally on both sides of the tube, and the third located directly on top once the ring is closed. This mount allows for fine and user-friendly adjustment of Pockel's cell pitch and yaw. The alignment procedure is as follows:

Table 2.3 Pockel's Cell Alignment Steps

1. Before the cell is incorporated into the path, an identically shaped cylindrical alignment tool (provided with purchase of the Pockel's cell) is finely aligned to optimize pitch and yaw positions. The use of the tool ensures alignment can be performed safely without posing any risk of damage to the cell. To perform this, the tool is placed on the pair of rings, resting on the two bottom adjustment knobs in their lowest positions, which is supported by a translatable platform.
2. The laser is then set to 'Low Power Mode' (<200mW, to allow the user to safely work with the laser without damaging the Pockel's cell or alignment tool, as well as relieve the risk of working with an unnecessarily high intensity beam), and with the shutter open, one can identify extend of misalignment of the tool to the beam. Using the large adjustment knob for the platform, the tool can be raised to roughly align with the incoming beam. Fine adjustment of the tool is achieved using the bottom two adjustment knobs in each ring and is achieved when the beam can pass through without being clipped or distorted by passing through the cylindrical channel in the tool.
3. Once this state is roughly achieved, a power meter be utilized to first measure power of the beam entering the tool, and subsequently placed directly after the tube in the path, to measure any loss of power through the tool. Ideally no power should be lost, but in some cases the beam diameter is slightly larger than the entrance to the tube, so a small fraction of power loss may occur. Therefore, between 1-5% power loss is acceptable, granted beam profile and path is not distorted.
4. Once the analog tool has been aligned without distortion to the beam path and power, it can be replaced with the actual Pockel's cell. With the Pockel's cell in place, the pitch and yaw can be finely aligned with the adjustment knobs and power meter, and once re-confirmed to not obstruct the beam, the rings can be clamped down and the adjustment knobs located above the Pockel's cell can tighten to fix it in place.

Table 2.3 Continued

5. With the pitch and yaw alignment completed, it is necessary to adjust rotation of the Pockel's cell, because as previously mentioned, the degree of rotation can significantly alter polarization, and thus, the extent and range of the Pockel's cell's ability to modulate beam intensity. A rotational indicator, located on the front face of the Pockel's cell, can help direct the initial angle of the device – which in this setup is optimally found to be 45° displaced from the entering beam's polarization angle, which is horizontal. It is difficult to simply visually ensure Pockel's cell rotation to be in the perfectly optimal location, therefore, using a power meter once again is necessary. To identify the optimal rotational position, the Pockel's cell voltage, with laser beam passing through and striking the meter, should be modulated across the entire working range (0-495V), and minimum/maximum power values recorded.
6. After the trial and error process of rotating the Pockel's cell and adjusting pitch/yaw to optimize extinction ratio (ratio of maximum to minimum transmission directly following the Pockel's cell), which is ideally at least 400:1, the vertical fine adjustment knobs are tightened to keep the cell in place.

2.5.2. Beam Alignment Throughout the Path

Following Pockel's cell alignment, before modulating waveplate rotation to achieve a desired state of polarization (adding polarizers to the path will not obstruct beam trajectory), the beam must be walked up the optical mount and directed into the FV300 unit. At each stage of the path, it is good practice and important to mount mirrors in locations allowing the beam to strike the center and reflect at ~90° angles.

As the length of the path increases, and amount of optical components altering or occurring within the path, keeping beams located at the center of each optic allows for a clean trajectory and ease of future realignment, should a misalignment occur.

To ensure this, it is wise to 'walk' the beam through the system with a notecard and system of irises, ensuring the beam is collinear traveling through the path before inserting a new optic in it. Allowing the beam to travel its full trajectory increases the path length, and thus, will exaggerate a slight misalignment or confirm a well-aligned beam at location in the path. Each mirror in the path, and many of the optics native to the equipment employed, possess X/Y adjustment knobs to allow for such fine alignments to be made, accompanied by proper mounted position of each optic. A thorough means to achieve such 'straightness' (true parallel, perpendicular or 45° to a particular surface) is allowing the beam to strike a wall or ceiling, before obstructing the path with the next optical element. Knowing the location of the previous optic, one can place a visual indicator, such as a notecard with an 'X' on it, on the location of the surface at which the beam reflecting off the previous optic would be directed into perfect place. With this performed, it ensures that when placing and aligning the next optical component, it is only necessary to adjust the new optic, as the incoming beam is already aligned in its desired trajectory.

2.5.3. Positioning of the FV300 Scan head and Microscope Stand

The 'straightness' of the beam path becomes increasingly more important as it passes through the FV300 unit – needing to precisely strike the custom-mounted dichroic mirror in the translatable mirror unit, in the middle at the correct angle, so it can follow to reflect off the middle of the galvo at a precisely right angle. In addition to a cleanly horizontal beam trajectory, is it imperative to position the FV300 unit in proper location (X, Y, and Z axis) to properly transmit, reflect, and direct the line scanning light into the trinocular head on the microscope stand. As the trinoc is located at the top of the stand, it was necessary

to construct a platform to raise the FV300 to the proper height, to align and connect with the trinoc. The platform consisted of four 80/20 T-slot aluminum beams reinforced with brace pairs between adjacent legs holding up a platform which possessed screw holes for custom 3D-printed clamps to hold the FV300 unit legs firmly to the platform. In situations requiring fine adjustment of alignment of the beam in the FV300 unit, the mirror directing the beam into the unit was mounted on a simply translatable beam, requiring only adjustment of the mirror mount location (altering the beam height in the Z-axis) rather than altering X/Y angles of the beam. Additionally, the legs of the FV300 unit allowed for fine adjustment in height.

As the galvos transform the beam into a continuous line scanning mode, it becomes increasingly more difficult to confirm alignment by using a card to visually confirm on each optic. Once the beam has entered the trinocular head, is directed through the objective and focuses at the focal point, it reaches its full beam path length of approximately 2.75 meters. At this point, due to human error, it is likely that the beam has been experienced a slight misalignment, however, the beam aligned to a point where at least a portion is passing through the objective can be visually confirmed by placing a notecard below the objective at the focal point. With this, as the beam becomes more focus it appears as more of a point, allowing the user to easily discern between a rough state of alignment and misalignment.

2.5.4. Even Sample Illumination

As previously mentioned, it is near impossible to manage perfect beam alignment by solely manual alignment of beam. Even illumination at the focal plane is the ultimate goal, and therefore, is the final stage for excitation beam alignment. To reach this state, a sample consisting of an evenly distributed amount of fluorophores is required – allowing for an image to be taken that when properly aligned, will result in an image displaying equal pixel intensity across the entire image. To ensure even illumination in

this system, an autofluorescent slide acquired from Chroma was used (Autofluorescent Plastic Slide, Cat. No 92001, Chroma), emitting bright green fluorescence that allows for clear visualization of any slight misalignments. Acquired images from this alignment should be opened in a program such as ImageJ, where image cross sections can be plotted as histograms, and when evenly illuminated, should result in a flat line of pixel intensity across any designated section, as shown in **Figure 2.9**.

Figure 2.9 Evenly illuminated ROI (A) and Even pixel intensity across ROI (B).

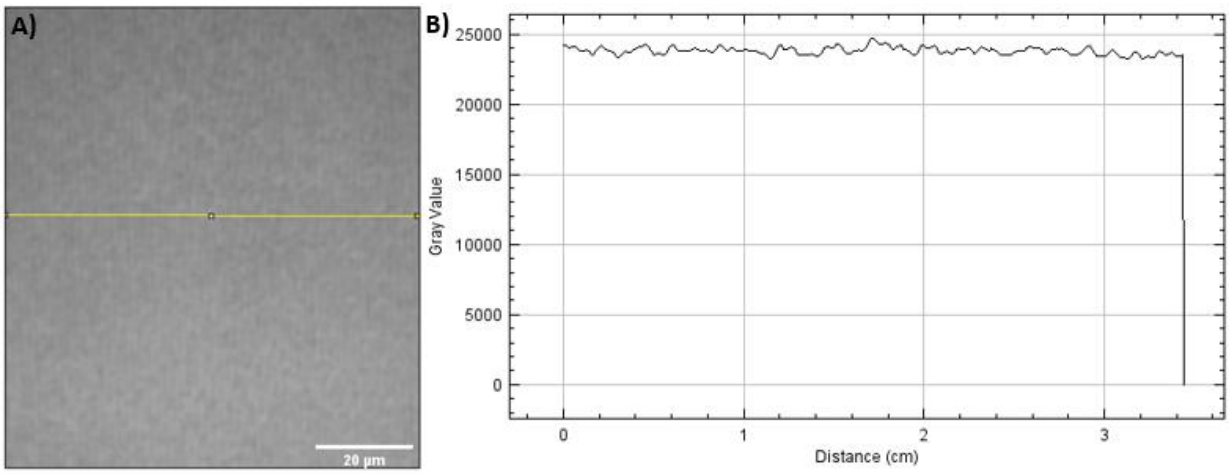

2.5.5. Ensuring Circularly Polarized Light

When the beam has been confirmed to evenly illuminate the sample at the focus, the angle or state of polarization can be altered by rotating both the half and quarter waveplates. For the purposes of initial image acquisition with this system, circular polarization was desired, and therefore needed to be achieved and confirmed. To do this, the simple concept of circular polarization power distribution can be applied; field intensity is equal at each degree of rotation. Therefore, by placing a polarizer below the objective, followed by a power meter, one can physically rotate through each degree and confirm even distribution

of power to the meter. With the half waveplate being the final plate in the path, and rotating the polarizer 360° and confirming no loss of power, circular polarization is successfully achieved and confirmed [28].

2.5.6. Axial Resolution

The longitudinal, or axial resolution of a microscope is its ability to differentiate between two distinct points (objects) in the axis parallel to the incident beam. This can be considered this as the distance between the nearest and farthest object plane in focus, calculated by the **Equation 2.1** below, which is a function of wavelength (λ), Numerical Aperture (NA) and refractive index (n). Sample values utilized reflect typical image acquisition parameters and are therefore representative of this system.

Equation 2.1. Axial resolution (*Δz*) of a two-photon microscope system.

$$\Delta z = \frac{1.22\lambda}{2\sqrt{2}NA} = \frac{1.22 \cdot (760nm)}{2\sqrt{2} \cdot 0.8} = 410nm$$

Where in a hypothetical instance, λ = 760 nanometers (nm), NA = 0.8, and n = 1.33 (where the medium is water). Solving for axial resolution produces a value of 410nm, or 0.41µm.

2.5.7. Lateral Resolution

As axial resolution is the microscope's resolution performance in the plane parallel to the optical axis, the lateral resolution, or the longitudinal resolution, is the microscope's resolving power in the plane perpendicular to the optical axis. As resolving power increases, the minimum distance between two points increases necessary for resolution as independent objects decreases. Spatial resolution is a function of wavelength and NA, calculated using **Equation 2.2** provided below (also reproduced from Benninger et al.) [31].

Equation 2.2. Lateral resolution ($\Delta\rho$) of a two-photon microscope system - given Numerical Aperture (NA) is greater than 0.7.

$$\Delta\rho = \frac{1.5n\lambda}{NA^2} = \frac{1.5 \cdot 1.33 \cdot 760}{0.8^2} = 2{,}370nm$$

Again, in this hypothetical instance, λ = 760 nanometers (nm), NA = 0.8, and n = 1.33 (where the medium is water). Solving for lateral resolution produces a value of 410nm, or 0.41µm.

2.5.8. Point Spread Function

To determine microscope PSF, a 0.175um bead was imaged and the histogram distribution of pixel intensity across the image, intersecting the bead was graphed. The sharp peak visible in **Figure 2.10** below was representative of the bead's intensity in the lateral plane. To understand lateral PSF, the FWHM of the peak was calculated, which was found to be roughly 0.434µm, or 434nm.

Figure 2.10 Lateral Point Spread Function (horizontal pixel intensity across bead ROI).

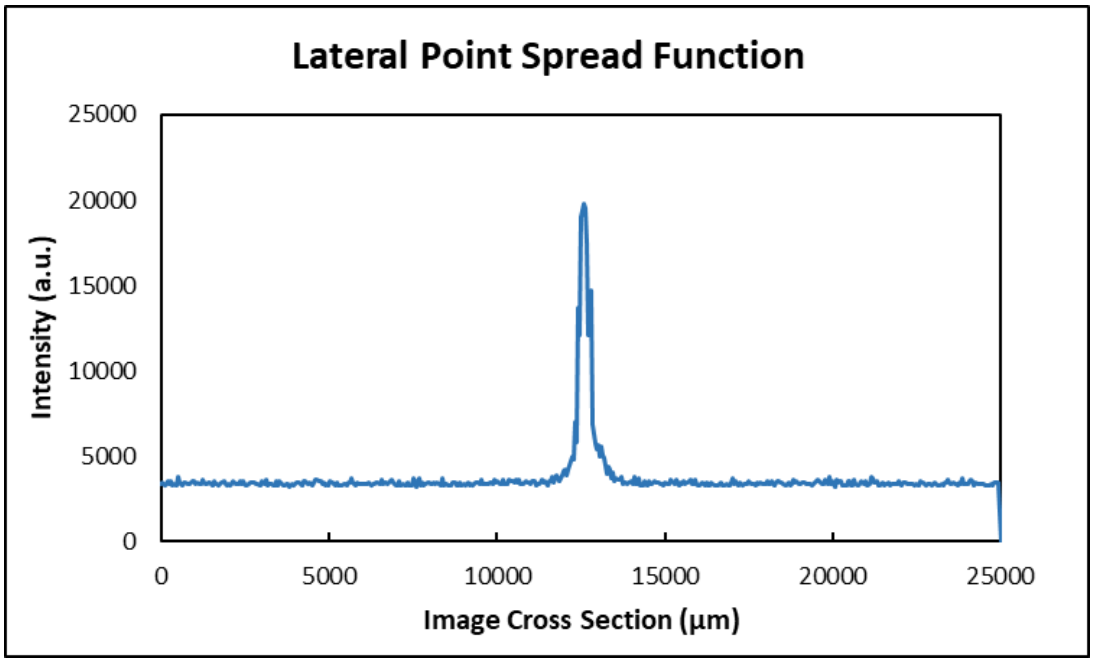

2.5.9. Power, Intensity and Energy Flux

Once constructed, aligned and calibrated, it is imperative to understand the systems performance both theoretically and physically, especially when performing experiments probing novel aspects of biological systems. With an understanding of system illumination/excitation properties, essentially a combination of an energy balance with a probability function, one can both generate a theoretical basis for the results of an experiment, have a basis for quantification and deductive problem solving in scenarios where an experimental result does not match a theoretical calculation or model. Numerous measurements describe aspects of the system's ability to excite a certain area, with a certain amount of photons, at a certain wavelength, for a certain amount of time – the three of particular interest are power, intensity and energy flux in the focal volume.

To begin with, power is simply a function of energy per second, therefore, should be the same throughout the entire beam path (unless obstructed by a filter, dichroic mirror, or minimal amounts of energy are scattered or absorbed upon contact with a surface or impurity), and is typically represents in Watts or Joules · seconds $^{-1}$. Intensity is a parameter of more interest, which is a function of energy per area and unit time, typically represented in photons per cm^2 s^1, or photons cm^{-2}s^{-1}. As this function possesses the area term in the denominator, as area decreases, intensity decreases, therefore, intensity is greatest at the point in which the area is the smallest, which is at the focal point. Energy flux through the focal area is calculated and discussed in more detail in **Chapter 4**.

2.6. Operation and Maintenance Standard Operating Procedures (SOP)

Table 2.4 Turning the system on

1)	Rotate the key on the Coherent power source (located next to the entrance door) 90° clockwise (to the horizontal position) so it clicks in place. While warming up, the Coherent laser power source digital display reads a 'Status: Power Ramping' message, which will remain for the 10-15 minute duration of the warm up cycle.

Table 2.4 Continued

2)	Turn on the Pockel's cell on with power switch on the front of the ConOptics power source. 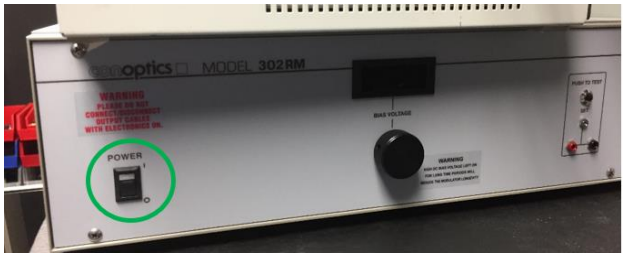
3)	Turn the desired PMT on using the power switch (in black), not the actuatable shutter (yellow). Additionally, when re-positioning the sample slide, it is good practice to turn off the PMT. See picture for PMTs corresponding to each pathway. 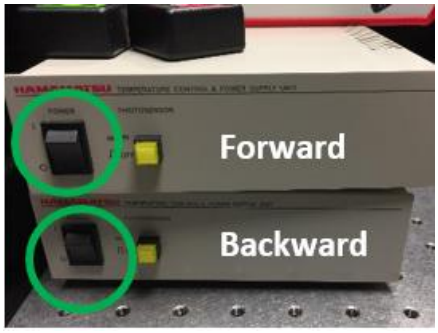
4)	Flip the 'Laser On' switch up (next to the light switch) located adjacent to the room entry door.
5)	Position the power meter head below the objective, within roughly 10mm of the objective to ensure the entirety of the beam strikes the meter. Turn the power meter on and ensure it is set to measure power of 760nm light.
6)	Begin scanning the beam (using the XY repeat button on the FV300 software). Record the highest observed power (stored and displayed below the 'current power' on the meter digital interface).

Table 2.4 Continued

7)	Reference recorded power of previous imaging sessions to ensure the power is consistent. 

Table 2.5 Turning the system off

1)	Close the PMT shutter and laser shutter.
2)	Turn the PMT off, then the Pockel's cell, then rotate the Coherent power supply key back to the vertical position.
3)	Lower the stage and remove your sample. Clean the objective by swiping with 50/50 Methanol/Acetone soaked lens cleaning paper.
4)	Flip the 'Laser On' switch down, turn the lights off.

Each day, it is important to ensure the path of the laser beam is aligned and evenly illuminating the sample.

To do this we follow standard daily alignment procedures:

Table 2.6 Daily Alignment

1)	Place one of the Chroma fluorescent slides under the microscope, using water to immerse the objective. Use the dark blue slide with an excitation wavelength of 760nm, using the 448/20nm bandpass filter in both backward and forward channels.
2)	For the backward channel, ensure the knobs and dichroic slider are properly positioned to direct the beam towards the backwards PMT (Ocular trinoc knob in the farthest-out position). For the forward channel, ensure the custom dichroic mirror below the stage is in place.
3)	Launch the Coherent GUI and FluoView software. Turn off the lights.
4)	Open the backwards PMT shutter, open the laser shutter on the Coherent software, and press 'XY scan' on the FluoView software to begin scanning.
5)	Adjust the stage Z-position until either the fluorescence from the slide is visible by eye (can use eyes to guide rough approximation for appropriate Z-height), and make sure the fluorescent area is visible on the FluoView viewing window. This image should display similarly to the image provided below:
6)	Take an image on the Kalman (4), slow scan speed settings at 3x zoom. To do this, configure the proper settings and take the image by pressing 'Once' next to XY scan. Make sure the circle is positioned in the center of the image (If this is not the case, adjust the horizontal and vertical knobs on the detector mount to center it). Save this image
7)	Close the backward channel detector and repeat this process taking an image in the forward channel. Open the forward channel shutter, switch the FluoVIEW selected 'Channel' from Channel 1 (backward) to Channel 2 (forward), and take an image with the identical settings. Save this image and upload both to ImageJ.

Table 2.6 Continued

8)	In ImageJ, draw a line across the circle, and select the Plot Profile function under Analyze (or press Ctrl+K). 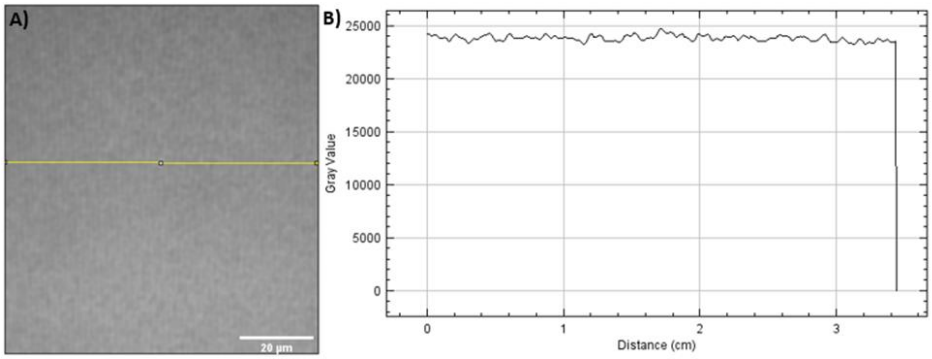
9)	Ensure that the intensity profile demonstrates even intensity across the sample.

Table 2.7 Daily Use

1)	Clean your desired objective by swiping with 50/50 Methanol/Acetone soaked lens cleaning paper.
2)	Place your sample under the objective, and lower until the objective the surface of the aqueous layer of the samples' surface tension creates a column connecting the sample to the objective.
3)	Adjust the knobs and dichroic slider to allow for viewing of a bright field image, and turn on the lamp to enable bright field.
4)	Adjust the Z-axis height to focus the sample in the oculars, move the sample with the X/Y stage translation knobs (left of stage) to focus on your sample or region of interest (ROI).

Table 2.7 Continued

5) Once focused, turn off the lamp and re-adjust the knobs and dichroic slider to direct the light towards the backwards detector.

6) Close the system door, and turn off the lights.

7) Open the laser shutter, PMT shutter and begin XY scanning. Adjusting stage height to focus on the sample will likely be necessary due to a slight difference in focusing length/image size between the oculars and PMT optical paths – use the double arrow on the FluoView interface to move the stage. This is most easily accomplished at FluoVIEW settings: 1-2x zoom, with fast/medium scan speed, at relatively high power (so the sample easily comes into view as you scan through the height).

8) Once focused, adjust the scan speed to slow, scan type to Kalman (4), zoom to at least 2x (typically for cell culture, 3x zoom), and make sure the proper filter is in place (switch with red/green buttons located on top of Pockels cell power supply).

Typical Image Acquisition Settings	
Parameter	**Value/Setting**
NA	0.8
Magnification	40x
Immersion	Water
Zoom	3x
Field Size	85um x 85um
Pixel Dwell Time	20us

Table 2.7 Continued

9) Begin scanning with XY scan. Adjust the power by increasing the PMT voltage on the ConOptics power modulator. Bring the power to a point where the sample is emitting adequate signal, but not saturating the detector (to ensure saturation is not occurring, utilizing the lookup table to Hi-Low provides an intuitive interface, where maximum signal/saturation is displayed as a red pixel) (display in the image below, a saturated vs non-saturated image).

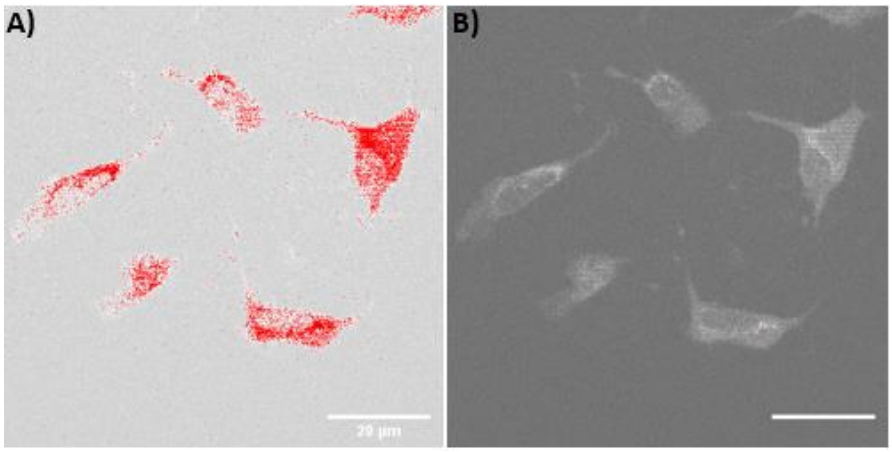

Alternatively, if the sample is easily damage by high-power excitation, bring the power to a point where sample emission is filling as much of the detector dynamic range as possible, without incurring any sample damage.

10) Once the ideal power has been identified, take an image using the FluoVIEW settings from step 8, by pressing 'Once' at the top of the interface. Once the image is acquired, press 'Save Experiment', and save to the folder corresponding to the date. Folder naming: Folder: Project Name Sub-Folder: Month (2 digits), Day (2 Digits), Year (Last 2 Digits) e.g. June 11th, 2018 → 061118

File Folder: Sample Name, Image Acquisition Settings

Table 2.7 Continued

11)	For each saved image, record the power (Pockel's cell voltage), zoom (FluoVIEW) and lookup table value (FluoView) in a lab notebook. Also record sample and time of imaging, along with any irregularities noticed during imaging.

2.7. Maintenance Standard Operating Procedures

On a day-to-day basis, environmental factors such as air pressure, humidity, temperature, air quality and cleanliness can lead to slight but significant alterations to the performance of the system. Due to this, there are a number of maintenance practices that should be performed on a regular basis.

For a number of reasons, including functionality of the laser, Pockel's cell, and beam alignment, it is possible that the power of the beam below the objective (focused at the sample) can experience slight to drastic alterations. This parameter should be measured daily, prior to performing any type of imaging. This process is simple, following the steps provided below:

Table 2.8 Excitation Power

1)	Place the power meter below the 40x objective at a distance where the beam appears to come to a focus on the face of the meter, without touching the meter to the objective.
2)	Turn the power meter on, ensuring the meter is set to record power at the designated wavelength (760nm).

Table 2.8 Continued

3)	Open the laser shutter and begin scanning the beam at 760nm with the Pockel's cell set to 250V. The width of the beam should fit entirely on the face of the meter, if not, focus the beam until the power meter is reading power from the entire diameter of the beam.
4)	The power should range between 31-32mW.

Similar to causes of an alteration in excitation power at the sample stage, if an optic is accidentally bumped or tampered with, or an environmental condition skews the beam path, it is highly likely that the beam will fall out of alignment over time, thus no longer evenly illuminating the sample. It is critically important to remain in such a state, to ensure a lack of aberrations, maintain resolution and contrast. Ensuring even illumination is achieved by simple:

Table 2.9 Even Illumination

1)	Placing a sample or slide under the objective with an evenly distributed amount of fluorophores throughout the optical window. In this system, Chroma plastic fluorescent slides are utilized.
2)	Focus the sample, illuminate at the optimal wavelength, and take an image (with slow scan speed and at least Kalman 4 mode) recording emission through the appropriate emission filter.

Table 2.9 Continued

3) Export the image to an image processing program such as ImageJ, that allows one to draw a line across the image and plot a histogram of intensity distribution. Doing this allows for a direct understanding of the excitation alignment characteristics of the beam, as emission signal should be evenly distributed across the field of view. A binned or averaged histogram should result in an even distribution of signal, such as the image and resulting plot viewed below. 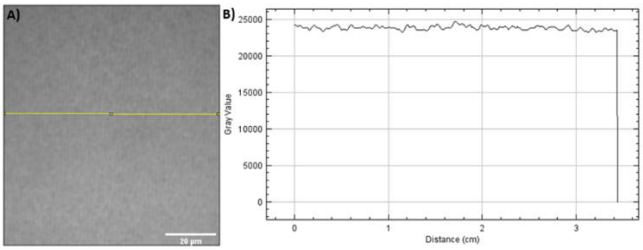

Finally, due to regular use, environmental conditions changing overtime and removing of external enclosure components allowing for particulates to easily enter the system, cleaning the optics on a regular basis is a best practice necessary for ensuring full functionality of the system. Cleaning optical surfaces is a quick and simple task:

Table 2.10. Cleaning Optics

1) Fold a sheet of lens paper to the appropriate dimensions and grasp with a set of forceps.
2) With an eye dropper, wet the cleaning surface of the lens paper with a 50/50 mixture of methanol and acetone.

Table 2.10 Continued

3) Gently rub the optical surface back and forth several times with the wetted lens paper, to ensure particulates are removed and faces are clean. Check after cleaning that a film or residue was not formed on the optic.
4) When cleaning an objective, remove it from the revolving nosepiece, and firmly secure the objective upside down (to access the side interacting with the sample) for cleaning in the same fashion.

Chapter 3

APPLICATIONS IN SINGLE-CELL OPTICAL METABOLIC IMAGING

3.1 Introduction

For an array of single-cell biological applications, two-photon fluorescence imaging is a particularly suitable tool; as the technique minimizes the potential for undesirable scattering, allows for imaging multiple hundred microns deep into a material, and excites fluores on a wavelength specific basis, producing high-resolution images on the scale of tens of microns.

In this work, the applications of single-cell optical metabolic imaging and deep tissue imaging were explored. In particular, optical metabolic imaging was applied to the study of cancerous cells response upon dosage with a potential novel anti-cancer candidate, and deep tissue imaging was performed to investigate the potential to image three-dimensional cellular growth into novel biomaterial scaffolds.

3.2 Optical Metabolic Imaging

3.2.1 Cellular Metabolism: Healthy and Cancerous

Cancer is a debilitating disease affecting millions around the world; in the U.S. over 1.7m people were diagnosed with new incidences of cancer, and cancer was the causal factor of over 600,000 deaths [32]. It is well known that cancer is a disease elusive to a number of treatment options, as it manifests as a result of a range of pre-conditioning factors; genetic, environment factors, nutrition, leading to a difficulty to pinpoint the pathology source and devise effective treatment modalities on a patient-specific basis. Fundamentally, cancer is known to manifest as a result of uncontrollable cellular division and growth,

typically consuming tissue and harnessing streams of normal physiological function to spread and form a tumor mass [33]. As a result of decades of translational work by biochemists, physicians and engineers, cancer metabolism is becoming increasingly understood.

To begin with, cells 'digest' substrates such as glucose for the purpose of producing ATP – the body's source of energy. It is well known that ATP production in healthy cells can occur through several pathways; oxidative phosphorylation (OxPhos) in aerobic conditions (oxygen present), and through glycolysis in anaerobic conditions. The entire OxPhos pathway first involves the entering of glucose through the cell membrane via GLUT-1 receptors, the subsequent breakdown of glucose into pyruvate through glycolysis, as well coenzyme nicotinamide adenine dinucleotide phosphate (NADH) production during glycolysis that serve to transport electrons to the inner mitochondria (later in the process) [34]. Next, pyruvate is converted into Acetyl-CoA, which further allows for reduction of flavin adenine nucleotide (FAD) into FADH, thus allowing both end products to fuel the electron transport chain (ETP). Acetyl-CoA feeds directly into the Krebs cycle, and the $FADH_2$ and NADH (from glycolysis) are transported through the inner mitochondrial wall and donate electrons to the ETP. Utilization of the protonated forms of coenzymes $NADH_2$ and FADH are critical to maintain an even charge gradient across the mitochondria, for oxidative phosphorylation to occur. At a high-level, through this process, 36 ATP are generated in an aerobic environment, and in an anaerobic environment, the pathway will halt at the end of glycolysis [35,36].

Cancerous cells, however, exhibit a shift in cellular metabolism different from these typical pathways; in the presence of oxygen, cancerous cells with revert to glycolysis, instead of OxPhos, which is termed anaerobic glycolysis. This reprogramming in the metabolic pathways of cancerous cells was discovered in the early 20th century by Otto Heinrich Warburg, a German physiologist. He found that despite the oxygen-enriched environment, therefore oxygen was available for utilization in OxPhos, that cancer cells displayed enhanced rates of glycolysis [37,38].

In these cells, the GLUT-1 receptor, which is responsible for the transport of glucose across the membrane into the cell, is radically overexpressed. In turn due to the increased amount of glucose entering the cell, the amount of glycolytic reactions (glycolysis) is significantly increased. Glycolysis products, reaction intermediates and resulting environmental changes, such as production of lactate and decrease in pH, are also significantly enhanced – leading to an array of pro-tumor environment factors. This shift in cancer metabolism towards aerobic glycolysis, leading to the uncontrollable and unregulated growth of cancer cells, is termed the Warburg Effect [38–40].

3.2.2. Optical Redox Ratio (ORR) Background

The importance of the need for protonated states of the coenzymes NADH and FAD have been integral to the study of healthy/pathological cell metabolism. Accompanied by the increased rate in glycolysis is the buildup of NADH, which with the lack of oxygen is not utilized by OxPhos in the mitochondria, therefore builds up in the cell. Knowing the need for each state in the ETP, Chance et al demonstrated that it was possible to record relative abundance of the coenzymes using the de-pronated forms' autofluorescence signal, in an effort to time and space resolve measurements for oxidation-reduction states on a signal cell level. In his work, Chance utilized the fact that reduced NADH has a stronger fluorescent signal over the oxidized NAD, and FAD exhibited more intense fluorescence than FADH. Conveniently, both fluorescence signatures are spectrally independent from each other, therefore, can be measured independently. With the significant accumulation of NADH in hypoxic cells, the shift in ratio of the NADH to FAD in healthy vs pathological cells is profound. This ratio has come be to termed the optical redox ratio (ORR), and has become a useful readout to probe a number of characteristics of cellular function and state [39–41].

Since the groundbreaking work performed by Chance, many research groups have adopted their own quantitative metrics for the ORR (different ratios and normalization procedures of NADH to FAD), all

relying on the same underlying concept [40]. Such previous work, pertaining to this study, has demonstrated the ability to non-invasively image cell ORR using various microscopy methods, *in vitro* and *in* vivo, to quantify alterations in cell metabolism in various stages of development, cellular function and response to a stimulus. Particularly relevant work has involved the attempt at early diagnosis of cancerous masses and the prediction of dose-dependent ORR shifts in pathological cells when dosed with therapeutic drug molecules [42,43].

Early ORR work with microscopy systems involved studies such as the observation of decreased ORR in human papillomavirus immortalized cells compared to non-infected, normal epithelial cells, and alterations in ORR intensity and spatial localization in human epithelial cells upon dosage with common chemotherapeutic, cis-platin [44,45].

Numerous studies have utilized confocal microscopy to predict and quantify cancerous cell response to therapeutic dosage with candidate molecules.

3.2.3. Single-Photon ORR

Nimmi Ramanujam's group performed optical ORR analyses that differentiated healthy human mammary epithelial cells from breast cancer cells, and further demonstrated a decrease of ORR in cancer cells dosed with the therapeutic, taximofen [46]. Alhallak et. al. investigated the ORR alterations in cell lines with increasing metastatic potential, by altering the normoxic and hypoxic conditions, ultimately indicating that ORR is sensitive to metabolic flexibility of cancer cell lines that exhibit dynamic changes in metastatic potential [47]. Zhang et. al. showed that the ORR can also be a quantitative metric to predict the effectiveness of photodynamic therapy, further substantiating the amounting evidence that ORR can be used to predict effectiveness of a wide range of therapeutic strategies [48]. The use of ORR has even been

demonstrated to be highly translatable, with work performed such as Yu et. al. who developed and validated a microfluidic system suitable for ORR imaging for the label-free, swift, non-invasive metric for drug screen and toxicity testing, with ORR results that were confirmed by traditional cell viability assays [49].

While proving to be highly viable in 2D cell culture studies, work progressing to evaluating ORR shifts in 3D culture and tissue samples suffered from previously mentioned downfalls of confocal (e.g. out of focus irradiation and superficial depth of penetration) which were magnified by the relatively low intensity of NADH/FAD fluorescence compared to commonly used fluorescent tags, and 3D stacks quickly became superficial due to complex overlapping spectral bands of absorbers in tissue [50–52]. Therefore, the use of two-photon microscopy to study ORR became of significant value.

3.2.4. Two-Photon ORR

Two-photon allows for the highly condensed and specific illumination of low-intensity emitters NADH and FAD, therefore optimizing collection of spatially and spectrally specific photons. The absorption of NADH and FAD occurs optimally around 350nm and 450nm, with emissions around 460nm and 535nm, respectively. Finally, usage of two-photon allows for farther depth of penetration into tissue samples, allowing for a viable and confident RR readout of up to 400um thick tissue sections [50]. Due to this, an array of two-photon based ORR studies have been performed the last two decades.

Wu et. al. used an array of two-photon quantitative metrics and signal including ORR and second harmonic generation (SHG) for the comparison between breast cancer tumors and surrounding microenvironment ORR and morphological changes, and found combined analyses to be a potential novel method for observing therapy efficacy [53]. Irene Georgakoudi's group applied the use of two-photon based, single-cell

ORR for the characterization of cellular metabolic changes in 3D engineered tissues, finding that in the initial stages of cell growth into matrices, a decreasing ORR is correlated to stem cell differentiation and lipogenesis, offering a label-free approach to aid in the optimization of tissue engineering [50]. In addition, Georgakoudi also demonstrated the use of deep-tissue two-photon imaging to differentiate 'live, engineering normal and precancerous squamous epithelial tissues' based on ORR, associated both with glycolysis and glutamine consumption [54].

Skala et. al. has performed a wide range of studies demonstrating the utilization of optical metabolic imaging (OMI) for therapeutic screening applications, such as the inhibition of human epidermal growth factor receptor 2 (HER2) in breast cancer cells lines that led to a stark decrease in ORR, the demonstration of correlation between OMI and glycolytic levels in numerous breast cancer cells lines, coupled with *in vivo* breast cancer xenografts in mice using OMI as an endpoint for determining efficacy of trastuzumab treatment, as well as the identification of single-cell tumor cell-cycle status *in vitro* and the prediction of drug response by OMI in breast cancer 3D organoids [42,52,55,56].

3.3. ORR Imaging Study Motivation: Hemocyanin

3.3.1. Hemocyanin Structure and Function

The application of ORR imaging in this study was to investigate the anti-cancer potential of the oxygen-transporting protein found in lobsters, called hemocyanin. Hemocyanin, functioning similarly to hemoglobin, with several structural differences including a binuclear copper ligand 'active site' instead of iron, is responsible both for oxygen transport throughout the circulatory system, as well as immunogenicity of the lobster. The molecule is composed of the copper site that reversibly binds oxygen, surrounded by histidine molecules and ultimately is encased by large glycosylated moieties containing

several orders of subunit aggregates; hexamers, oligomers, '24mers'. The order and amount of subunit aggregates varies among arthropod species, with lobster hemocyanin composed primarily hexamer and dodecamers [57,58].

On the surface of the hemocyanin molecule lay a significant number of hapten-binding sites, which play a critical role in its function as an immune glycoprotein. This characteristic of hemocyanin has led to its frequent use in immunogen preparation, as an immunostimulant and carrier protein [59,60]. These proteins are used in antibody preparation, enzyme-linked immunosorbent assays (ELISA), as well as for therapeutic applications as an adjuvant to stimulate immune response [61]. For decades, the dual role as a carrier protein with immunogenic potential has been utilized and become increasingly more well characterized on various animal models, which has led to its primary commercial function as a carrier protein used in vaccine development [31,62–65]. This work has been performed primarily using hemocyanin from a marine mollusk called the giant keyhole limpet.

In mice and murine models, targeted therapeutics have been conjugated to hemocyanins such as KLH, measuring endpoints such as immune response and tumor volume [62,64,66–68]. KLH is now estimated to be used in over 15 vaccine clinical trials for cancer, lupus, lymphoma and Alzheimer's [68,69].

Unfortunately, heavy harvesting of the keyhole limpet warranted several EPA regulations for harvesting volume, just after the market for KLH began to skyrocket. To account for this, companies have been driven to establish aquaculture facilities dedicated to the sustainable growth of giant keyhole limpet colonies. This somewhat inflated hemocyanin market, with a resource supply bottlenecked by various EPA regulations, drove others to investigate the potential to use other hemocyanins in replacement of KLH [70].

3.3.2. Additional Hemocyanin Applications

Several groups and companies have successfully achieved the development of such an interchangeable product, such as hemocyanin from a Chilean gastropodon 'Conchepelas' (CCH). Similar and mirroring the application of KLH, CCH has shown to promote a humoral immune response, and is currently in preclinical vetting as an immunotherapeutic agent. [67,71,72]

Upon the investigation of using alternative hemocyanins, research groups began to find addition applications with alternative mechanisms of action. For example, Dolashka et. al. has characterized hemocyanins structure and anti-tumor potential from a variety of species over the past few decades, notably, the demonstration of anti-tumor activity of hemocyanin subunits from *Rapana venosa*, a large sea snail, against Guerin ascites tumor on a murine model [65]. Gesheva et. al. also brought hemocyanins to investigate anti-cancer activity on a murine model, using gastropodan hemocyanins, from the snails *Rapana thomasiana* and *Helix pomatia*, against colon carcinoma [66,73].

Teitz-Tennenbaum et. al. used KLH in an additional immunotherapeutic study; dendritic cell pulsed therapy, which showed to have considerable activity against melanoma on their murine model [74]. Arancibia et. al. found hemocyanin from the Limpet *Fissurella latimarginata* to possess potential anti-melanoma activity on a mouse model via humoral immune response, and even showed the immune response to be greater than dosage with KLH or CCH [59,67,75].

More work is now being done spanning into non-cancer disease models, such as Zanjani et. al., who showed that hemocyanin from the abalone can block entry of herpes simplex virus 1 (HSV-1) into cells, and later demonstrated efficacy with topical application of a hemocyanin-based nutraceutical [76]. Several groups have characterized various hemocyanins' anti-viral activity, hypothesizing that the carbohydrate chains on the exterior of the glycoprotein play a major role in binding to virus' via Van der Waals forces, resulting in anti-viral activity [31,71,77,78].

3.3.3. *In Vitro* Hemocyanin Anti-Cancer Activity

Accompanied with these novel applications and findings of hemocyanins alternative to traditional KLH use-case, many groups have performed thorough *in vitro* studies to understand mechanistic route of action on cell culture models.

To investigate immune-stimulatory potential, Zhong et. al. demonstrated in culture that hemocyanin from *'Concholepas, Fissurella latimarginata,* and *Megathura crenulata'* (keyhole limpet) stimulate a proinflammatory cytokines from macrophages, potentially responsible for the innate immune response by macrophage [75,79]. In a complementary study performed by Lui. et. al., hemocyanins from *Litopenaeus vannamei* were cultured with T cells, and T-cells subsequent added to cultures of HepG2 cells. Upon prior incubation with hemocyanin, they observed elevated T-cell anti-cancer activity, suggesting numerous immune anti-cancer mechanisms [73,79,80].

A significant amount of work has evaluated the effectiveness of hemocyanins from the (snail) genus *Rapana*, which are large predatory snails, against numerous cancer cells lines. Boyanova et. al. demonstrated efficacy of *Rapana venosa and Helix lucorum* hemocyanin against CAL-29 and T-24 bladder cancer lines, as well as comparative efficacy to cells dosed with KLH, doxorubicin and mitomycin over a period of 24 hrs [81]. Salama and Mona also demonstrated anti-breast cancer (MCF-7 line) as well as anti-hepatocellular carcinoma (HepG-2 line) activity, however, using hemocyanin isolated from crab species *Atergatis roseus* and *Eriphia verrucose* [82]. Guncheva et. al. further modified hemocyanin from the snail *Rapana thomasiana*, functionalizing with complexes of choline amino acid salts, which demonstrated potent anti-cancer activity against MCF-7 breast cancer cells, and with the amino acid modified surface, did not result in cell death when incubated with 3T3 (non-cancerous) cells, demonstrating the ability for selective anti-cancer activity with retained biocompatibility in the presence of normal, healthy cells [83]. A more comprehensive study performed by Antonova et. al. also included T-24 and CAL-29 bladder cancer

lines, in addition to an ovarian cancer line FraWu, acute monoctic leukemia line THP-1, prostate cancer line DU-145, glioma cancer line LN-18, and Burkitt's lymphoma Daudi line. They utilized *Helix lucorum* and *Helix aspersa* hemocyanin, and found broad anti-proliferative effects against the range of cancer cell lines utilized [84,85].

Riggs et. al. performed a similar study to Boyanova, with just KLH on breast cancer ZR75-1 and MCF-7 lines, pancreas cancer PANC-1 and MIA-PaCa cell lines, as well as the prostate cancer DU145 line. For each cell line used, KLH demonstrated a dose-dependent anti-cancer response [86]. They observed the same anti-cancer activity dosing Barret's esophageal cancer SEG-1 and BIC-1 cell lines, further demonstrating a dose-dependent relationship between cancer cell death and KLH dosage concentration [87]. The same group also provided that the *in vitro*, independent therapeutic activity of KLH was due to the induction of apoptosis in melanoma cell lines HTB68 and HTB72, following the dose-dependent anti-cancer response observed in other studies. They further characterized cytokine production from these cells, showing a clear disrupting in cytokine production, such as the suppression of IL-8, IL-6 and IL-2, and decrease in TNF-(alpha) expression. This was followed by further exploration into apoptotic stages observed throughout cell dosing, showing that ZR75-1 and MCF-7 breast cancer cells and PANC-1 pancreas cells exhibited high late stage apoptotic activity, another indicator that a broad spectrum of hemocyanins possess an innate ability to trigger intracellular apoptotic pathways in cancer cells, leading to cell death [88].

This hypothesis was further cemented by Zheng et. al., who published a detailed study describing their methods of purifying hemocyanin from shrimp *litopenaeus vannamei* and characterized numerous HeLa cell cellular events triggered upon dosage, that cascaded to the eventual induction of apoptosis. They hypothesized that apoptosis was induced by an intrinsic mitochondrial metabolic pathway, that began with the overproduction of reactive oxygen species (ROS), leading to a shift in mitochondrial membrane potential, which triggered subsequent cleavage of caspase-9/3 – indicative of end-stage apoptosis [89]. After

rigorous biochemical analysis in this study that showed multiple indicators of a mitochondrial induced apoptotic cell death pathway (alterations in genetic expression, secretion of various factors, cleavage of caspases, etc.), they pursued treating Sarcoma-180 tumor-bearing mice, and showed promising effectiveness following a similarly described pathway as their *in vitro* work [90].

3.3.4. Hemocyanin Industry Bottleneck and Alternative

Such promising applications of a range of hemocyanins on the brink of discovery beg question as to how other hemocyanin's biomedical potential can be realized and why there aren't more commercially available hemocyanin-based therapies. A reasonable explanation may not be due to the demand, but the readily available supply of hemocyanin to fuel an emerging industry. Harvesting of the giant keyhole limpet was an industry that grew over decades, forming the fishing, harvest and eventual aquaculture of the keyhole limpet into a commonly practiced processed [91]. Other hemocyanins that have displayed comparable and alternative therapeutic activity, such as *Rapana venosa*, *Helix lucorum* and *Litopenaeus vannamei* in the studies mentioned, do not have a collection process based on an existing fishery or aquaculture facility. Therefore, implementation of feasible large-scale commercial therapeutics and other medical hemocyanin-based products would require the establishment of entire fishery processes, practices, ecological impact studies and guidelines. Likely, these would be incredibly expensive, time consuming, and produce relatively low yield compared to that needed to combat the recognized potential disease applications.

The lobster industry stands to offer such a suitable alternative, as the lobster industry is a large scale, sustainable fishery. Lobster hemolymph, and the hemocyanin suspended within the lymph, is discarded a waste byproduct in lobster processing plants at a rate of estimated 3-5 million pounds of hemolymph per year. With hemocyanin averaging to account for roughly 95% of the total protein content in lymph, lobster

hemocyanin is estimated to be discarded at a scale of 1 million pounds per year. With recent Maine lobster hauls reaching an all-time high, the evaluation of lobster hemocyanin as a suitable therapeutic for the previously described applications is of significant value – as the current supply of wasted hemocyanin has the potential to fit the bill for supplying a growing hemocyanin industry.

3.4. Optical Metabolic Investigation of Lobster Hemocyanin Anti-Cancer Effects

3.4.1. Study Overview

The goal of this study was to investigate the anti-cancer potential of lobster hemocyanin against lung cancer adenocarcinoma A549 cell line. Our hypothesis follows that of the previously described work, in which hemocyanin possesses anti-cancer activity due to induction of apoptosis in cancer cells. We processed and purified hemocyanin in-house following a protocol used by several previous hemocyanin studies, followed previous methods to use absorbance to determine hemocyanin concentration, and subsequently dosed cells at varying ranges of concentration [57,92]. Measurements for anti-cancer activity began with a standard cell viability MTT colorimetric assay from which we were able to calculate an IC50, then used the corresponding IC50 concentration to dose cells for two-photon ORR experiments, as well as confocal imaging of cells labeled with a CellEvent Caspase-3/7 detection kit to visualize end-stage apoptosis.

3.4.2. Methods

3.4.2.1. Collection

Collection was performed by industry collaborators at Lobster Unlimited LLC. Hemolymph was drawn from the pericardium of the lobster and transferred to a laboratory homogenizer. The raw lymph was homogenized to remove cellular components, and a supernatant consisting of ruptured cells and their respective components was formed. The supernatant was removed and resulting solution was run through a 40um bacterial filter. The resulting solution was stored at -20C (frozen) and thawed as needed.

3.4.2.2. Determination of Concentration

Digital refractometry and absorbance spectroscopy were initially sought to be employed to determine concentration of hemocyanin within native solution. Hemocyanins exhibit two distinct peaks; a peak at 280nm corresponding to tyrosine and tryptophan, and a peak at 350nm corresponding to tyrosine and tryptophan in close proximity to a Cu-Oxygen bound 'active' site (when the protein is oxygenated) [93,94]. As the peak at 350 has been experimentally demonstrated to vary depending on both hemocyanin concentration and oxygenation, absorbance of the 280 peak, which only varies with concentration, was to be used to determine hemocyanin concentration [58,95].

However, in previous work performed by Bolton et. al., absorbance spectroscopy was used in parallel to digital refractometry to identify an optimal method for determining hemocyanin concentration within the lymph, which revealed a direct correlation between absorbance, Brix value and hemocyanin concentration. Therefore, either method was determined viable for measuring concentration. Here, the degree on the Brix scale from the digital refractometer measurement was primarily used, where 1-degree brix correlated to 1g protein per 100g aqueous suspension. As the suspension is lymph, which is primarily

salt water, the 100g was converted to 100mL by using the molecular weight of water [95]. Therefore, 1-degree brix correlated to:

Equation 3.1. Brix Scale conversion to concentration.

$$Brix = \frac{1g}{100mL}$$

Measurement of the native hemocyanin in the refractometer revealed a Brix value of roughly 15, indicating a 150mg/mL solution of native hemocyanin. This solution was used as the stock, further diluted in media for cell dosing experiments.

3.4.2.3. MTT Assay

96-well plates were seeded with A549 cells at a density of 36,000 cells/mL with 200uL of cell suspensions, which was experimentally determined to be the optimal seeding density for assays. After seeding, cells were allowed to attach for 24 hrs, and subsequently dosed with varying concentrations of hemocyanin dissolved in media with 100uL dosing agent, for a period of 72hrs. After 72hrs, the dosing agent was removed and a solution of 400 µM MTT was added to each well. MTT solution incubated in wells for a period of 4 hours, and upon successful conversion of MTT into formazan crystals (visually confirmed in a brightfield microscope for each experiment), the MTT solution was removed and replaced with DMSO. This step dissolved the crystals, turning the aqueous layer increasingly more purple corresponding to the amount of formazan crystals, and was left in the incubator to dissolve the crystals for 1hr. After this, the

plate was analyzed by a BioRad plate reader, measuring absorbance at 560nm (purple signal) and 670nm (background). Each experiment was performed in triplicate.

3.4.2.4. ORR

Cells were seeded in 35mm circular dishes at a concentration of roughly 36,000 cells/mL and allowed to attach for 24 hrs. Subsequently, media was removed and 25mg/mL hemocyanin solution (suspended in media) was added to cells, and incubated for a period of 24hrs. Prior to this, cell dishes were placed under the two-photon microscope setup. The custom, home-built two-photon microscope setup used consisted of a mode-locked Titanium Sapphire laser excitation source (Chameleon; Coherent, Santa Clara, California) directed into a laser scanning unit (FluoVIEW 300; Olympus, Center Valley, Pennsylvania) which was mounted onto an upright microscope stand (BX50WI; Olympus, Center Valley, Pennsylvania). Laser power was modulated by an Electro-Optic Modulator (ConOptics, Danbury, Connecticut), operated in a power range of 1-500mW at the focal plane using a 40x 0.8NA water immersion objective, and excitation wavelengths were consistent at 760nm and 890nm for NADH and FAD excitation, respectively. Both NADH and FAD fluorescence were collected using a Photosensor Module (H7422 Series GaAsP Photosensor Module; Hamamatsu, Hamamatsu City, Japan) through 450 +/-35nm and 582 +/-32nm filters (Semrock, Rochester, NY), respectively. Five locations per cell dish were imaged, consisting of an average of 10 cells/image.

3.4.2.5. Apoptosis: Caspase-3/7 Activity

For investigating late stage apoptotic activity, cell seeding and dosing protocol was performed identical to the ORR experiments. The caspase-3/7 kit was selected for the specific binding to caspases secreted

during end-stage apoptosis, allowing for clear visualization of apoptotic cells on a single-cell basis. Upon dosing for the appropriate amount of time, in this case 24hrs, the aqueous layer was removed, and replaced with 2mL CellEvent Caspase-3/7 Green Detection Reagent (ThermoFisher Scientific) diluted to 10uM in complete medium. The Caspase-3/7 solution was allowed to incubate with the 45 minutes, after which was exchanged with complete medium. Cells were visualized under a Leica DMR upright fluorescence microscope, using a filter cube consisting of a 490/20nm bandpass excitation filter, allowing for visualization of fluorescence emission through a 525/20nm emission filter.

3.4.3. Results

3.4.3.1. MTT Assay Results

A549 cells in 96-well plates were dosed with varying concentrations of hemocyanin, calculated by the refractometer as described above, and diluted in media to concentrations of 50, 45, 40, 35, 30, 25 and 20ug/mL – mimicking dosing ranges of previously performed *in vitro* hemocyanin anti-cancer experiments [63,81,96]

Absorption measurements at 670nm were subtracted from values in the corresponding well at 560nm to subtract background signal, as well as normalized to a control (dosage with media) to scale absorbance to viability from a scale of 0-100%, where 0% indicates no viable cells and 100% indicates complete cell survival (identical to the value of the control). Percent viability values were plotted against concentration of hemocyanin dosage, and fitted with appropriate error bars, shown in Figure 3.1, below.

Figure 3.1 MTT Assay results with varying amounts of native lobster hemocyanin.

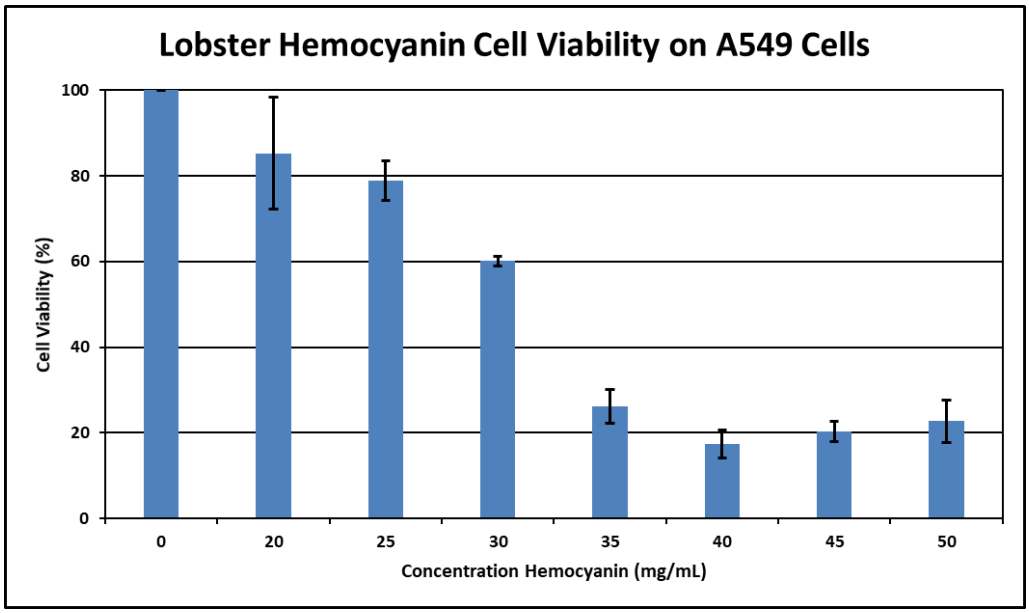

MTT assay results demonstrated a clear reduction in cell viability as hemocyanin dosage concentration was increased, with the lowest amount of cell viability observed at a dosage concentration of 40ug/mL. A slight increase in calculated 'cell viability' was observed at concentrations higher than 40ug/mL, which was attributed to non-reacted hemocyanin in wells, as wells with high hemocyanin concentration exhibited a visible opalescent blue colorimetric profile, likely overlapping with absorbance reading intended for the purple solubilized formazan. Future experiments should include a control to account for this additional optical signature, however, for the purposes of demonstrating a reduction in cell viability, the experimental data shown above proved to be adequate in exploring the range of effective anti-cancer native hemocyanin concentrations.

From this data, the inhibitory concentration (IC_{50}), or concentration at which 50% of the cell population was viable, was approximated to be roughly 32ug/mL [97]. This concentration of hemocyanin solution used for dosing dishes of A549 cells in further ORR and apoptosis-validating experiments

3.4.3.2. ORR Analysis

ORR image sets consisted of two channels; NADH and FAD raw recorded fluorescence. To adequately quantitatively process images and data, the use of an image processing program was necessary. To do so, image sets were imported into an image processing program called CellProfiler. CellProfiler is a freely available open source cell image analysis software, possessing a particular strength performing numerous single-cell analyses with large batches of data. To do so, one can create a 'pipeline' (more commonly in other languages referred to as a routine) to string together step-by-step image processing algorithms and math to allow for simple, automated image data processing.

The CellProfiler pipeline created for ORR experiment image analysis is as follows:

Table 3.1 ORR CellProfiler Pipeline

1.	Load Images Images are saved in specific directories, which are initially called upon by the program to search for a collection of images. Using a simple naming protocols to designate certain images, such as including 'NADH' for NADH images and 'FAD' for FAD images gives the program a reference to selectivity upload and group images based on similar attributes. In this program we use these notations to isolate NADH and FAD into groups for further image processing.

Table 3.1 Continued

2. Rescale Intensity

During image acquisition, images in particular locations, in any channel, are taken with varying source excitation power. This is due to the balance primarily between three parameters; a) maximizing the amount of excitation events and thus, fluorescence collection from the sample and fill the dynamic range of the detectors, b) avoid detector, and c) avoid sample damage due to harmfully high excitation powers, a common occurrence in sensitive, highly absorbing samples. To account for a change in power delivered to each sample, images must be normalized to allow for accurate analysis. In this step image pixel values are simply stretched, or normalized, to use the full intensity range.

3. Threshold

A thresholding method is incorporated into almost every image analysis pipeline, allowing for isolation of the signal of regions of interest, and/or removing of unwanted objects, artifacts or background. In this analysis, a global minimum cross entropy method is employed combined with a lower threshold boundary value of 0.06 (on a 0-1 scale) – which visually inspected and shown to perform the most adequate removal background signal around cell cytoplasm.

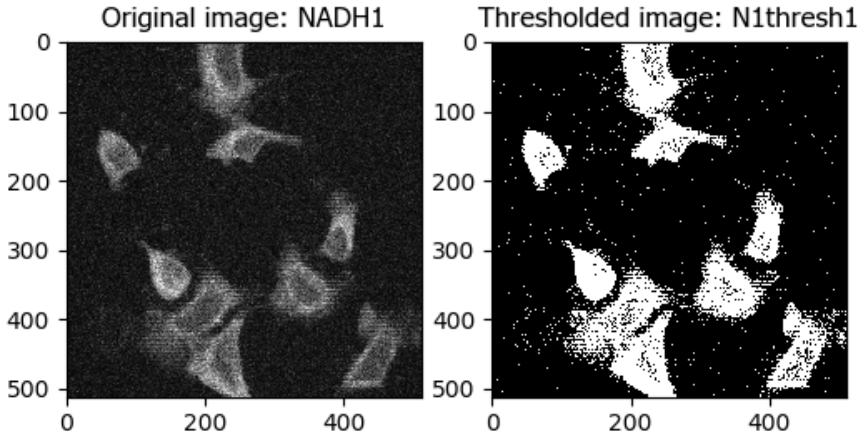

Table 3.1 Continued

4. Smooth

To further exaggerate the thresholding of the background, a smoothing step is incorporated. A median filter is used in the smoothing method that calculates artifact diameter automatically. Overall, this will essentially tighten the threshold by one step size further into the objects still identifiable, to ensure all background and artifacts are removed.

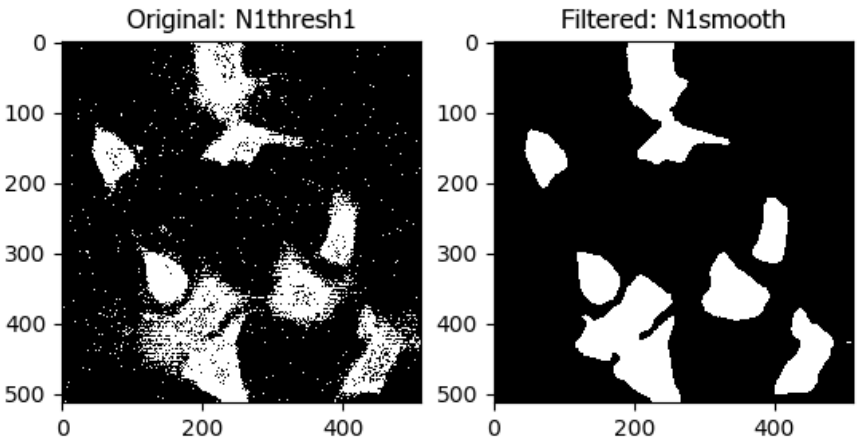

Table 3.1 Continued

5. Invert for Printing

To carry out further processing, the rescaled and thresholded image, still in grayscale format, required conversion to color image, performed by the invert for printing function. Additionally, this function inverts the image from the 0-1 scale to 1-0, therefore bright sections become dark and vice versa. This produces a background image mask for utilization in the next step.

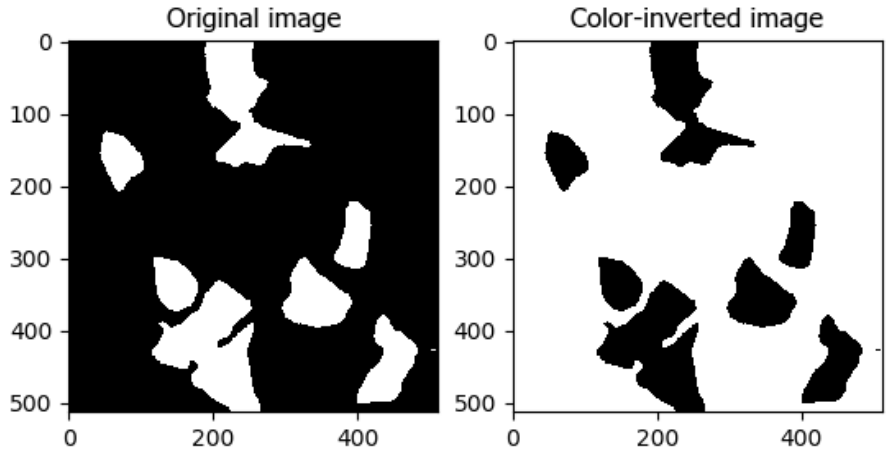

6. Mask Image

Using the inverted image in the prior step, rescaled NADH images are overlaid with a mask produced in Step 4, effectively removing the background signal from the image.

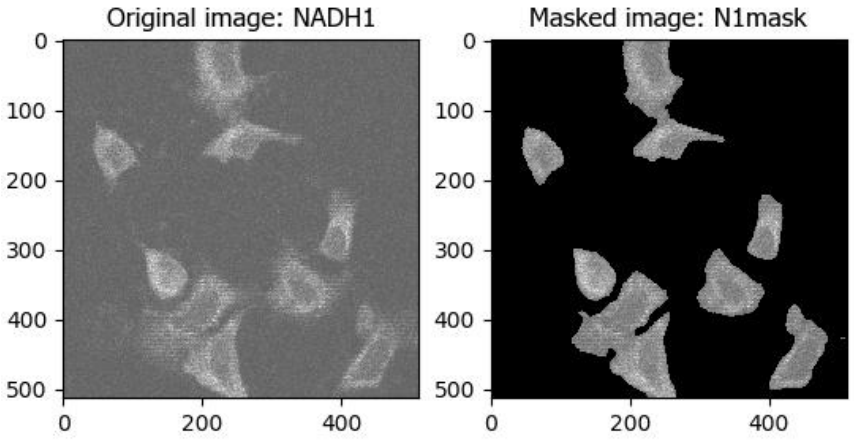

Table 3.1 Continued

7. Identify Primary Objects

For ORR image processing, it is necessary to remove nuclei autofluorescence signal from analysis, as nuclei signal in both channels has not been shown to correlate to NADH or FAD fluorescence in the cytoplasm. In this step, masked images' (from Step 5) nuclei were isolated based on boundary edges, circulatory and a distinct change in pixel intensity across boundary, which were adjacent to the much brighter fluorescence signal from the cytoplasm. Identification of nuclei classified each as 'Primary Objects'.

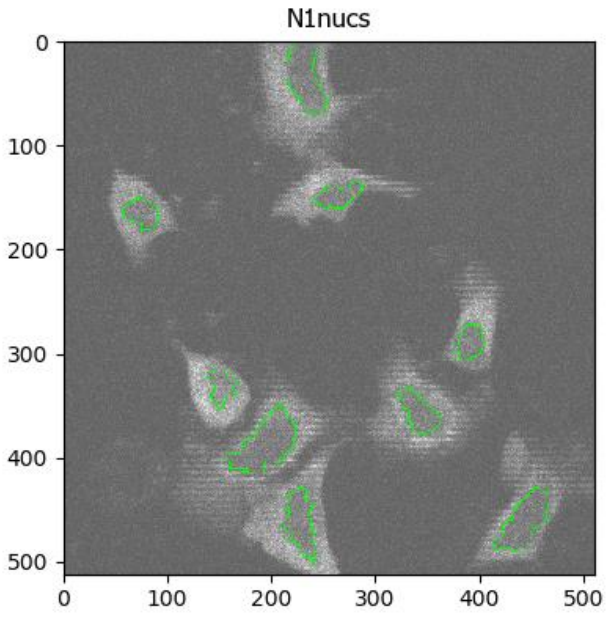

Table 3.1 Continued

8. Identify Secondary Objects

Numerous iterations of image analysis pipelines proved identification as nuclei as primary objects, for subsequent identification of cytoplasm as secondary objects around the parent primary object, to be the most effective means of image processing. This step uses a propagation algorithm for objects originating from the parent primary object, again employing a global minimum cross entropy thresholding method, with a regularization factor of 0.05. It is important to note that these methods should be altered and tailored to particular image sets, as one method may not be suitable for images of different characteristics. This step identifies cytoplasm boundaries (exterior boundaries of the cell), and exports regions as masses inclusive of everything inside of the exterior boundaries.

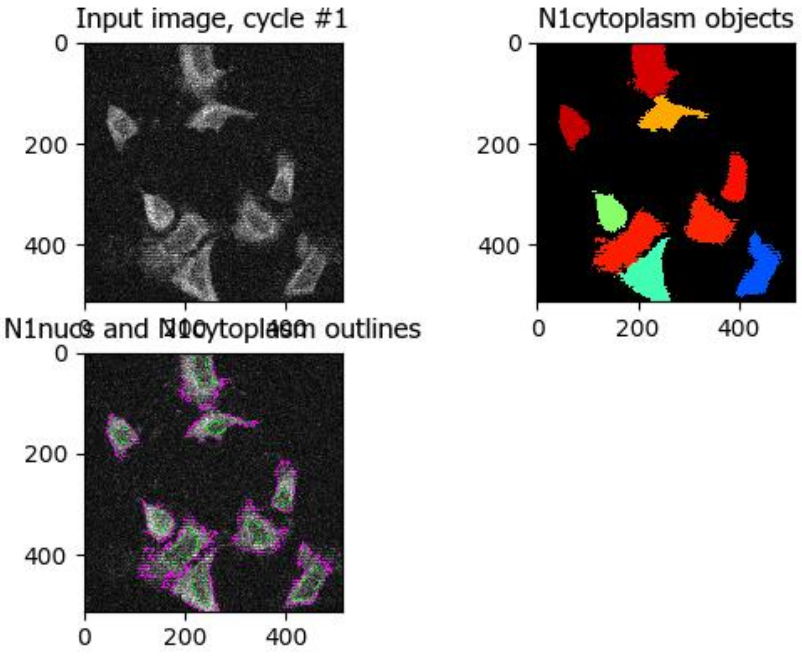

Table 3.1 Continued

9. Mask Objects

With the exterior boundaries of the cytoplasm defined in Step 7, and respective cell nuclei boundaries defined in Step 6, a mask object function can be used to mask cytoplasm images with nuclei images – removing the nuclei boundaries from the regions of interest, isolating just cytoplasm and classifying these areas as individual objects.

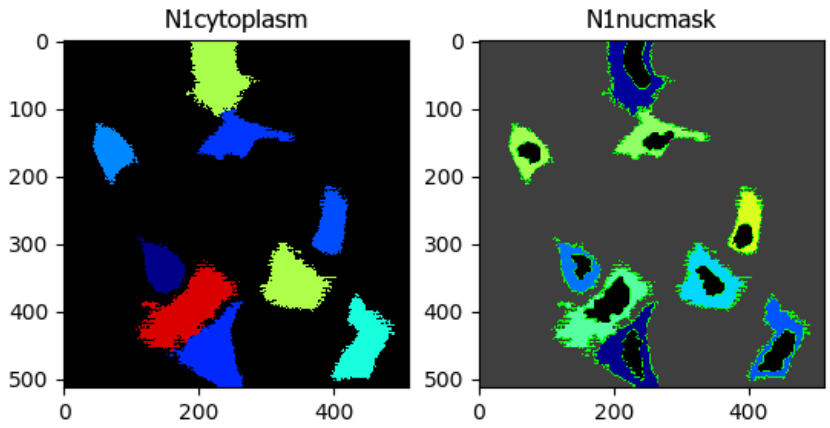

10. Measure Object Intensity

With the cytoplasm regions isolated as individual objects, and each image's intensity appropriately rescaled in Step 2, the measure object intensity function will measure rescaled cytoplasm intensity on a single-cell basis, exporting normalized raw integrated intensity values for each object, or cell. This information is exported to an organized .csv file for further processing in excel.

Table 3.1 Continued

11. Export to Spreadsheet Information calculated in Step 9 is exported to an organized .csv file for further processing in excel. Upon exporting the data to a spreadsheet, integrated pixel intensities for individual objects (cells) are compiled. Values are first rescaled to account for varying power taken per image, using the equation (below), which normalizes intensity values based on a ratio of laser excitation power used during that particular image, to the highest laser excitation power used of any image collected and considered in the data set.

Equation 3.2 Calculation of normalized intensity for NADH and FAD channel images

$$Normalized\ Intensity = Integrated\ Intensity/(\frac{Image\ Power}{(Total\ Image\ Set\ Power)^2})$$

This normalization is performed for arrays of both NADH and FAD cell cytoplasm intensities values and designated as 'NADH normalized' and 'FAD normalized'. Next, the ratio of NADH normalized to FAD normalized intensity is taken on an object-by-object basis (simply the quotient of NADH normalized / FAD normalized). Finally, normalized ORR is calculated by dividing NADH normalized by the NADH normalized / FAD normalized quotient, shown in **Equation 3.3** below.

Equation 3.3 Normalized ORR

$$Normalized\ ORR = \frac{NADH}{(NADH + FAD)}$$

Normalized ORR values are culminated and reported as an average single-cell ORR across the entire set of images taken for each acquisition parameter and time point. An average of 50 individual cells were analyzed for each image set.

Figure 3.2 ORR data displaying changes in RR at 4 and 24hrs post-dosage. Control (media) is shown in grey and native lobster hemocyanin in blue.

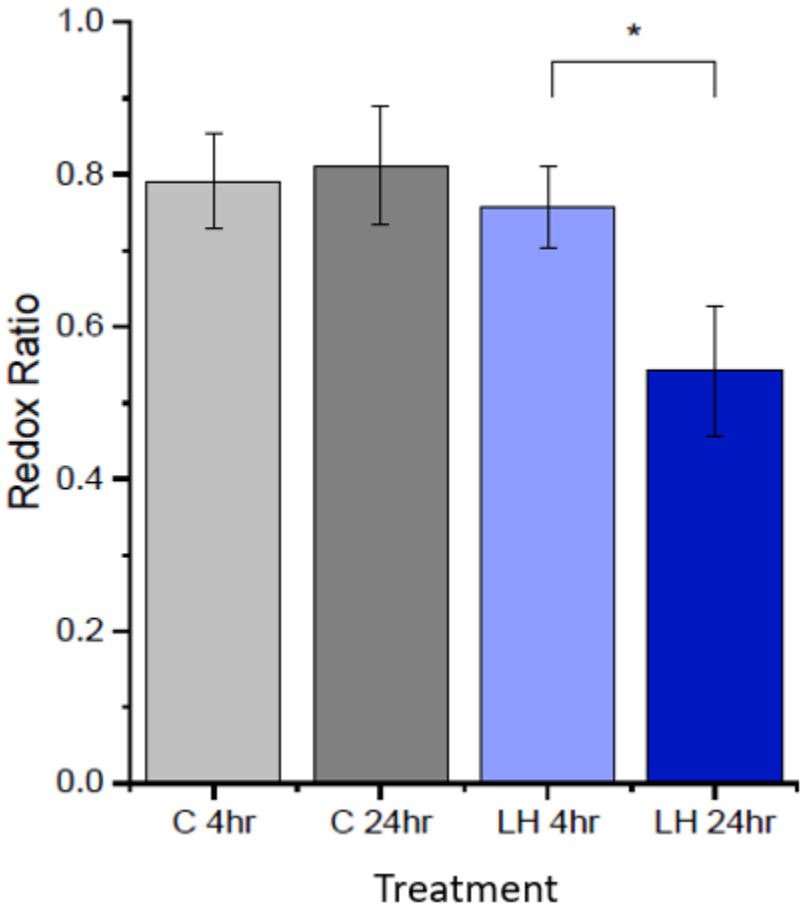

3.4.3.3. Apoptosis: Caspase-3/7 Results

The CellEvent Caspase-3/7 Green Detection Reagent kit was used to identify signatures of apoptosis. A Leica DMR was used to visualize green fluorescent emission, as well as viewing in a typical brightfield manner. Therefore, two channels of images were collected; brightfield images of the entire viewing plane, and green fluorescent images of apoptotic cells. Overlaying the two channels allows for comparison of number of apoptotic cells to total cells in the viewing plane, and thus a ratio of percent of visible cells undergoing apoptosis. In this study, we compared a control 'dosed' with complete media, to a dish of cells dosed with the IC50 concentration (from MTT assay results) of hemocyanin.

Fluorescence imaging for presence of caspase 3/7 with A549 cells dosed with 32ug/mL native hemocyanin revealed no visible fluorescence in any image set, indicating that the primary cell-death mechanism of action of the native hemocyanin solution was not apoptosis, therefore some means of inducing necrosis.

3.4.4. Native Hemocyanin Discussion

As previously mentioned, apoptosis is the primary mechanism of action observed across a range of hemocyanin types in their anti-cancer application for *in vitro* experiments. Considering likely causes of cell death other than apoptosis, it was possible that the salinity of the native hemocyanin solution was an important factor previously overlooked. It is well known in lobster anatomy and physiology that the salinity of the lymph matches that of the surrounding ocean water, therefore, solutions extracted from lobsters can range between 2-6% salinity. With this known, observation of cell morphology upon native lobster hemocyanin dosage did demonstrate a clear shriveling and shrinking effect when dosed, as if cell osmotic balance had been disrupted, drawing aqueous content out of the cell, causing a shriveling morphology.

Figure 3.3 NADH image demonstrating blatant cell shriveling and shrinkage. Hypothesized to be due to high salinity of native hemocyanin solution causing a significant osmotic imbalance.

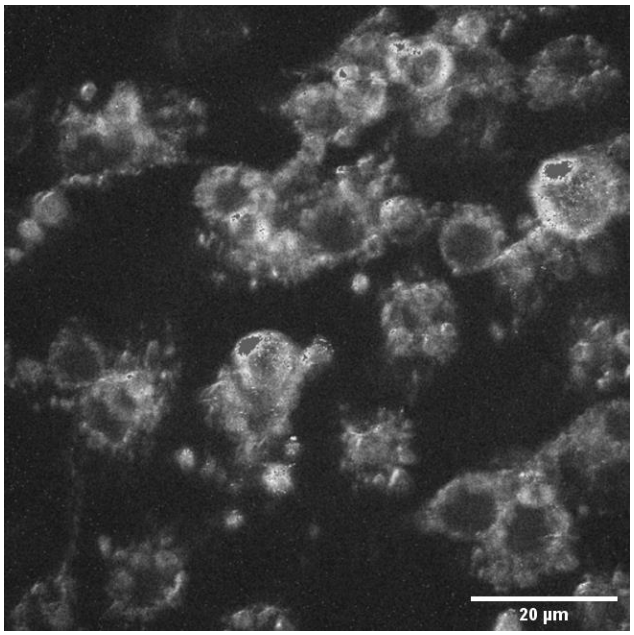

With this hypothesis for the current primary means of cell death from native hemocyanin, and cross-refencing our method for hemocyanin extraction and purification, it became evident that isolation of the protein by further purification methods was necessary, to ensure cell death was solely induced by the hemocyanin protein itself. Therefore, a method for purification of lobster hemocyanin previously performed by Hodgkin et. al. was adopted, where the primary means of isolation utilizes ultracentrifugation [98,99].

3.4.5. Anti-Cancer Effects of Ultracentrifuged Lobster Hemocyanin

3.4.5.1. Ultracentrifugation

As hemocyanin is a highly water-soluble carrier protein, a significant amount of force is required to physically remove the protein from solution, therefore, ultracentrifugation steps have been employed by groups purifying a wide range of hemocyanin types. To isolate hemocyanin from the *Homarus Americanus*, a method previously used to isolate the same protein for anti-viral applications by Hodgkin et. al. was utilized.

Thawed (chilled) hemolymph solutions were centrifuged at 3000g at room temperature for 30 minutes. Upon formation of a pellet, which consisted primarily of suspended tissue and cellular debris, the supernatant was removed, transferred to another centrifuge tube, and centrifuged again with identical parameters for another 10 minutes. The following supernatant was transferred to Nalgene ultracentrifuge-grade tubes, and subsequently ultracentrifuged at 40,000rpm at 5°C for 6.5 hours. The supernatant of the resulting solution was removed, pellet weighed, and media was added to resuspend the pellet (containing >95% hemocyanin). The resulting solution was stored in a refrigerator overnight, allowing the hemocyanin to dissolve into solution, and once evenly dispersed in solution stored in a -20°C freezer until further use.

3.4.5.2. Concentration

Digital refractometry was used to investigate the concentration of resuspended hemocyanin. Refractometer readings averaged 5.1 – indicating a concentration of 51 mg/mL hemocyanin. This solution was treated as the stock concentration and diluted for subsequent MTT assays.

3.4.5.3. Analysis of Purification by HPLC

High performance liquid chromatography was performed on a Hitachi-Hitech Chromaster on a standard column for protein purification by industry collaborator Lampire Biological Laboratories, to evaluate extent of hemocyanin purification and hemocyanin isomer distribution.

Figure 3.4 HPLC of Ultracentrifuged Lobster Hemocyanin. Performed by Lampire Biological Laboratories.

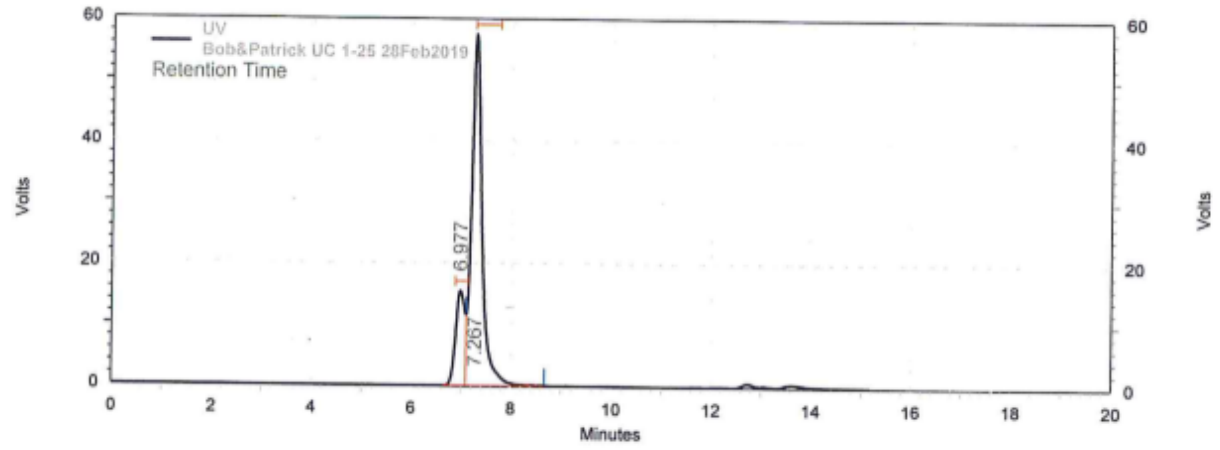

UV Results

Pk #	Name	Retention Time	Area	Area %
1	peak-1	6.977	775478	18.59
2	Dimer	7.267	3396131	81.41
Totals			4171609	100.00

Two key elution peaks emerged, a predominant peak with a retention time of 7.267 (amassing 81.41% of the area) and a smaller peak on its shoulder at 6.977 minutes (18.59% area). A calibration curve generated by internal standards for varying protein sizes was referenced to approximate molecular weight (MW) of protein at the predominant peak, shown in **Equation 3.4** below.

Equation 3.4 Calibration equation generated by Lampire, HPLC protein size

$$Log(MW) = -0.53(Elution\ Time) + 9.6831$$

Plugging in 7.267 for the elution time, the Log of the molecular weight was calculated to be 5.83, which relates to a molecular weight of roughly 670,000 Da. This rough approximation is supported by literature, as hemocyanin subunits can range from 70,000-120,000 Da, and Bolton et. al. demonstrated that the most common form of lobster hemocyanin isomer is a hexamer – 6 subunits bound together [58,100,101]. It is likely that the shoulder can be attributed to a slightly smaller isoform. Overall, the HPLC data conformed to an anticipated result for hemocyanin isomer and demonstrated fair purity level of the molecule.

3.4.5.4. Ultracentrifuged Hemocyanin MTT Assay

An MTT assay was performed following the identical protocol to the native hemocyanin, however, concentration of hemocyanin was shifted to range between 0-50mg/mL, to cover a broad range of concentrations.

Figure 3.5 MTT Assay results with varying amounts of Ultracentrifuged Hemocyanin.

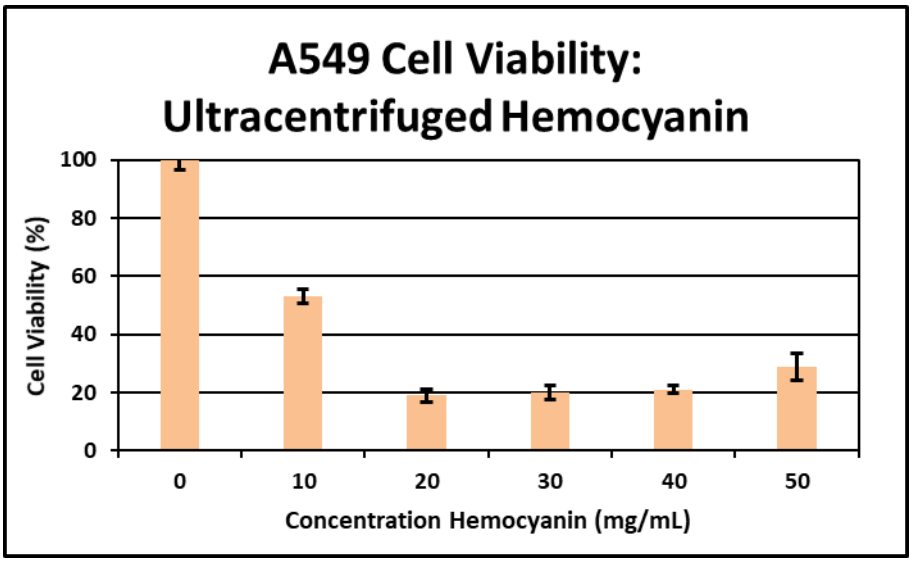

The MTT assay clearly illustrated a reduction in cell viability as concentration was increased. It is likely that due to the higher concentrations than that of the native hemocyanin experiments, the reduction of cell viability was thus increased (when comparing the two experiments). This resulted in roughly 20% cell viability upon dosage with 20mg/mL hemocyanin, and the IC_{50} was approximated at 10mg/mL. Therefore, 10mg/mL was the working concentration used for further cell dosing experiments.

To immediately investigate mechanism of action (apoptosis or necrosis), caspase-3/7 experiments were performed immediately following the analysis of the MTT results shown above in **Figure 3.5.**

3.4.5.5. Ultracentrifuged Hemocyanin Apoptosis Results

Cells were labeled with the Caspase-3/7 kit following the same procedure in the native hemocyanin experiment. Labeled cells were imaged as described in the methods section: under a Leica DMR upright

fluorescence microscope, using a filter cube consisting of a 490/20nm bandpass excitation filter, allowing for visualization of fluorescence emission through a 525/20nm emission filter. An additional set of images was taken in the brightfield channel to allow for counting of all cells in the viewing area.

Figure 3.6 Sample merged brightfield and caspase-3/7 fluorescence signal channels - Ultracentrifuged hemocyanin-dosed A549 cell dish.

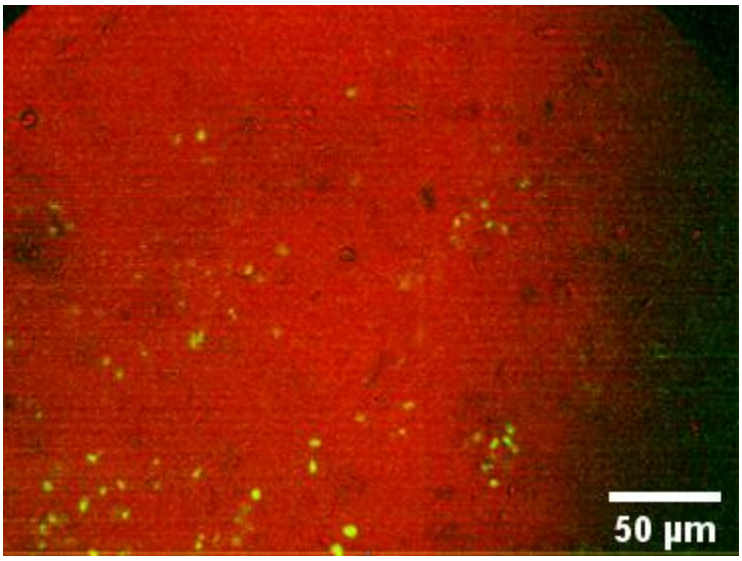

Images were acquired in both channels and merged in ImageJ for analysis, such as in the image presented in **Figure 3.6**. Cells visible in both channels were summed and ratio of apoptotic cells to overall cells was calculated, averaging roughly 70 apoptotic cells/135 cells total in view. Therefore, the % apoptotic cells was roughly calculated to be an average of 52%.

Further work should aim to more rigorously quantify cell apoptotic response upon dosage with a range of hemocyanin concentrations, and probe a complimentary indicator of apoptotic response to more deeply understand the mechanism.

3.4.6. Discussion

This inconclusive work demonstrates the potential for an ultracentrifuge-purified lobster hemocyanin protein to have anti-cancer effects. This claim was supported by the MTT assay displaying the A549 lung adenocarcinoma cell line IC_{50} (upon dosage with hemocyanin) to be 10mg/mL. Dosage of the same cell line in dishes with 10mg/mL hemocyanin solutions resulted in clear fluorescence from cleaved caspase-3/7 in solution, indicating the presence of apoptosis upon dosage. Future work should aim to further characterize the extent of hemocyanin purification, potentially establish more robust means of determining hemocyanin isomer distribution, and work to understand the mechanism of lobster hemocyanin inducing an apoptotic mechanism in cancer cells. Overall, this facet of applying the Tilbury Lab two-photon system demonstrated the clear ability to images changes in cellular metabolism via ORR, and established robust image processing algorithms for the analysis of two-photon ORR imaging data.

Chapter 4

APPLICATIONS IMAGING THE CELLULAR-MATERIAL INTERFACE

4.1. Introduction

Over the past decade, interest in polysaccharide-based biomaterials for biomedical applications has increased explosively. Common polysaccharide polymers used in biomedicine today include alginates, starches, chitosan, and cellulose derivatives; all abundant, naturally-sourced materials. These materials are highly attractive candidates for biomedical applications as they are readily modifiable using surface chemistry functionalization for modulation of mechanical, optical and biocompatibility properties [1,2]. Realization of these desirable and adaptable properties has led to the broad utilization in applications such as drug delivery, wound healing, and tissue engineering [1,3,4].

4.2. Background

Tissue engineering applications, specifically, involves the use of these materials as biomedical implants, three-dimensional cell culture systems, wound healing and tissue regeneration scaffolds. Preparation of such materials requires an intricate balance of desirable mechanical and biocompatibility properties [5]. For example, an implantable polysaccharide-based medical device for bone regeneration requires tensile properties similar to that of the native bone, accompanied with a bone-like microporous structure for cellular migration and networking formation, and possessing the necessary biocompatible surface properties for adequate cellular adhesion that allow cells to subsequent secrete the necessary chemical factors to induce further proliferation [6–8]. Overall, the high tunability of polysaccharides make them viable materials for such applications, and for regenerative tissue applications must be specifically tailored to

allow for growth of viable cells; adhesion, proliferation, ingrowth and maturation into integrated tissue networks [9]. To vet a material's ability to facilitate or induce such biological processes, it is necessary to quantify such attributes of the material's interaction with biology on the cellular level.

4.2.1. Current Methods - Strengths and Downfalls

Candidate biomaterials need to demonstrate cellular proliferation and function to characterize and establish the materials' in-vitro biocompatibility prior to most costly in-vivo assays [2,10]. Cellular proliferation is an early biocompatibility indicator and is commonly characterized using widefield and confocal microscopy approaches, plate reader assays, flow cytometry and atomic force microscopy [11–13]. Microscopy approaches are advantageous over both plate reader assays and flow cytometry as they offer spatial information; however widefield and confocal microscopy have limited depth penetration particularly troublesome in highly scattering biomaterials such as polysaccharides [12,14–17]. Flow cytometry approaches are quick and commonly used to differentiate cellular populations based on the presence of surface receptors; however cells must be removed from the candidate biomaterial either through mechanical scrapping or chemical digestion potentially altering the cells [18–21]. AFM provides high resolution images of surface topological features suitable for studying fibril orientation and geometry as well as the ability to derive mechanical properties such as Young's Modulus and viscoelasticity [22,23]. Unfortunately, AFM suffers from poor depth penetration therefore 3D biological interactions within complex candidate biomaterials such as polysaccharides are hindered [11,24].

4.2.2. Second Harmonic Generation (SHG) Imaging

Second Harmonic Generation, coupled with two-photon fluorescence imaging, may be a viable means to simultaneously image cellular features and morphology of the candidate polysaccharide biomaterial. SHG is a coherent, label-free process that occurs when 2-photons of identical energy interact with a non-centrosymmetric structure resulting in a single photon at half the wavelength [25,26]. Common biological proteins that are SHG active include: fibrillar collagens, myosin, and cellulose. SHG imaging has been utilized as a tool to study fine features of nanocellulose fibrils, as well as biological interactions with nanocellulose [27,28].

Previous work exploring SHG signal in cellulose matrices further investigated the variables dictating forward/backward signal ratio; where fiber orientation and sample depth parameters highly affected the ratio [27,29–31]. The high dependence of SHG signal on fiber orientation and polarization of the excitation beam was demonstrated in similar work performed by Zimmerley et. al. where dry and hydrated CNF spectral characteristics were probed via Raman spectroscopy and SHG imaging [32]. Recent work has employed this property of CNF to image cellular behavior and growth onto CNF-based scaffolds, shown to produce ideal images with high contrast between biological endogenous fluorescence, tagged extracellular matrices and cellulose structures in images of neuronal growth onto nanocellulose scaffolds [33]. Overall, SHG and 2-photon fluorescence microscopy is a viable tool for imaging biological interactions. Unfortunately, CNF materials are non-homogenous and possess highly variable optical properties, prohibiting use of existing techniques to study desired biomaterial characteristics such as cell proliferation and ingrowth into the scaffold.

4.3. Study Overview

Here, we present a method utilizing two-photon microscopy and SHG imaging to image three-dimensional cellular proliferation on cellulose nanofibrillar-based scaffolds. We first characterized the fluorescence of the CNF using Diffuse Reflectance Spectroscopy (DRS) and Steady State Luminescence Spectroscopy (SSLS), which illustrated its broad emission, leading us to explore photobleaching to optimize our contrast to noise ratio (CNR) for robust cellular imaging using common fluorophore labels. We characterized the photobleached CNF material and determined there was no structural damage inflicted via characterization of the CNF using SHG generation, however the autofluorescence returned within 24 hours therefore making it a non-viable means to enhance our CNR. Using knowledge of the CNF autofluorescence spectral characteristics, we selected an optimal cellular fluorophore and developed an imaging method using two-photon fluorescence spectroscopy and SHG to visualize cellular and material content. Specifically, we used Cell Tracker Orange (CTO) to image cells interacting with the CNF films. Cell nuclei were identified using a new semi-automated imaging pipeline for an assessment of cellular proliferation.

4.4. Methods

4.4.1. CNF Film Preparation

Roughly 3mm thick CNF films were prepared from a bulk source of 3 wt% CNF slurry (UMaine Nanomaterial Pilot Plant, Process Development Center) by confining 25mL increments of slurry between two macro-porous ceramic interfaces and transferring into an 80°C oven for 24 hours, producing bulk dried films. Thin 20 mm diameter circular films were then created from these bulk materials using a circular biopsy punch, and were subsequently sterilized using a dry autoclave at 121^{o}C for 60 minutes. For

cell culture experiments, films were seeded with MC 3T3 E1 mouse pre-osteoblasts at a density of 100,000 cells/mL, suspended in 2mL of complete media. Complete media consisted of MEM Alpha 1X with 10% FBS and 1% penicillin/streptomycin.

4.4.2. Characterization of CNF Autofluorescence

4.4.2.1. Diffuse Reflectance Spectroscopy (DRS)

CNF DRS spectra were collected at 298 K, using a Mikropack DH-2000 deuterium and halogen light source coupled with an Ocean Optics USB4000 detector. Scattered light was collected with a fiber optic cable. Spectra were referenced with MgSO4. Data was processed using SpectraSuite 1.4.2_09, and further analyzed using Origin.

4.4.2.2. Steady-State Luminescence Spectroscopy (SSLS)

CNF SSLS scans were collected at 298 K, using a Model Quantamaster-1046 photoluminescence spectrophotometer from Photon Technology International using a 75 W xenon arc lamp combined with two excitation monochromators and one emission monochromator. A photomultiplier tube at 800 V was used as the emission detector. The solid samples were mounted on a copper plate using non-emitting copper-dust high vacuum grease. Excitation and emission scans were iteratively performed to identify peak CNF excitation and emission characteristics.

4.4.3. Two-Photon Imaging

The custom, home-built two-photon microscope setup used consisted of a mode-locked Titanium Sapphire laser excitation source (Chameleon; Coherent, Santa Clara, California) directed into a laser scanning unit (FluoView 300; Olympus, Center Valley, Pennsylvania) which was mounted onto an upright microscope stand (BX50WI; Olympus, Center Valley, Pennsylvania). Laser power was modulated by an Electro-Optic Modulator (ConOptics, Danbury, Connecticut), operated in a power range of 1-50mW at the focal plane using a 40x 0.8NA water immersion objective. Circular polarization was used for CNF SHG imaging, verified at the focal plane by rotating a polarizer and experiencing no change in laser power. Even illumination was confirmed with a uniform ring stain on a fluorescent microsphere (FluoSpheres polystyrene, 15 μm, green; Life Technologies, Carlsbad, CA).

Cells were labeled with CellTracker Orange (CTO) CMTMR dye (ThermoFisher Scientific, Waltham, and excited at 815 nm, with epi-fluorescence emission collected at 565 nm using a 582/32 bandpass filter (Semrock, Rochester, NY). The CNF fiber structure was imaged using SHG with a laser incidence wavelength of 890 nm and backward SHG collection at 445nm using a 448/20nm bandpass filter (Semrock, Rochester, NY). Both CTO fluorescence and backwards SHG signals were detected using a H7422 GaAsP PMT (Hamamatsu, Hamamatsu City, Japan). All 3D images were acquired using 3x optical zoom, 1µm step size, laser scanning speed of 2.71s/frame and Kalman 4 averaging. The fibroblast-seeded CNF films were imaged every 24 hours for 72-hours, imaging three separate areas per film (experiment performed in triplicate) to monitor cellular proliferation.

4.4.4. CNF Photobleaching

Small square regions (42.5µm x 42.5µm) within the original 85µm field of view were photobleached using 760nm light at 49mW for approximately 55 seconds. Photobleaching was confirmed by both visual and quantitative inspection of the decrease in autofluorescence intensity of the small photobleached area in images of the CNF film acquired using 760nm excitation, emission filtered using a 582/32 (Semrock, Rochester, New York). Photobleaching in the absence of CNF fiber damage was further verified as the SHG intensity of the fibers remained constant pre/post photobleaching. Furthermore, a pixel-pixel colocalization of the pre/post photobleaching SHG images was also performed using the 'JaCoP' ImageJ plugin to confirm photobleaching in the absence of structural alterations. This method utilized Pearson's correlation coefficient as a metric for colocalization, which measures "pixel-by-pixel covariance in the signal levels of two images" where a PCC of 1 indicates perfect direct correlation, whereas PCC of -1 indicates a perfectly inverse correlation.

Once photobleaching was confirmed, a longitudinal time-lapse study was performed to examine if the photobleaching effects were permanent or if there was a recovery period. For this experiment, a CNF film was photobleached and the autofluorescence was measured as previously described at the following time-points: 0, 1, 2, 3.5. 5.5 9.5, 11.5, and 24 hours. This film was left at room temperature and humidity conditions during the length of the experiment on the microscope, and was undisturbed to not adjust the CNF material area under microscope focus (continuously image same area over time). A material topological feature distinctly visible in images was referenced as a fiduciary marker on the CNF to ensure that the same focal plane was imaged at all timepoints. A single square ROI (80 pixels by 80 pixels) consistent across each time point image was selected to include the non-photobleached CNF region, photobleached region and edge between the two (Figure 4.1A). The ROI was 'vertically condensed' by summing the raw pixel intensity values in each column and normalized by dividing corresponding summed

columns by the columns from the pre-photobleached image, yielding graphs depicting summed pixel columns on both sides (photobleached and non-photobleached) of the photobleached region edge, as shown in Figure 4.1B.

Figure 4.1 Photobleaching image analysis process. A) Example CNF photobleached region and ROI selected for photobleaching recovery analysis, B) horizontal distribution of the sum of pixel intensity across the vertically condensed ROI, displaying regions of non-photobleached and photobleached CNF.

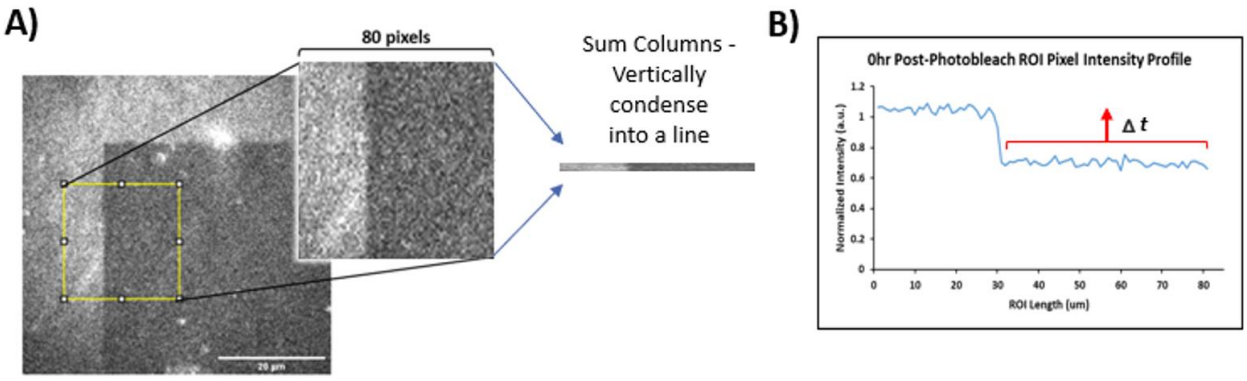

4.4.5. Cellular Proliferation Image Analysis

Three-dimensional imaging stacks of CTO labeled 3T3 fibroblasts were collected at 24, 48, and 72 hour time points and used to quantify cellular proliferation using a semi-automated CellProfiler image pipeline coupled with several 3D image processing ImageJ plugins. The entire image processing algorithm is depicted in **Figure 4.2**, and only briefly described here. All CTO fluorescence images were re-scaled and median filtered allowing for clear identification of the nuclei boundaries via user identification. Each identified nuclei was then segmented and a binary mask was applied to identify the nuclei regions within all the optical sections of the 3D image stack. Each optical section was saved as a unique image and its z-

step location within the image stack logged. Segmented binarized nuclei images were loaded into ImageJ and converted into a single 3D image stack to employ the '3D Centroid' Plugin to count individual nuclei and track the 3D centroid coordinates. The number of cells counted by the '3D Centroid' Plugin was averaged for each time point and plotted over time to assess cellular proliferation.

Figure 4.2 CellProfiler and ImageJ image analysis routine diagrams. Shown to the left are CellProfiler steps of A) Rescaling Image Intensity, B) Smoothing images using a median filter, C) Identifying primary objects (to identify nuclei) and D) Conversion of identified nuclei objects into an image. Next, image sets are exported into ImageJ, E) Converted into a 3D stack, and applied is the F) 3D Centroid Plugin.

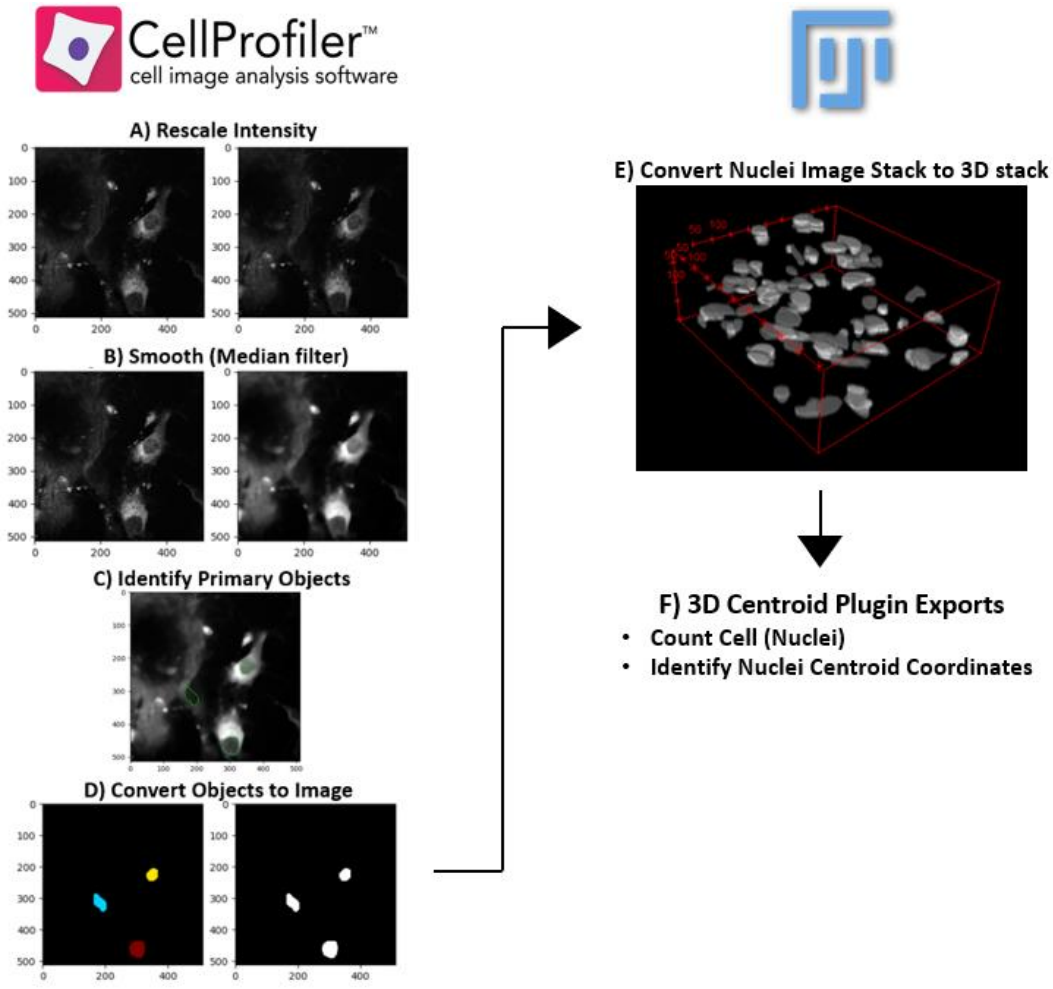

4.5. Results

4.5.1. Photobleaching Region of Interest (ROI)

As mentioned in the CNF photobleaching methods section, photobleaching was determined by quantitative inspection of the decrease in autofluorescence intensity of the small photobleached area in images of the CNF film. For this, five identical photobleaching experiments were carried out, exposing 42.5µm x 42.5µm square CNF regions to the designated photon flux for a period of 54.2 seconds. SHG and fluorescence channel images were acquired under identical acquisition parameters described in the 'Two-Photon Imaging' methods section. Images were obtained immediately before and immediately after the photobleaching experiment. An example set of collected images is displayed in Figure 4.3 A)-D). Average pixel intensities within photobleached ROIs for each channel were calculated and plotted to confirm the incidence of reduced fluorescence signal with the photobleached ROI (Figure 4.3E).

Figure 4.3 Before/After CNF/fluorescence photobleached images and ROI intensities. A) and B) show 582nm channel intensity before/after, while C) and D) demonstrate 448nm channel change in intensity before/after, respectively. These ROIs were selected and plotted to visualize change in intensity between channels.

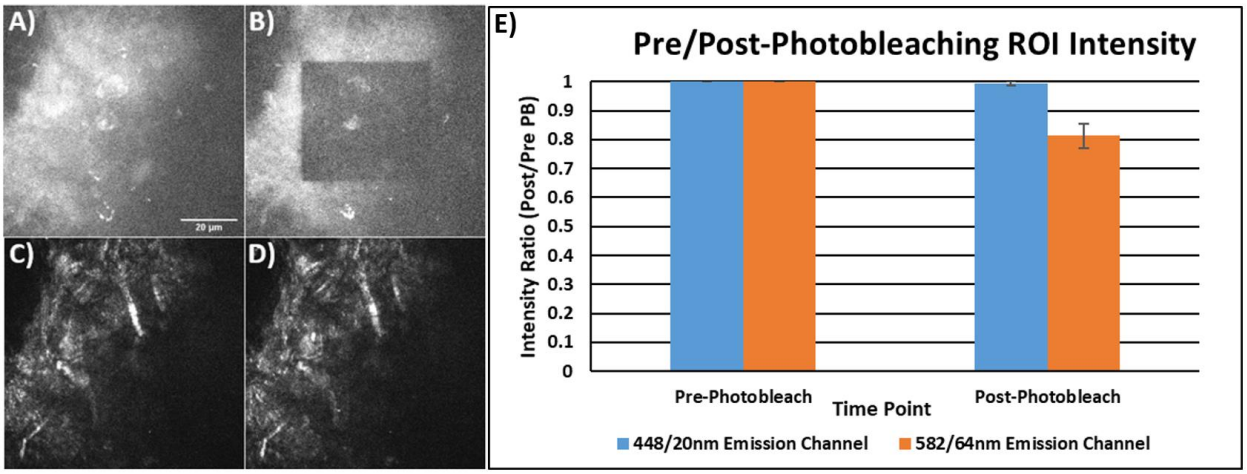

Through comparison of the average Pre and Post-photobleached ratios in each channel, it was evident that no statistically significant change in SHG channel intensity occurred after photobleaching (Orange bar, Figure 4.3E). As expected, the fluorescence (582nm) channel ROI intensity ratio did decrease by 20%, clearly demonstrating a decrease in ROI signal upon photobleaching (Blue bar, Figure 4.3E).

4.5.2. Colocalization Results

Figure 4.4 Sample colocalization quantitative and qualitative data. Set of A) Pre and B) Post-photobleached SHG images, and the corresponding Pearson's Correlation Coefficient between images. Also displayed is a separate set of C) Pre and D) Post-photobleached SHG images, assigned green and red color channels (respectively) and merged in section E), Displaying a clear distortion in color due to overlapping signal.

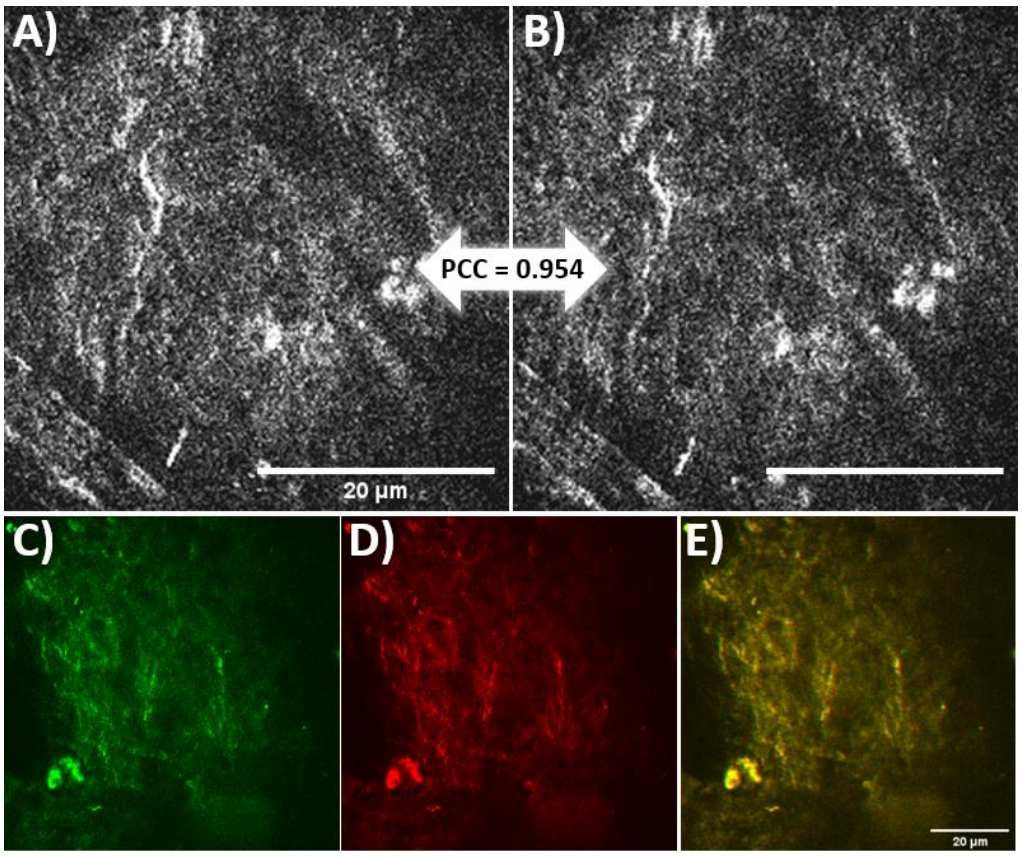

An overall average PCC value was calculated from the data set provided in Figure 4.4 A-B, to be 0.954. The extent of similarity between before/after images is blatantly observed upon assigning green and red lookup tables (which is a table of 256 entries, respective to each potential intensity value of a pixel, that allows for a user to assign RGB values to each image intensity) to pairs of images and merging the color channels, where spatially overlapping pixels experience a color distortion (as displayed in Figure 4.4 C-E).

It is clear from this data that no structural change, as observed by SHG imaging, is incurred as a result of photobleaching under the parameters described.

4.5.3. Photobleaching Recovery

Figure 4.5 Photobleaching Recovery data. Bar graph depicting the increasing ratio of photobleached area normalize pixel intensity to non-photobleached area intensity, changing over time as the material recovers to normal fluorescence emission intensity (where no photobleaching effect remains).

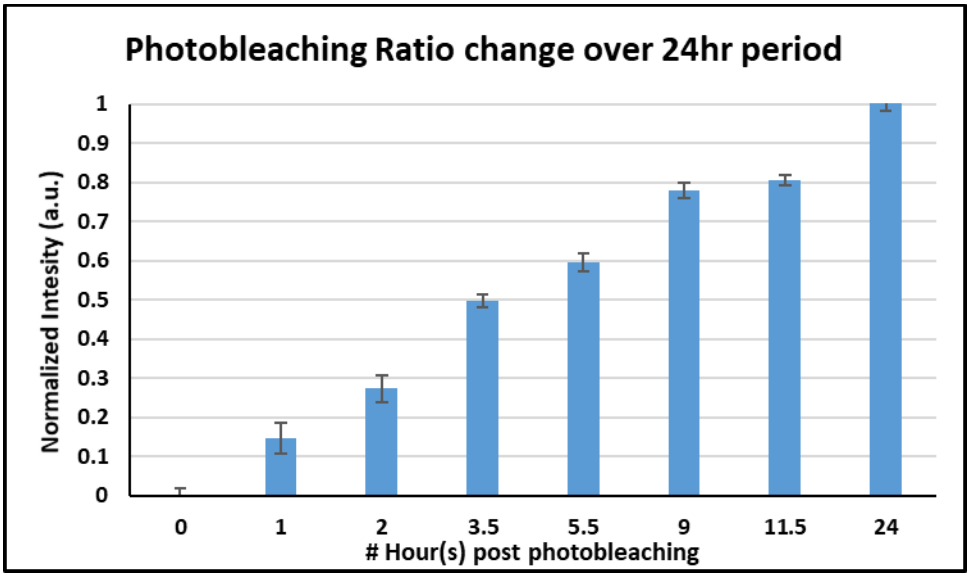

The ratios of normalized photobleached ROI pixel intensities to non-photobleached pixel intensity across the horizontal profile, depicted in Figure 4.1B, were plotted over a time period of 0-24hrs. These were calculated by taking the ratio of an average of 25 columns of non-photobleached CNF, to an average of the adjacent 45 columns of photobleached CNF (amount of columns selected as they best represented the photobleached and non-photobleached regions). To normalize the data between 0-1, where 0

represents a fully photobleached image and 1 represents a fully recovered ratio image, the value at time point 0 was subtracted from each value, bringing the minimum value (time point 0) to 0. Next, the new ratio values were subsequently divided by the new value for the pre-photobleached ratio, thus normalized to a max of 1.

The graphically represented 'percent photobleached' recovery data in Figure 4.8 indicate the photobleached region reaches the same average pixel intensity as the non-photobleached area by 24hr post-illumination. This therefore indicates that the CNF fluorescence 'recovers' from photobleaching within the 24hr period, and that photobleaching may not be a viable means to enhance CNR for long-term 'cell on CNF' studies.

4.5.4. Characterization of CNF Autofluorescence

Figure 4.6 CNF Diffuse Reflectance Spectroscopy data of CNF.

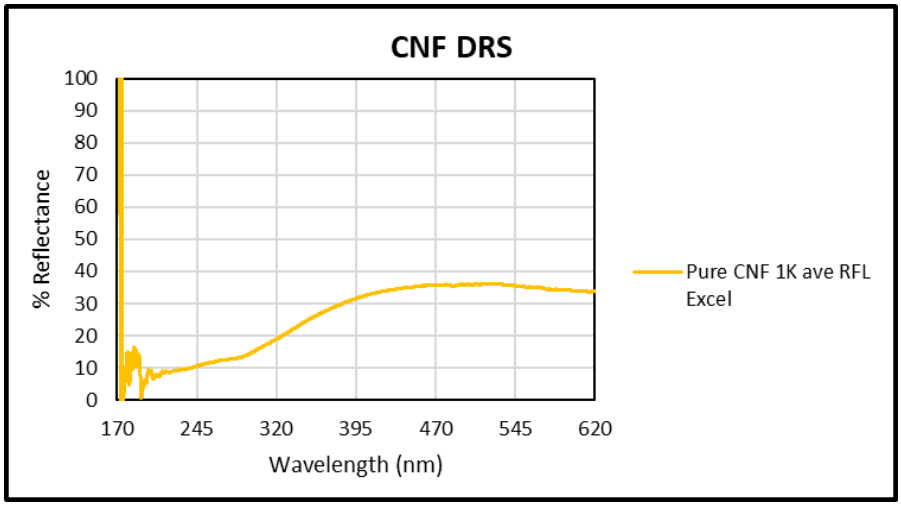

The CNF displayed a strong absorption band was observed below 500nm, indicated by the edge of gradually declining % reflectance roughly between 320-490nm. It is clear that the relative % reflectance

was lower than 40% across the entire spectrum, indicating potential absorption across the spectra. With the lagging optical edge and capacity for absorption below 500nm, a further investigation of excitation/emission fluorescence characteristics was warranted.

Figure 4.7 Steady state luminescence data from CNF. Spectra displays a strong excitation peak at 420nm and emission peak at 635nm, with small intensity of emission present across a broad range from 370-720nm.

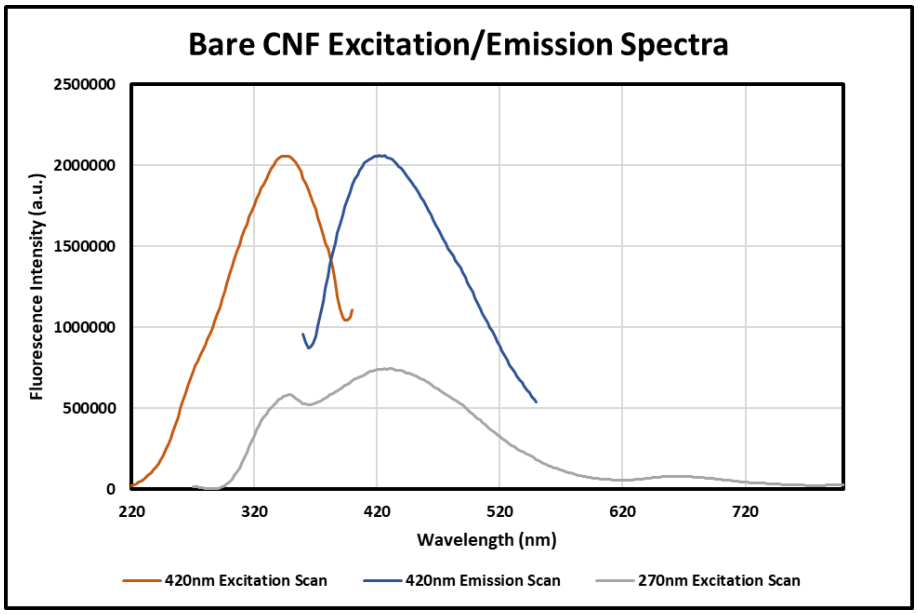

Excitation and emission scans were iteratively performed to identify peak excitation and emission characteristics of CNF, yielding spectra displayed in **Figure 4.8** above. A clear absorption band was observed between 300-390nm, with a peak at 350nm, which was demonstrated to correspond to an emission band between 395-490nm, with peak emission at 420nm.

An additional emission spectra of the CNF was obtained exciting at 270nm, revealing both the predominant peak at 420nm and an additional minor broad peak around 662nm, spanning roughly 630-

720nm. While the emission observed from CNF spans broadly from roughly 370-720nm, the peak intensity at 662nm is roughly 11% that of the predominant emission peak at 420nm. Therefore, while fluorescence may be present in regions above 520nm, this decrease in intensity represents a viable optical window for a fluorescent label to be utilized, where contrast could be optimized for multimodal imaging of cells on CNF.

4.5.5. Cellular Proliferation

As mentioned in the methods section, the image analysis routine identified cell nuclei, reconstructed nuclei images into 3D nuclei maps, and counted the amount per 3D stack. 3D image reconstructions and nuclei counts were performed for each time point; example 24, 48 and 72hr stacks are provided in Figure 4.9A-C. Cell counts from each time point (n=9 stacks) were averaged and plotted to quantify change in amount of cells over time, providing a quantitative metric for cellular proliferation. The bar chart is provided in Figure 4.9D.

Figure 4.8 Sample nuclei 3D stacks and cell counting results. Displayed is a sample 3D stack at A)24hr, b) 48hr and C)72hr. D) Bar chart displaying cell proliferation on CNF results.

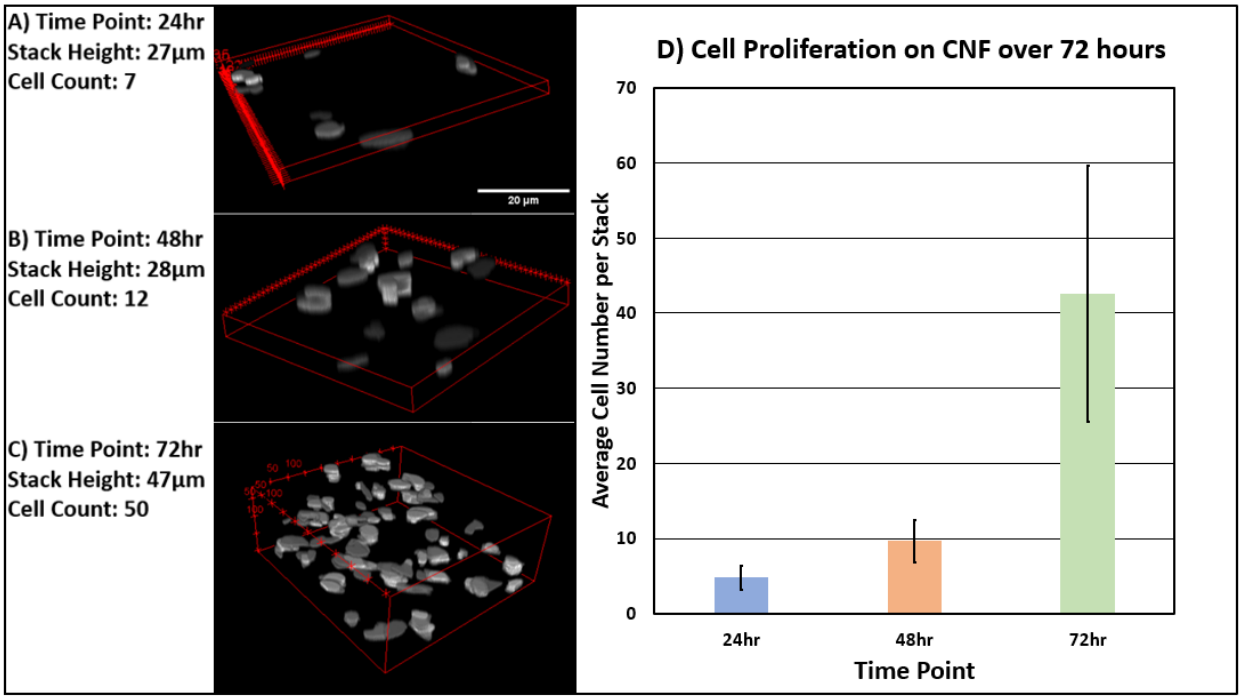

A statistically significant increase in cell number per stack was observed as time progressed, between 24-48hrs, and 48-72hrs. Statistical significance was determined by employing a Wilcoxon rank sum test, where p-values for 24-48, and 48-72 time points were 0.0024 and 0.0017, respectively.

At 24, 48 and 72hr, the mean cell counts (rounded up to the nearest whole number) were 5, 10, and 43, respectively. A significant increase in growth was observed between the 48-72hr time points compared to 24-48hr, which can most likely be attributed to the doubling time of the NIH 3T3 cells of between 20-30hrs, resulting in rapid growth over a second doubling period between 48-72hrs of growth.

During imaging, it was noted that one sample imaging at the 48hr time point displayed unique visual characteristics, appearing likely to have only had a portion of the CNF film submerged in media – resulting in a significant amount of cell death on the sample. Therefore, this portion of the 48hr image stacks was

excluded from analysis, leaving the stack sample size at each time point to be: 24hr n=9, 48hr n=6, and 72hr n=9.

4.6. Discussion

4.6.1. Photobleaching Results

The purpose of the initial photobleaching and colocalization analysis was to determine if a CNF structural change or damage was induced as a result of laser damage. It was visually clear through comparison of before/after images in each channel (Figure 4.3A-D) and quantitatively evident in the plotted results (Figure 4.3E) that there was an intensity decrease in the 582nm channel, but not the 448nm channel. It is important to remember that the information collected in the 448nm channel was in fact second harmonic signal, and SHG is produced strictly due to the nature of non-centrosymmetric structures and is not related to a fluorescence emission event. Therefore, this data demonstrated that the CNF was not being damage or structurally altered by laser exposure, rather, was likely experiencing some type of photobleaching effect.

This additionally indicated that CNF fluorescence and SHG signal minimally overlapped (enough so to allow for individual imaging through each channel and performance of image processing adequate to make conclusions in this study). Identification of a SHG signal acquisition parameter isolated from undesirable background fluorescence was a promising indicator that non-invasive, label-free imaging of the material would be possible.

The consistent amount of SHG signal generated in the Pre and Post-Photobleached images was a promising superficial indicator that the sample was not damaged, however, a more rigorous image

analysis technique to demonstrate no structural change occurred was necessary. This need brought about the utilization of the PCC colocalization metric.

4.6.2. Colocalization Results

The positive PCC values obtained from utilizing the 'JaCoP' colocalization ImageJ plugin, combined with visual inspection of images indicate that the CNF fiber presence and position were not altered upon photobleaching, therefore, the reduction in photobleached ROI fluorescence signal could more likely be attributed to a photobleaching phenomenon where fluorescent emission was quenched by high energy absorbancein the ROI. For the purpose of imaging cellular components on the surface of the material, the ability to photobleach and remove CNF fluorescence represents an advantageous means to allow for label-free imaging of intrinsic cellular fluorescence from co-enzymes NADH and FAD. However, for this approach to be meaningfully useful in a long-term study of cell conduction into the material, it would be necessary for the photobleaching effect be irreversible.

4.6.3. Photobleaching Recovery Results

As clearly illustrated by the results in Figure 4.6, CNF autofluorescence signal within the photobleached ROI returned, or recovered, within a 24hr period.

The mechanism of this recovery is difficult to determine, as there are numerous factors to consider when quantifying contribution of fluorescence recovery after photobleaching. In general, it is well known that intense illumination causes photobleaching of the fluorescent molecules within the excited area, which in turn creates a diffusion gradient that causes an inflow of fluorophores from the surrounding area into the photobleached region. The diffusion of these fluorophores has been a well-studied field, where models

are applied to represent the mechanism of diffusion. These models more strongly fit the data as more is known about system factors such as: Arrangement of the fluorophores, structural hierarchy and heterogeneity of the fluorescent and non-fluorescent species, and polydispersity of the fluorescent species [138]. With many of these properties of CNF still unknown (especially the specific species contributing to fluorescence emission), it is difficult to confidently fit a model to this fluorescence recovery data. Similar work has indicated that complimenting multiphoton methods such as the one used in this work with SHG and fluorescence, can validate at least whether structural degradation occurred within the system, by using a probing technique sensitive to structural integrity (such as SHG), which was observed in this work [139]. Based off this, it can at least be strongly assumed that the observed decrease and subsequent recovery of fluorescence signal was in fact a photobleaching effect, not a result of sample damage.

To mathematically understand the energy required to induce such an effect, photon flux was calculated.

CNF films were exposed to 760nm excitation light at 49mW that scanned across focal areas of dimensions 42.5um by 42.5um (1892.25 um2) for a period of 54.2 seconds. To calculate photon flux, we first find the energy of an incident photon in this specific experiment using the Plank-Einstein relation 134.

Equation 4.1 Plank-Einstein relation

$$E = h\nu$$

Where E is photon energy, h is Planck's constant, and v is frequency. The frequency can also be expressed by:

Equation 4.2 Expression for frequency

$$v = \frac{c}{\lambda}$$

Where c is the speed of light and λ is wavelength (nm). Therefore, the equation for photon energy becomes:

Equation 4.3 Energy of a photon

$$E = \frac{hc}{\lambda}$$

The both Planck's constant and the speed of light are constants, where h = 6.626 x 10-34m2kg/s (roughly), and c = 3 x 108m/s (roughly), and λ = 760nm for the photobleaching experiment 135. Plugging these values in gives:

Equation 4.4 Energy of a photon (solved)

$$E = \frac{hc}{\lambda} = \frac{(6.626\ x\ 10^{-34} m^2 kg/s\ )(3\ x\ 10^8 m/s)}{760nm} = 2.6137\ x\ 10^{-19}\ \frac{Joules}{photon}$$

Where the energy of an incident photon is equal to 2.6137 x 10-19 Joules (J).

As mentioned in the 'Design and Construction' section, power of the beam below the objective was measured across a range of values at both 890nm and 760nm wavelengths, therefore, power delivered

to the sample as a function of time is known to be 49mW at the 760nm excitation. By substituting Joules/second in for Watts, amount of photons/second can be calculated:

Equation 4.5 Photons per second

$$\frac{49\,\frac{Joules}{second}}{2.6137\ x\ 10^{-19}\,\frac{Joules}{photon}} = 1.8747\ x\ 10^{20}\,\frac{photon}{second}$$

As photon flux (Φ) is a function of time and area, dividing amount of photons/second by the illumination area yields the value for photon flux:

Equation 4.6 Photon flux

$$\Phi = \frac{1.8747\ x\ 10^{20}\,\frac{photon}{second}}{illumination\ area} = \frac{1.8747\ x\ 10^{20}\,\frac{photon}{second}}{1892.25\mu m^2} = 9.9\ x\ 10^{16}\,\frac{photon}{second\cdot \mu m^2}$$

This calculation indicates that CNF exposure to a photon flux of roughly 9.9 x 1016 photon/(second·µm2) results in the maximum extent of 'photobleachability' (or change of intensity within the region of interest (ROI)); an extremely high amount of energy.

While the recovery data does demonstrate that CNF films prepared by the described method have the potential to be photobleached, due to the swift recovery time and high energy requirements, photobleaching may not prove to be useful to enhance contrast for long-term multiphoton studies. This presence of fluorescence emitted from CNF upon illumination represents a potential downfall when

considering applications imaging cells embedded in CNF, as emission between channels may overlap, resulting poor contrast-to-noise ratio images that render cellular analysis difficult or impossible. Therefore, a more thorough understanding of CNF fluorescent properties was necessary for designing an adequate two-photon imaging method. To do so, CNF film excitation/emission properties were characterized by diffuse reflectance and steady-state luminescence spectroscopy.

4.6.4. Characterization of CNF Autofluorescence

The DRS data provided a useful foothold to gain a superficial understanding of potential absorption (or at least, lack of reflection), by CNF. As shown in Figure 4.7, the CNF displayed strong absorption below 500nm, which was characterized by lower reflectance and of particular interest was the lagging edge between 320-490nm – used as a reference point to guide further investigation of peak excitation somewhere within this range.

This deeper investigation into these spectral characteristics was performed by SSLS, which iteratively fixed excitation and emission to arrive at peak excitation/emission wavelengths. Figure 4.8 displays two gaussian-shaped peaks representative of peak excitation and emission, at 350nm and 420nm, respectively. It is important to note that an additional spectra is included, that illustrates the broad CNF fluorescent emission across the spectrum, with considerably lower intensity (roughly 11% of the peak emission) emitted above 520nm. This region of low emission intensity represented a potential optical window to take advantage of, where contrast could be optimized for multimodal images of cells on CNF by selected cell fluorophore labels that emit above 520nm.

4.6.5. Applicable Dyes

Considering the low CNF fluorescence signal at higher wavelengths, a range of fluorescent cell labels could be utilized for such multimodal 'cell on CNF' imaging. These labels can bind to many types of cellular receptors and serve to provide a wealth of singe-cell functional information, as depicted by the numerous potential label candidates in Table 4.1.

Table 4.1 Fluorescent labels ideal for imaging outside CNF peak emission [140]. (label names, applications and values reproduced from Cahalan et al.) [141].

Application	Label Name	Peak Excitation Wavelength (nm)	Peak Emission Wavelength (nm)
Intracellular calcium measurements	Yellow cameleon	780nm	535nm
	Fura-2 free	720nm	512nm
Protein conjugates	FITC	780nm	519nm
	Texas red	780nm	615nm
Organelle Visualization	DAPI (nucleus)	700nm	565nm
	Rhodamine 123 (mitochondria)	780nm	550nm
Cell Tracking & Morphology	CellTracker Orange CMTMR	815nm	565nm
	SNARF-1	700-810	580-640nm

4.6.6. Cell Proliferation Discussion

In this study, proliferation is directly correlated to (and interpreted as) cell count, therefore our method proved to be viable process for observing and quantifying the cellular characteristic of proliferation. We

observed statistically significant growth between the 24-48hr, and 48-72hr time points, with significant increase in growth occurring between the 48-72hr time points compared to 24-48hr. This can most likely be attributed to the doubling time of the NIH 3T3 cells of between 20-30hrs, resulting in rapid growth over a second doubling period between 48-72hrs of growth.

Overall observation of cellular growth on the surface of the CNF revealed cells located in varying depths in the Z-axis, illustrating migration into the material around fiber geometries. The combination of two-photon fluorescence imaging CTO labeled cells and SHG signal from CNF proved to be a viable combination of techniques for imaging and visualizing cellular growth onto and into CNF scaffolds. The multitude of attributes capable of being derived from cell morphology obtained from utilization of this two-photon imaging method, combined with the wide availability of additional labels for probing of more specific cellular features (Table 4.1) represents significant potential for understanding the three-dimensional nature of cellular growth into polysaccharide-based materials such as CNF.

It is worth noting that creation and demonstration of this valid image analysis routine can provide a wealth of additional information, one such piece of information is cell penetration or height relative to the CNF. In these image sets, larger image stack sizes were collected to account for increasingly more thick layers of cells residing on the surface of the CNF, therefore cells were located at varying heights within the stack. To quantify height, one could use the center of mass of a 3D object – a metric calculated in the described image analysis routine during the '3D centroid' step. This already in-hand value can be simply compared to corresponding XY coordinate Z-axis height of the CNF, to create a metric for cell penetration into the CNF or growth of additional layers on top of the CNF. In addition, the coordinates of these nucleus centers of mass can be mapped over time to result in a means of observing cell migration into or across the CNF. Finally, the three-dimensional reconstruction of nuclei boundary objects performed in ImageJ resulted in

3D stacks of objects with well-defined shapes (shown in Figure 4.9). It is well known that nuclei shape (e.g. circular, elongated, fragmented) can be indicative of cell viability or permeability.

4.7. Concluding Summary

With the rising interest in using polysaccharide polymers as biomaterials, the development novel methods to non-invasively monitor the natural three-dimensional growth and maturation of cells within these material candidates becomes ever more useful and necessary. In this study, we investigated CNF optical properties and first found a viable window displaying low amounts of autofluorescence, representing an ideal window to utilize cellular fluorescent label for cell visualization. We combined this knowledge with the use of SHG imaging to visualize the CNF material, resulting in a multimodal method for observing the interaction between cells and CNF materials. To demonstrate the viability of this method to provide useful information, we quantified longitudinal three-dimensional growth of cells within the material, by obtaining 3D images of cells growing on the CNF 24hr, 48hr and 72hr after seeding cells on the material. These 3D image stacks were analyzed by a simple image analysis method we developed, using CellProfiler to identify nuclei boundaries, and ImageJ to reconstruct these nuclei in 3D and count amount per 3D stack. This resulted in our ability to quantify statistically significant cell growth over the 72hr period, and overall demonstrated the viability of the multimodal imaging method to provide a wealth of information pertaining to cell function and growth, on and within the material.

It is clear that this method has the potential to aid in other 3D assessments of biological species or analytes in SHG-active or CNF structures. In this work we provided a table of additional dyes for use as contrast agents imaging the cell and material interface, applicable for materials with similar optical characteristics to the CNF used in this study. Overall, this method can be applicable in a wide variety of exciting applications, such as drug delivery through a porous cellulose membrane, nutrient transfer through a

polysaccharide polymer-based 3D cell culture system – constituting a new tool to evaluate overall biocompatibility of novel 3D scaffolds for tissue regeneration.

CONCLUSION

The field of optics has been revolutionized with the realization and application of two-photon microscopy, which has come a long way since the inception of the theoretical concept by Maria Göppert-Mayer in 1931. It is a powerful tool for probing biological and material systems characteristics, gaining accelerated adoption in the research field over the decades. This thesis simply overviewed the application of two-photon microscopy for single cell metabolism and imaging the cellular-material interface, however, current and future applications span widely beyond what was discussed for both research and industry.

As the utility of two-photon becomes increasingly more realized, two-photon microscopists and engineers continue to innovate, and hardware/optical components become more condensed, available and rigid, the potential for two-photon to span out of the research field and into diagnostics and treatments will be an exciting time, which is already beginning to occur. The pairing of two-photon microscopy with other microscopy techniques, such as RAMAN spectroscopy and diffuse optics approaches will be a blue ocean for research deriving complementary information to further understand biological mechanisms within tissues and single cells. Work such as that performed in the thesis highlighting a novel use-case of the combination of two-photon fluorescence and second-harmonic generation imaging further cement the wide breadth of two-photons microscopy's unrealized applications - encouraging scientists and engineers to look with excitement to the bright future of nonlinear microscopy.

BIBLIOGRAPHY

1. Paddock, S. W., Fellers, T. J. & Davidson, M. W. Introductory Confocal Concepts. 7 Available at: https://www.microscopyu.com/techniques/confocal/introductory-confocal-concepts. (Accessed: 6th May 2019)

2. Minsky, M. Memoir on Inventing the Confocal Scanning Microscope. *Scanning* **10**, 128–138 (1987).

3. Sheppard, C. J. R. Confocal microscopy. The Development of a Modern Microscopy. *Encycl. Biomater. Biomed. Eng.* 41–47 (1990). doi:10.1081/E-EBBE-120024153

4. Jonkman, J. & Brown, C. M. Any way you slice it—A comparison of confocal microscopy techniques. *J. Biomol. Tech.* **26**, 54–65 (2015).

5. St Croix, C. M., Shand, S. H. & Watkins, S. C. Confocal microscopy: comparisons, applications, and problems. *Biotechniques* **39**, (2005).

6. Sachs, R. G. Maria Goeppert Mayer 1906—1972. (1979).

7. Göppert-Mayer, M. fiber Elementarakte mit xwei QuantemspWwgem. **114**, (1928).

8. Rumi, M. & Perry, J. W. Two-photon absorption: an overview of measurements and principles. *Adv. Opt. Photonics* **2**, 451 (2010).

9. Kaiser, W. K., Garrett & C.G.B. Two-Photon Excitation in CaF2:Eu2+. *Phys. Rev. Lett.* **7**, 229–231 (1961).

10. Denk, W., Strickler, J. & Webb, W. Two-photon laser scanning fluorescence microscopy. *Science (80-.).* **248**, 73–76 (1990).

11. Young, M. D., Field, J. J., Sheetz, K. E., Bartels, R. A. & Squier, J. A pragmatic guide to multiphoton microscope design Michael. **7**, 276–378 (2016).

12. Masters, B. R. & So, P. T. C. Antecedents of Two-Photon Excitation Laser Scanning Microscopy. *Microsc. Res. Tech.* **63**, 3–11 (2004).

13. NIH Pubmed. Available at: https://www.ncbi.nlm.nih.gov/pubmed/.

14. Van Stryland, E. W., Woodall, M. A., Vanherzeele, H. & Soileau, M. J. Energy band-gap dependence of two-photon absorption. *Opt. Lett.* **10**, 490 (2008).

15. Newport & Spectra-Physics. *Application Note: Two-Photon Excited Fluorescence Microscopy*. *Technology and Applications Center - Newport Corporation* (2007).

16. Stokes, G. G. On the Change of Refrangibility of Light. 463–562 (1852).

17. Svoboda, K. & Yasuda, R. Principles of Two-Photon Excitation Microscopy and Its Applications to Neuroscience. *Neuron* **50**, 823–839 (2006).

18. So, P. T. C., Hosseini, P., Dong, C. Y. & Masters, B. R. Two-photon excitation fluorescence microscopy. *Biomed. Photonics Handbook, Second Ed. Fundam. Devices, Tech.* 417–434 (2014). doi:10.1201/b17290

19. Richards, B. & Wolf, E. Electromagnetic diffraction in optical systems, II. Structure of the image field in an aplanatic system. *Proc. R. Soc. London. Ser. A. Math. Phys. Sci.* **253**, 358–379 (2006).

20. Zipfel, W. R., Williams, R. M. & Webb, W. W. Nonlinear magic: multiphoton microscopy in the biosciences. *Nat. Biotechnol.* **21**, 1369–77 (2003).

21. Liu, T. M., Conde, J., Lipiński, T., Bednarkiewicz, A. & Huang, C. C. Revisiting the classification of NIR-absorbing/emitting nanomaterials for in vivo bioapplications. *NPG Asia Mater.* **8**, 1–25 (2016).

22. Rubart, M. Two-photon microscopy of cells and tissue. *Circ. Res.* **95**, 1154–1166 (2004).

23. Helmchen, F. & Denk, W. Deep tissue two-photon microscopy. *Nat. Methods* **2**, 932–940 (2005).

24. Diffuse Optical Spectroscopic Imaging. *Beckman Laser Institute and Medical Clinic* Available at: https://dosi.bli.uci.edu/research/.

25. Coherent. *Chameleon Ultra ™ and Diode-Pumped Lasers*. *Current*

26. Conoptics. *User's Guide Modulator Alignment Procedure series User Guide Modulator Alignment Procedure User Guide Modulator Alignment Procedure*. (2009).

27. Volodymyr, N. & Rafael, Y. A Practical Guide How to Build a Two-Photon Microscope Using a Confocal Scan Head.

28. Chen, X., Nadiarynkh, O., Plotnikov, S. & Campagnola, P. J. Second harmonic generation microscopy for quantitative analysis of collagen fibrillar structure. *Nat. Protoc.* **7**, 654–69 (2012).

29. Edmund. Understanding Waveplates. 6 (2019). Available at: https://www.edmundoptics.com/resources/application-notes/optics/understanding-waveplates/. (Accessed: 5th May 2019)

30. Olympus. Objectives. *Life Science* Available at: https://www.olympus-lifescience.com/en/objectives/lumplfln-w/.

31. Musselli, C., Livingston, P. O. & Ragupathi, G. Keyhole limpet hemocyanin conjugate vaccines against cancer: the Memorial Sloan Kettering experience. *J. Cancer Res. Clin. Oncol.* **127 Suppl**, R20-6 (2001).

32. Cancer Statistics. *National Cancer Institute* (2018). Available at: https://www.cancer.gov/about-cancer/understanding/statistics.

33. Skin Cancer (Non-Melanoma): Treatment Options. (2016). Available at: http://www.cancer.net/cancer-types/skin-cancer-non-melanoma/treatment-options.

34. Thorens, B. & Mueckler, M. Glucose Transporters in the 21st Century. *Endocrinol Metab* **298**, 141–145 (2010).

35. Birsoy, K. *et al.* An essential role of the mitochondrial electron transport chain in cell proliferation is to enable aspartate synthesis. **118**, 6072–6078 (2016).

36. Hay, N. Reprogramming glucose metabolism in cancer : can it be exploited for cancer therapy ? *Nat. Publ. Gr.* (2016). doi:10.1038/nrc.2016.77

37. Zheng, J. Energy metabolism of cancer: Glycolysis versus oxidative phosphorylation (review). *Oncol. Lett.* **4**, 1151–1157 (2012).

38. Vander Heiden, M. G., Cantley, L. C. & Thompson, C. B. Understanding the Warburg Effect: The Metabolic Requirements of Cell Proliferation. *Science (80-.).* **324**, 1029–1033 (2009).

39. Solaini, G., Sgarbi, G. & Baracca, A. Oxidative phosphorylation in cancer cells. *Biochim. Biophys. Acta - Bioenerg.* **1807**, 534–542 (2011).

40. Kalyanaraman, B. Redox Biology Teaching the basics of cancer metabolism : Developing antitumor strategies by exploiting the di ff erences between normal and cancer cell metabolism. *Redox Biol.* **12**, 833–842 (2017).

41. Chance, B., Schoener, B., Oshino, R., Itshak, F. & Nakase, Y. Oxidation-Reduction Ratio Studies of Mitochondria in Freeze-trapped. **254**, (1979).

42. Arteaga, C. L. & Skala, M. C. metabolism predicts drug response in breast cancer. **74**, 5184–5194 (2015).

43. Rice, W. L., Kaplan, D. L. & Georgakoudi, I. Two-photon microscopy for non-invasive, quantitative monitoring of stem cell differentiation. *PLoS One* **5**, (2010).

44. Mujat, C. *et al.* Endogenous optical biomarkers of normal and human papillomavirus immortalized epithelial cells. *Int. J. Cancer* **122**, 363–371 (2008).

45. Levitt, J. M. *et al.* Intrinsic fluorescence and redox changes associated with apoptosis of primary human epithelial cells. *J. Biomed. Opt.* **11**, 064012 (2006).

46. Ostrander, J. H. *et al.* Optical Redox Ratio Differentiates Breast Cancer Cell Lines Based on Estrogen Receptor Status. *Cancer Res.* **70**, 1–14 (2013).

47. Uinn, Q. & Ajaram, N. A. R. Optical redox ratio identifies metastatic potential-dependent changes in breast cancer cell metabolism. **7**, 4364–4374 (2016).

48. Zhang, Z. *et al.* Redox ratio of mitochondria as an indicator for the response of photodynamic therapy. *J. Biomed. Opt.* **9**, 772 (2004).

49. Yu, F. *et al.* On chip two-photon metabolic imaging for drug toxicity testing. *Biomicrofluidics* **11**, 1–11 (2017).

50. Chang, T. *et al.* Non-invasive monitoring of cell metabolism and lipid production in 3D engineered human adipose tissues using label-free multiphoton microscopy. **34**, 1–21 (2014).

51. Armstrong, D. Multiphoton Redox Ratio Imaging for Metabolic Monitoring in vivo. *Adv. Protoc. Oxidative Stress III* 1–477 (2014). doi:10.1007/978-1-4939-1441-8

52. Skala, M. C. *et al.* In vivo multiphoton microscopy of NADH and FAD redox states , fluorescence lifetimes , and cellular morphology in precancerous epithelia. (2007).

53. Wu, S. *et al.* Quantitative evaluation of redox ratio and collagen characteristics during breast cancer chemotherapy using two-photon intrinsic imaging. *Biomed. Opt. Express* **9**, 1375 (2018).

54. Georgakoudi, I. & Quinn, K. P. Optical Imaging Using Endogenous Contrast to Assess Metabolic State. *Annu. Rev. Biomed. Eng.* **14**, 351–367 (2012).

55. Shah, A. T. *et al.* Optical Metabolic Imaging of Treatment Response in Human Head and Neck Squamous Cell Carcinoma. **9**, (2014).

56. Skala, M. C. *et al.* Multiphoton Microscopy of Endogenous Fluorescence Differentiates Normal , Precancerous , and Cancerous Squamous Epithelial Tissues. 1180–1187 (2005).

57. Bolton, J. C. *et al.* Spectroscopic Analysis of Hemolymph from the American Lobster (*Homarus americanus*). *J. Shellfish Res.* **28**, 905–912 (2009).

58. Bolton, J. C., Bayer, R., Bushway, R., Collins, S. & Perkins, B. Analytical and Semipreparative HPLC Analysis and Isolation of Hemocyanin from the American Lobster *Homarus americanus*. *J. Shellfish Res.* **33**, 11–17 (2014).

59. Becker, M. I., Arancibia, S., Salazar, F., Del Campo, M. & De Ioannes, A. Mollusk Hemocyanins as Natural Immunostimulants in Biomedical Applications. *Immune Response Act.* (2014). doi:10.5772/57552

60. McFadden, D. W., Riggs, D. R., Jackson, B. J. & Vona-Davis, L. Keyhole limpet hemocyanin, a novel immune stimulant with promising anticancer activity in Barrett's esophageal adenocarcinoma. *Am. J. Surg.* **186**, 552–555 (2003).

61. Jiewkok, A., Tsukimura, B. & Utarabhand, P. Purification and molecular cloning of hemocyanin from Fenneropenaeus merguiensis(de Man, 1888): Response to Vibrio harveyi exposure. *J. Crustac. Biol.* **35**, 659–669 (2015).

62. Swaminathan, A., Lucas, R. M., Dear, K. & McMichael, A. J. Keyhole limpet haemocyanin - A model antigen for human immunotoxicological studies. *Br. J. Clin. Pharmacol.* **78**, 1135–1142 (2014).

63. Harris, J. R. & Markl, J. Keyhole limpet hemocyanin (KLH): a biomedical review. doi:10.1016/S0968-4328(99)00036-0

64. McFadden, D. W., Riggs, D. R., Jackson, B. J., Ng, A. & Cunningham, C. Keyhole limpet hemocyanin potentiates standard immunotherapy for melanoma. *Am. J. Surg.* **193**, 284–7 (2007).

65. Dolashka, P. *et al.* Antitumor activity of glycosylated molluscan hemocyanins via Guerin ascites tumor. *Immunol. Invest.* **40**, 130–149 (2011).

66. Gesheva, V. *et al.* Anti-cancer properties of gastropodan hemocyanins in murine model of colon carcinoma. *BMC Immunol.* **15**, 1–11 (2014).

67. Arancibia, S. *et al.* A novel immunomodulatory hemocyanin from the limpet Fissurella latimarginata promotes potent anti-tumor activity in melanoma. *PLoS One* **9**, (2014).

68. L.M., K. *et al.* Vaccination of Small Cell Lung Cancer Patients with Polysialic Acid or N-Propionylated Polysialic Acid Conjugated to Keyhole Limpet Hemocyanin. *Clin. Cancer Res.* **10**, 916–923 (2004).

69. Brisson, C., Ph, D., Lincicum, B. & Biotechnologies, S. Keyhole Limpet Hemocyanin (KLH): Protecting the Sole Marine Source of an Important Pharmaceutical Product. 2014 (2014).

70. Eisemann, J. D., Fagerstone, K. A. & O'Hare, J. , R. Wildlife Contraceptives: A Regulatory Hot Potato. *Proc. Vertebr. Pest Conf.* **22**, (2019).

71. Pizarro-Bauerle, J. *et al.* Molluskan hemocyanins activate the classical pathway of the human complement system through natural antibodies. *Front. Immunol.* **8**, (2017).

72. Moltedo, B. *et al.* Immunotherapeutic Effect of Concholepas Hemocyanin in the Murine Bladder Cancer Model : Evidence for Conserved Antitumor Properties Among Hemocyanins. **176**, 2690–2695 (2006).

73. Gesheva, V. *et al.* Helix pomatia hemocyanin - A novel bio-adjuvant for viral and bacterial antigens. *Int. Immunopharmacol.* **26**, 162–168 (2015).

74. Teitz-Tennenbaum, S., Li, Q., Davis, M. A. & Chang, A. E. Dendritic cells pulsed with keyhole limpet hemocyanin and cryopreserved maintain anti-tumor activity in a murine melanoma model. *Clin. Immunol.* **129**, 482–91 (2008).

75. Zhong, T.-Y. *et al.* Hemocyanins Stimulate Innate Immunity by Inducing Different Temporal Patterns of Proinflammatory Cytokine Expression in Macrophages. *J. Immunol.* **196**, 4650–4662 (2016).

76. Zanjani, N. T. *et al.* Abalone Hemocyanin Blocks the Entry of Herpes Simplex Virus 1 into Cells : a Potential New Antiviral Strategy. **60**, 1003–1012 (2016).

77. Pan, J. Y., Zhang, Y. L., Wang, S. Y. & Peng, X. X. Dodecamer is required for agglutination of Litopenaeus vannamei hemocyanin with bacterial cells and red blood cells. *Mar. Biotechnol.* **10**, 645–652 (2008).

78. Dolashka, P. *et al.* Glycan structures and antiviral effect of the structural subunit RvH2 of Rapana hemocyanin. *Carbohydr. Res.* **345**, 2361–2367 (2010).

79. Presicce, P., Taddeo, A., Conti, A., Villa, M. L. & Della Bella, S. Keyhole limpet hemocyanin induces the activation and maturation of human dendritic cells through the involvement of mannose receptor. *Mol. Immunol.* **45**, 1136–1145 (2008).

80. Liu, J. *et al.* The effects of hemocyanin on T cells cultured in vitro. *Oncol. Lett.* **15**, 2655–2660 (2018).

81. BOYANOVA, O., DOLASHKA, P., TONCHEVA, D., RAMMENSEE, H.-G. & STEVANOVIĆ, S. In vitro effect of molluscan hemocyanins on CAL-29 and T-24 bladder cancer cell lines. *Biomed. Reports* **1**, 235–238 (2013).

82. Salama, W. M. & Mona, M. M. In vitro anti-tumor effects of hemocyanin isolated from Atergatis roseus and Eriphia verrucosa crabs. (2019).

83. Guncheva, M. *et al.* Modification of Rapana thomasiana hemocyanin with choline amino acid salts significantly enhances its antiproliferative activity against MCF-7 human breast cancer cells. *RSC Adv.* **5**, 63345–63354 (2015).

84. Velkova, L. *et al.* Structure of hemocyanin from garden snail Helix lucorum. *Comp. Biochem. Physiol. - B Biochem. Mol. Biol.* **157**, 16–25 (2010).

85. Antonova, O. *et al.* In vitro antiproliferative effect of helix aspersa hemocyanin on multiple malignant cell lines. *Zeitschrift fur Naturforsch. - Sect. C J. Biosci.* **69 C**, 325–334 (2014).

86. Riggs, D. R., Jackson, B. J., Vona-Davis, L., Nigam, A. & McFadden, D. W. In vitro effects of keyhole limpet hemocyanin in breast and pancreatic cancer in regards to cell growth, cytokine production, and apoptosis. *Am. J. Surg.* **189**, 680–684 (2005).

87. Riggs, D. R., Jackson, B., Vona-Davis, L. & McFadden, D. In Vitro Anticancer Effects of a Novel Immunostimulant: Keyhole Limpet Hemocyanin. *J. Surg. Res.* **108**, 279–284 (2002).

88. Somasundar, P., Riggs, D. R., Jackson, B. J. & McFadden, D. W. Inhibition of melanoma growth by hemocyanin occurs via early apoptotic pathways. *Am. J. Surg.* **190**, 713–716 (2005).

89. Zheng, L. *et al.* Hemocyanin from Shrimp Litopenaeus vannamei Has Antiproliferative Effect against HeLa Cell In Vitro. *PLoS One* **11**, e0151801 (2016).

90. Zhang, Z. *et al.* Glycosylation of hemocyanin in Litopenaeus vannamei is an antibacterial response feature. *Immunol. Lett.* **192**, 42–47 (2017).

91. Sommer, L. Harvesting Blood From Limpets for a Cancer Vaccine. *IEEE Spectrum* (2012).

92. Dolashka, P. *et al.* Antiviral activity of Hemocyanin Rapana venosa and its isoforms against Epstein-Barr virus. *Glob. J. Pharmacol.* **8**, 206–212 (2014).

93. Longa, S. Della *et al.* The Dinuclear Copper Site Structure of Agaricus bisporus Tyrosinase in Solution Probed by X-ray Absorption Spectroscopy *. *Biochemistry* **271**, 21025–21030 (1996).

94. Spritz, R. A., Ho, L., Furumura, M. & Hearing, V. J. Mutational analysis of copper binding by human tyrosinase. *J. Invest. Dermatol.* **109**, 207–212 (1997).

95. Bolton, J. C. SPECTROSCOPIC ANALYSIS OF HEMOLYMPH AND HEMOCYANIN FOR THE. (2008).

96. Liu, S. *et al.* Litopenaeus vannamei hemocyanin exhibits antitumor activity in S180 mouse model in vivo. *PLoS One* **12**, 1–14 (2017).

97. He, Y., Zhu, Q., Chen, M., Huang, Q. & Wang, W. The changing 50 % inhibitory concentration (IC 50) of cisplatin : a pilot study on the artifacts of the MTT assay and the precise measurement of density-dependent chemoresistance in ovarian cancer. **7**, (2016).

98. Hodgkin, M. & Bayer, R. Antiviral Activity of Hemocyanin from Homarus americanus. *J. Shellfish Res.* (2015).

99. Schenk, S., Schmidt, J., Hoeger, U. & Decker, H. Lipoprotein-induced phenoloxidase-activity in tarantula hemocyanin. *Biochim. Biophys. Acta - Proteins Proteomics* **1854**, 939–949 (2015).

100. Engel, D. W., Brouwer, M. & McKenna, S. Hemocyanin concentrations in marine crustaceans as a function of environmental conditions. *Mar. Ecol. Prog. Ser.* **93**, 235–244 (1993).

101. Giomi, F. *et al.* Structural and functional heterogeneity of hemocyanin: Intra- and inter-specific comparison in four species of portunid crabs (Crustacea: Portunidae). *Mar. Biol.* **151**, 1237–1247 (2007).

102. Wahab, I. F. & Razak, S. I. A. Polysaccharides as Composite Biomaterials.

103. Áková, L. B. A. Č., Filová, E., Ek, F. R. Č., Ík, V. Š. Č. & Starý, V. Cell Adhesion on Artificial Materials for Tissue Engineering. **53**, (2004).

104. Manian, A. P., Široká, B. & Bechtold, T. Polysaccharide Applications in Textiles and Materials Technologies. **91**, 98–102 (2013).

105. Liang, L., Huang, C. & Ragauskas, A. J. Nanocellulose-based Materials for Biomedical Applications. 36–39 (2017).

106. Diekjürgen, D. & Grainger, D. W. Biomaterials Polysaccharide matrices used in 3D in vitro cell culture systems. *Biomaterials* **141**, 96–115 (2017).

107. Karadzic, I. *et al.* Effects of novel hydroxyapatite-based 3D biomaterials on proliferation and osteoblastic differentiation of mesenchymal stem cells. 350–357 (2014). doi:10.1002/jbm.a.35180

108. Applications, E. Polysaccharide Based Scaffolds for Soft Tissue. (2019). doi:10.3390/polym11010001

109. Áková, L. B. A. Č., Novotná, K. & Ízek, M. P. A. Ř. Polysaccharides as Cell Carriers for Tissue Engineering : the Use of Cellulose in Vascular Wall Reconstruction. **63**, (2014).

110. Mieszawska, A. J. & Kaplan, D. L. Smart biomaterials - regulating cell behavior through signaling molecules. 2–4 (2010).

111. Tanimowo, H. & Sadroddiny, E. ScienceDirect Fundamentals of protein and cell interactions in biomaterials. *Biomed. Pharmacother.* **88**, 956–970 (2017).

112. Iturri, J. & Toca-Herrera, J. L. Characterization of cell scaffolds by atomic force microscopy. *Polymers (Basel).* **9**, (2017).

113. Physiol, A. J. *et al.* Live cell imaging using confocal microscopy induces intracellular calcium transients and cell death. 1083–1089 (2019).

114. Kohn, J. & Moghe, P. V. Profiling Stem Cell States in Three-Dimensional Biomaterial Niches using High Content Image Informatics. 98–109 (2017). doi:10.1016/j.actbio.2016.08.052.Profiling

115. Loh, Q. L. & Choong, C. Three-Dimensional Scaffolds for Tissue Engineering Applications : Role of Porosity and Pore Size. (2013). doi:10.1089/ten.TEB.2012.0437

116. Tayebi, L., Nozari, A., Vashaee, D. & Mozafari, M. Current opinion in tissue engineering microscopy techniques. *Curr. Microsc. Contrib. to Adv. Sci. Technol.* 591–601 (2012).

117. Simão, C. D., Reparaz, J. S., Wagner, M. R. & Graczykowski, B. Optical and mechanical properties of nanofibrillated cellulose : towards a robust platform for next- generation green technologies. 1–24 (2015). doi:10.1016/j.carbpol.2015.03.032

118. Lin, N. & Dufresne, A. Nanocellulose in biomedicine : Current status and future prospect. *Eur. Polym. J.* **59**, 302–325 (2014).

119. Variola, F. Atomic force microscopy in biomaterials surface science. *Phys. Chem. Chem. Phys.* **17**, 2950–2959 (2015).

120. Stylianou, A. Atomic Force Microscopy for Collagen-Based Nanobiomaterials. *J. Nanomater.* **2017**, 1–14 (2017).

121. Marrese, M., Guarino, V. & Ambrosio, L. Atomic Force Microscopy: A Powerful Tool to Address Scaffold Design in Tissue Engineering. *J. Funct. Biomater.* **8**, 7 (2017).

122. Mach, W. J., Thimmesch, A. R., Orr, J. A., Slusser, J. G. & Pierce, J. D. Flow cytometry and laser scanning cytometry, a comparison of techniques. *J. Clin. Monit. Comput.* **24**, 251–259 (2010).

123. Ong, C. S., Fukunishi, T., Zhang, H., Huang, C. Y. & Nashed, A. Biomaterial-Free Three-Dimensional Bioprinting of Cardiac Tissue using Human Induced Pluripotent Stem Cell Derived Cardiomyocytes. 2–12 (2017). doi:10.1038/s41598-017-05018-4

124. Chow, L. W. & Fischer, J. F. Creating biomaterials with spatially organized functionality. *Exp. Biol. Med.* **241**, 1025–1032 (2016).

125. Leijten, J. *et al.* Spatially and Temporally Controlled Hydrogels for Tissue Engineering. 1–35 (2018). doi:10.1016/j.mser.2017.07.001.Spatially

126. Florczyk, S. J. & Lewis, A. M. 3D Porous Chitosan-Alginate Scaffolds: New Matrix for Studying Prostate Cancer Cell-Lymphocyte Interactions In Vitro. **1**, 590–599 (2013).

127. Tilbury, K. & Campagnola, P. J. Applications of second-harmonic generation imaging microscopy in ovarian and breast cancer. *Perspect. Medicin. Chem.* **7**, 21–32 (2015).

128. Cox, G. C. & Feijo, J. Second harmonic imaging of plant polysaccharides. *Multiphot. Microsc. Biomed. Sci. IV* **5323**, 335 (2004).

129. Nadiarnykh, O., Lacomb, R., Campagnola, P. J. & Mohler, W. A. Coherent and incoherent SHG in fibrillar cellulose matrices. **15**, 11014–11019 (2007).

130. Peciulyte, A., Kiskis, J., Larsson, P. T., Olsson, L. & Enejder, A. Visualization of structural changes in cellulosic substrates during enzymatic hydrolysis using multimodal nonlinear microscopy. *Cellulose* **23**, 1521–1536 (2016).

131. Brown, R. M., Millard, A. C. & Campagnola, P. J. Macromolecular structure of cellulose studied by second-harmonic generation imaging microscopy. **28**, 2207–2209 (2003).

132. Zimmerley, M. *et al.* Molecular Orientation in Dry and Hydrated Cellulose Fibers : A Coherent Anti-Stokes Raman Scattering Microscopy Study. (2010).

133. Jonsson, M., Brackmann, C., Puchades, M. & Bratta, K. Neuronal Networks on Nanocellulose Scaffolds. **21**, 1162–1170 (2015).

134. E., M. D. Einstein Relations Connecting Broadband Emission and Absorption Spectra. *Phys. Rev. J. Arch.* **136**, (1964).

135. Farrell, D. J. " The constancy , or otherwise , of the speed of light ". *Horizon* 1–18

136. Dunn, K. W., Kamocka, M. M. & McDonald, J. H. A practical guide to evaluating colocalization in biological microscopy. *Am. J. Physiol. Physiol.* **300**, C723–C742 (2011).

137. Aaron, J. S., Taylor, A. B. & Chew, T.-L. Image co-localization – co-occurrence versus correlation. *J. Cell Sci.* **131**, jcs211847 (2018).

138. Lorén, N. *et al.* Fluorescence recovery after photobleaching in material and life sciences: Putting theory into practice. *Q. Rev. Biophys.* **48**, 323–387 (2015).

139. Shahin, S. *et al.* Multiphoton microscopy as a detection tool for photobleaching of EO materials. *Opt. Express* **22**, 30955 (2014).

140. Live-cell imaging product selection guide. *ThermoFisher Scientific* Available at: https://www.thermofisher.com/us/en/home/life-science/cell-analysis/cellular-imaging/fluorescence-microscopy-and-immunofluorescence-if/microscopy-reagents-and-media/live-cell-imaging-reagents.html.

141. Cahalan, M. D., Parker, I., Wei, S. H. & Miller, M. J. TWO-PHOTON TISSUE IMAGING: SEEING THE IMMUNE SYSTEM IN A FRESH LIGHT. *Proc. McMat 2005 2005 Jt. ASME/ASCE/SES Conf. Mech. Mater. June 1-3, 2005, Bat. Rouge, Louisiana, USA* **2**, 194 (2005).

142. CellTracker Orange CMTMR Dye. Available at: https://www.thermofisher.com/order/catalog/product/C2927.

BIOGRAPHY OF THE AUTHOR

William Patrick Breeding was born in Plano, Texas on August 8th, 1995. He was raised in East Granby, Connecticut and graduated from East Granby High School in 2013. He then attended the University of Maine and graduated with his Bachelors of Science in Bioengineering in 2017. He promptly returned to enter graduate school at the University of Maine in the Summer of 2017. After graduating, he will be working as a project manager at Lobster Unlimited commercializing biomedical, cosmetic and material applications of lobster processing waste byproducts. Patrick is a candidate for the Masters of Science degree in Biomedical Engineering from the University of Maine in August 2019.